

Setup of precise camera based solar tracker systems and greenhouse gas measurements using a modified portable spectrometer

Zur Erlangung des akademischen Grades eines
DOKTORS DER NATURWISSENSCHAFTEN
der Fakultät für Physik des Karlsruher Instituts für Technologie

genehmigte

DISSERTATION

von

Michael Gisi
aus Rheinfelden (Baden)

Tag der mündlichen Prüfung:

7.12.2012

Referent:

Prof. Dr. Johannes Orphal

Korreferent:

Priv. Doz. Dr. Michael Höpfner

Contents

Abstract	1
1 Introduction	3
2 Atmospheric trace gas measurements by solar absorption spectroscopy	5
2.1 Fourier-Transform Spectroscopy	5
2.1.1 The Michelson interferometer	5
2.1.2 Resolution of FTIR spectrometers	8
2.1.3 Practical aspects of solar FTIR spectroscopy	8
2.2 Atmospheric trace gas measurements using FTIR spectrometers	13
2.2.1 IR-absorption spectroscopy	14
2.2.2 Atmospheric retrieval procedure	19
2.2.3 FTIR networks	21
2.3 IMK-related FTIR stations	22
3 Reduction of error sources in solar absorption FTIR measurements	25
3.1 Previous developments to reduce impacts of error sources	25
3.2 The importance of precise solar tracking	27
3.3 The solar position	28
3.3.1 Celestial coordinate systems	28
3.3.2 Variations in Earth's rotation	31
3.3.3 Calculation of the solar position	32
3.3.4 Refractive index of air	35
3.3.5 Refraction	38
3.3.6 Apparent air mass	41
3.4 Finite duration of measurements	42
3.5 Correction of source intensity variations	46
3.6 Sampling-Ghost artifacts	49
3.6.1 Correction of ghost artifacts	51
3.7 Intraday temperature and pressure variability	56
3.8 Conclusions of investigating error sources	60

4	Camera-based optical tracker feedback	61
4.1	Previous quadrant based optical feedback	61
4.2	Camera setup	63
4.3	Principle of operation	65
4.3.1	Image processing	68
4.3.2	Automatic calibration of the optical setup	71
4.4	Advantages of the camera setup	73
4.5	Accuracies of tracking	74
4.5.1	Ellipse center positions	75
4.5.2	Solar line shifts	77
4.5.3	Error budget of the camera-based system	81
4.6	Further indications for the LOS sensitivity of the CamTracker	84
4.6.1	Aperture position	84
4.6.2	Tilting of the spectrometer	85
4.7	Tracking software	86
4.8	Conclusion of the camera-based tracker system	87
5	Solar tracker systems	89
5.1	Tracker set ups	89
5.1.1	Alt-azimuthal “Newport”-setup	89
5.1.2	Astronomical mount	90
5.1.3	Miniaturized setup	91
5.2	Calculation of mirror angles	93
6	CO₂ measurements with a low-resolution spectrometer	97
6.1	Motivation for portable spectrometers	97
6.2	Instrumentation	98
6.2.1	The NIR-modified EM27 spectrometer	99
6.3	Characteristics	102
6.3.1	Instrumental line shape	102
6.3.2	Ghost to parent ratio	103
6.4	Measurements and analysis	103
6.4.1	Setup and operation of the spectrometers: EM27 and reference TCCON spectrometer	103
6.4.2	Data processing and evaluation	105
6.4.3	Spectral windows	106
6.5	Results	108
6.5.1	CO ₂ and O ₂ -columns	108

6.5.2	XCO ₂	111
6.5.3	Comparisons	113
6.5.4	XCO ₂ -Signal to noise	116
6.6	Conclusions of the low-resolution XCO ₂ measurements	117
7	Summary	119
8	Publications and Patents	121
	Acknowledgments	123
	Bibliography	125
	Acronyms	133

Abstract

The investigation of changes in the atmosphere in the context of global warming is a major topic in current research for which measurements of greenhouse gases are essential. The technique of Fourier-Transform Infrared (FTIR) spectroscopy using the Sun as the light source is well suited for this aspect, as it provides total column measurements of atmospheric gases. Despite ongoing improvements, the achieved precision always competes with the quality requirements for assimilation in meteorological models.

Therefore this work presents and discusses solutions for the minimization of error sources in the application of FTIR spectroscopy.

The main focus of this work was to develop a solar tracker with a precision of better than 20 arc seconds. As the tracker's precision directly impacts on the precision of the retrieved trace gas result, the commonly used tracker systems are insufficient for the increased requirements. The new system, which will be called "CamTracker" in the following, uses the novel approach to record the spectrometer's field stop with a camera. These images then are interpreted using real-time image processing algorithms, and the required corrections for the tracker angles are derived. This approach was registered for a patent at the German Patent and Trade Mark Office in 2010 (Gisi et al., 2010). In the framework of this thesis, the CamTracker system was successfully applied to five FTIR spectrometers worldwide. Three of those sites had existing trackers, whereas for two instruments new mechanically tracker setups were designed and built. One is a low-cost tracker with a large beam diameter of 12 cm. The second was built as a lightweight miniature tracker as required for portable spectrometers, and offers a beam diameter of 5 cm.

The precisions achieved with the new system are investigated in detail. In average, it was better than 20 arc seconds which is a significant improvement. In addition to the high precision, the CamTracker system is self-calibrating and needs no additional optical elements, which makes it easy to setup and to maintain. Easy control is offered by a graphical user interface.

In the context of tracking the Sun, a calculation scheme of the astronomical solar position with a precision of about 0.25 arc seconds for an observer on the Earth has been implemented. Various complicating effects are investigated such as the variations in the Earth's rotation speed and the wavelength-, pressure- and temperature-dependent refraction of radiation in the atmosphere.

As the solar elevation angle, and therefore the air mass may change significantly during the recording of a single measurement, the induced influences onto the trace-gas retrieval are investigated as function of measurement durations and elevation angles.

A method for correction of errors induced from clouds passing in front of the Sun is presented, which under non-ideal measurement conditions leads to a reduction of the scatter in the retrieved gas concentrations by more than one order of magnitude.

The currently used spectrometers from Bruker[®] show sampling errors when recording interferograms for measurements in the near-infrared (NIR) spectral range. The influence of this deficit and a possible correction scheme is presented and successively applied to a timeseries of spectra.

Furthermore, the influence of intra-day temperature and pressure changes are investigated towards changes in the retrieval of O₂ and CO₂ total columns. To avoid inaccuracies from this, a program was created to retrieve the relevant temperatures and pressures along the path of radiation from meteorological model data.

In addition to the increased requirements towards the accuracy of greenhouse gas measurements, observations with a reasonable global coverage is highly desirable. Due to financial and infrastructural reasons this is not possible with the currently used high-resolution FTIR spectrometers. Therefore, the capabilities of measuring total column CO₂ values with a portable low-resolution FTIR-instrument are investigated in the second part of this work. This is based on a commercially available EM27 FTIR instrument from Bruker[®], with self-made modifications for measuring the solar spectrum in the NIR. The self-built miniature tracker is attached directly to the spectrometer, resulting in a single setup which is ready-to-use without further assemblies. The tracker is controlled by a CamTracker system. To investigate the capabilities, retrieved CO₂ and O₂ gas columns are compared with a co-located, high-resolution reference instrument, for a time period of 5 months. The agreement between the two instruments in the time series is within 0.1%, which is an outstanding result and was never reached before with a similar compact low-resolution instrument. This capability together with its compactness and robustness makes the instrument an ideal choice, both for campaign uses and for extensions of existing CO₂ measurement networks, especially in remote areas.

1 Introduction

The Earth's atmosphere is indispensable to life on Earth, not only by supplying and transporting the vital oxygen, carbon dioxide and water, but also by shielding harmful solar and extra-terrestrial radiation. In addition, resulting from a sophisticated equilibrium in radiation and heat transfers, the surface temperatures are kept in habitable ranges.

To improve the scientific understanding of the complete atmospheric system, measurements of various kinds of atmospheric parameters are required. For example, this includes the atmosphere's constitution, chemical composition, dynamical processes, and interactions with surface and oceans. This information can then be used to set up and improve computer-based atmospheric models. As the atmosphere can not be investigated in the manner of a normal lab experiment, these models play a major role in atmospheric research, as they provide the possibility to investigate the atmosphere's reactions to external influences. These can originate from human activities such as the release of ozone-destroying substances, greenhouse gases or climate engineering, or natural sources such as the influence of solar intensity variability or volcanic emissions.

The depletion of ozone in the polar regions is a prominent example for the importance of atmospheric measurements. They played a major role in understanding the stratospheric chemistry which causes the destruction of ozone, which was the base for the abolishment of chlorofluorocarbons (CFCs) by the Montreal Protocol in 1987. FTIR measurements are used to monitor trends of CFCs (Kohlhepp et al. (2012)) and ozone.

Another important field of current research is global warming. The Intergovernmental Panel on Climate Change (IPCC), in which thousands of environmental scientists participate, is 90% certain that global warming is primarily caused by increasing greenhouse gas concentrations produced by human activities (IPCC (2007)). For meteorological models which allow estimations in this context, long-term trends of greenhouse gas concentrations such as carbon dioxide (CO_2), methane (CH_4) and nitrous oxide (N_2O) are very important.

The ground-based remote-sensing group at the Institute for Meteorology and Climate Research (IMK) has performed measurements of the atmosphere at several measurement stations world-wide, for many years. The technique is based on high-resolution Fourier Transform Spectrometers which observe the solar radiation arriving at the ground after passing through the Earth's atmosphere. An evaluation of these measurements provides the total column abundances of numerous atmospheric gases including approximate information on the vertical trace gas profile shape. As this type of measurement detects the gases along the observed line of sight through the complete atmosphere, total gas columns are retrieved. These

are well suited for determining long-term trends, as well as for satellite validation, since they are affected only little by local variations on the ground. In contrast, instruments measuring in-situ concentrations are greatly affected by local variations in the planetary boundary layer (e.g. advection of exhaust plumes emitted by power plants), which makes the interpretation of these data difficult for some applications such as satellite validation.

In addition to trend studies, research also has to consider the sources and sinks of greenhouse gases on Earth, to be able to refer them to anthropogenic activities such as the burning of fossil fuels and deforestation or natural activities such as volcanoes. For trend studies and especially for the determination of sources and sinks, the target accuracies are very high ($\leq 0.1\%$). As the current network wide accuracies achieved by solar FTIR measurements are in the range of 0.25% (Wunch et al. (2011)), an identification and reduction of existing error sources is necessary. This will be the main part of this work.

A second severe problem within this context is the lack of global coverage and the insufficient geographic distribution of greenhouse gas measurement stations. To retrieve the required total column values, high resolution FTIR instruments are used to obtain the requested accuracies. These, however, are expensive, large, difficult to maintain and need a lot of infrastructure such as climate control. As a result, in many regions of the world such as Africa or South America, there are practically no high resolution FTIR sites, whereas in central Europe or North America, numerous sites exist. Portable and robust spectrometers could overcome the aforementioned problems, provided that the accuracy is similar to those of the high resolution instruments. This will be investigated in the second part of this work for a portable FTIR spectrometer.

2 Atmospheric trace gas measurements by solar absorption spectroscopy

2.1 Fourier-Transform Spectroscopy

Fourier-Transform Spectroscopy (FTS) has evolved to one of the major techniques for remote-sensing of atmospheric gases. Here it is widely used to analyze radiation in the Mid-Infrared (MIR) and Near-Infrared (NIR) spectral range, as these contain a wealth of spectral signatures which are characteristic for specific molecules, as will be described in section 2.2.1.

The main principles of the measurement technique will be described in the following sections. Further details can be found in the literature, such as Griffiths et al. (2007) and Davis et al. (2010).

2.1.1 The Michelson interferometer

The heart of an FTIR spectrometer is a Michelson Interferometer (see Fig. 2.1), containing a semi-transparent mirror (beamsplitter) which divides the incoming radiation into two partial beams and leads them into the interferometer arms. At their ends, the radiation is reflected back to the beamsplitter by mirrors (often realized by cube corner mirrors which are insensitive to tilting). One or both of the mirrors can move, to vary the optical path difference between the partial beams. The beamsplitter thus also acts as a recombiner, resulting in constructive and destructive interference patterns in the recombined beam. The variable intensity in the recombined beam due to interference is recorded by the detector.

The interferogram, which is the AC part of the recorded interference pattern, depends on the optical path difference x (OPD). The spectrum $S(\tilde{\nu})$, where $\tilde{\nu} = 1/\lambda = \nu/c$ denotes the wavenumber, and the interferogram $I(x)$ are connected via a Fourier Transformation (FT):

$$S(\tilde{\nu}) = \mathcal{F}(I(x)) = \int_{-\infty}^{\infty} e^{-i 2\pi\tilde{\nu}x} I(x) dx \quad [2.1]$$

$$I(x) = \mathcal{F}^{-1}(S(\tilde{\nu})) = \int_{-\infty}^{\infty} e^{i 2\pi\tilde{\nu}x} S(\tilde{\nu}) d\tilde{\nu} \quad [2.2]$$

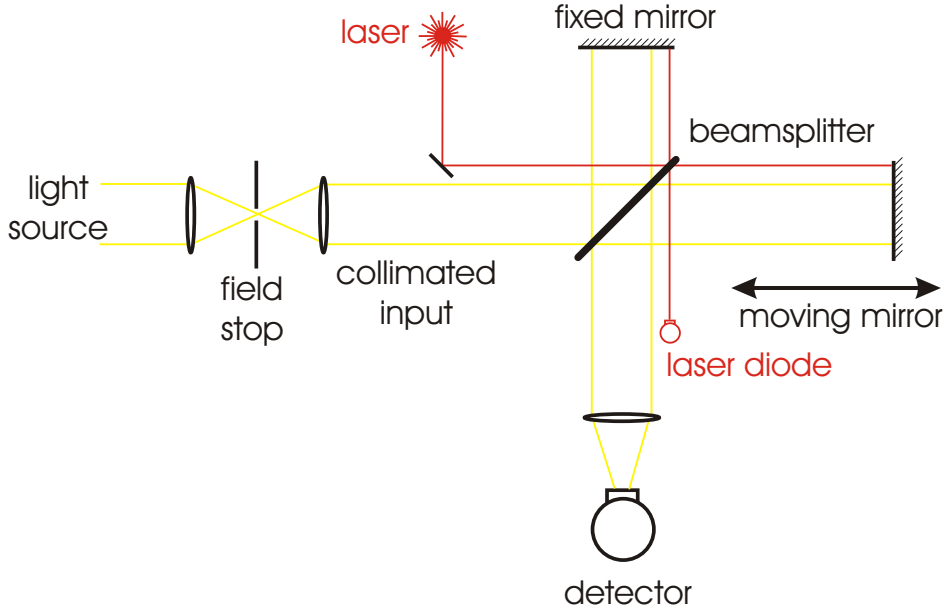


Figure 2.1: Schematic drawing of a Michelson Interferometer. In practice, the focusing and collimating elements are off-axis parabolic mirrors as they do not limit the spectral range to be used and do not suffer from chromatic aberrations. The laser is used for the precise position determination of the moving mirror.

In practice, the recorded interferogram is neither infinite nor continuous. Instead one has N equidistant discrete sampling points with distance Δx and equations 2.1 and 2.2 become:

$$S(\tilde{\nu}_m) = \sum_{n=1}^N I(x_n) e^{-i 2\pi \tilde{\nu}_m x_n} \quad [2.3]$$

$$I(x_n) = \frac{1}{N} \sum_{m=1}^N S(\tilde{\nu}_m) e^{i 2\pi \tilde{\nu}_m x_n} \quad [2.4]$$

The sampling interval Δx has to be adapted to the the frequency range ($\tilde{\nu}_{max} - \tilde{\nu}_{min}$) in the interferogram $I(x)$ due to Nyquist-Shannon sampling theorem:

$$\frac{1}{\Delta x} > 2(\tilde{\nu}_{max} - \tilde{\nu}_{min}) \quad [2.5]$$

In consequence, the optical path difference sampling interval Δx has to be chosen appropriately when recording an interferogram. In practice, Δx and from this, the optical path difference between the two interferometer arms, is derived from interferences of a reference laser which also passes through the interferometer. For all spectrometers and spectra used in this work, the 632.988 nm radiation of a Helium-Neon laser was utilized, and the values of $\tilde{\nu}_{max}$ were 7899 and 15798 cm^{-1} . $\tilde{\nu}_{max}$ and $\tilde{\nu}_{min}$ are the low- and high-folding-limits, which restrict the free spectral range of the FTS. If the Nyquist condition is not satisfied (the detector detects radiation with frequencies outside the range $\tilde{\nu}_{max}$ and $\tilde{\nu}_{min}$), the discrete Fourier Transform cannot properly reconstruct the irradiated spectrum (as illustrated in Fig. 2.2). Instead, these spectral contributions from outside the Nyquist-allowed interval are folded back into the observed range, leading to a distortion of spectrum, as illustrated in Fig. 2.3. This effect is known as aliasing.

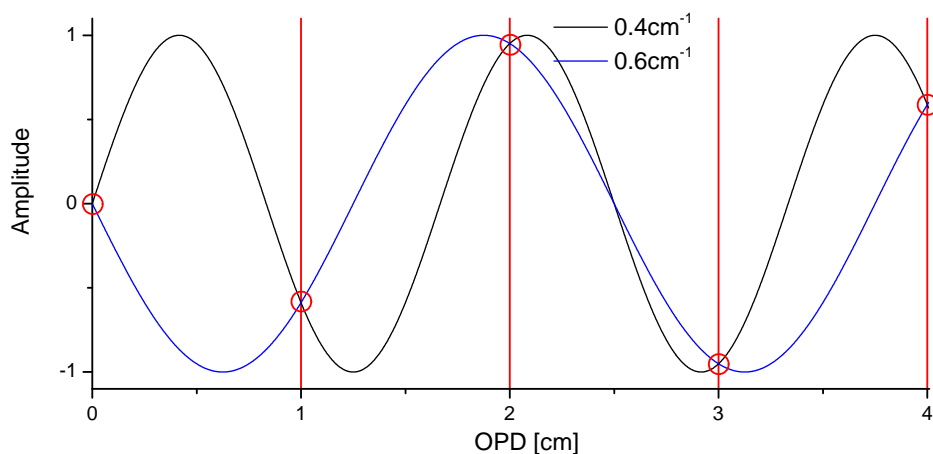


Figure 2.2: Example of 2 sine functions, having the same amplitude at all sampling points (red lines and circles). The wavenumber of the black curve ($\tilde{\nu}_1 = 0.6 \text{ cm}^{-1}$) exceeds the maximal allowed wavenumber ν_{max} of 0.5 cm^{-1} , and therefore is not distinguishable from the red curve with $0.4 \text{ cm}^{-1} = \nu_{max} - (\tilde{\nu}_1 - \nu_{max})$.

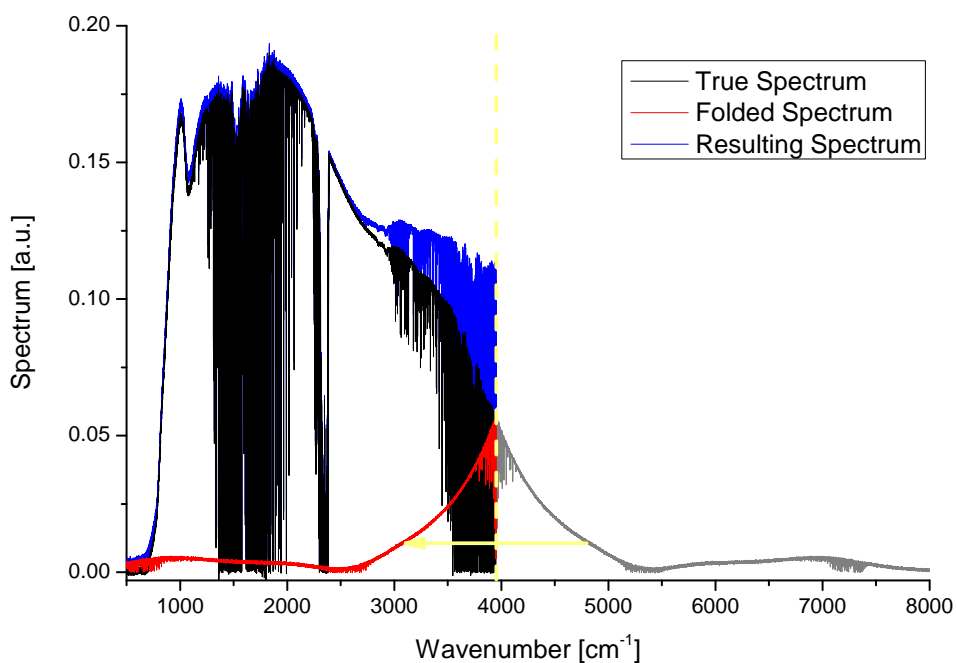


Figure 2.3: Effect of a too low high-folding-limit of 3945.5 cm^{-1} . The measured spectrum (lab measurement with MCT Detector) is the sum of the real (black + gray) and the folded (red) spectrum.

2.1.2 Resolution of FTIR spectrometers

The maximum path difference that can be realized by the movable mirror in the interferometer, and therefore size of the interferogram is finite, limited to the maximal optical path difference (OPD_{max}). Mathematically this can be described as a multiplication of the infinite long interferogram $I_{inf}(x)$ with a box-shaped function: $box(x)=1$ for $|x| \leq OPD_{max}$ and 0 for $|x| > OPD_{max}$: $I_{meas}(x) = I_{inf}(x) * box(x)$. Using the folding theorem, the measured spectrum S_{meas} due to a finite OPD can be calculated from the ideal spectrum S_{inf} :

$$\begin{aligned}
 S_{meas}(\tilde{\nu}) &= \mathcal{F} [I_{meas}(x)] \\
 &= \mathcal{F} [I_{inf}(x) \cdot box(x)] \\
 &= \mathcal{F} [I_{inf}(x)] \otimes \mathcal{F} [box(x)] \\
 &= S_{inf}(\tilde{\nu}) \otimes \frac{\sin(2 \pi OPD_{max} \tilde{\nu})}{\pi \tilde{\nu}}
 \end{aligned} \tag{2.6}$$

From this it can be seen that the finite interferogram results in a convolution of the real spectrum with a sinc function. Its width sets the spectral resolution, where the full width half maximum (FWHM) of a sinc function is $0.6035 / OPD_{max}$.

Another important effect of the sinc function are the negative sidelobes, which may give nonphysical values in the measured spectrum. To avoid these, one can numerically modify the interferogram and change the original box function by multiplication with a special function, such as a triangle or a Gaussian. This method, which is called apodization, reduces the sidelobes, but on the other hand degrades the resolution, as can be seen in fig. 2.4. The mathematical equations describing various apodization functions can be found in Hase (2000). The spectral resolution can not uniquely be given as different criteria are common to define when two peaks in a spectrum can be identified separately. In this work we adopt the following definition for the resolution of an FTIR, which is in wide use:

$$resolution = \frac{0.9}{OPD} \tag{2.7}$$

The spectral distance between adjacent spectral bins is $1/(2 \cdot OPD_{max})$, when no apodization is applied.

2.1.3 Practical aspects of solar FTIR spectroscopy

The measured spectrum given by a spectrometer is not identical to the theoretically expected spectrum. Instead, several effects introduce deviations. A systematic effect is caused by the wavelength dependent sensitivity of the detector and efficiency of the beamsplitter. This effect can be canceled out by dividing the measured solar spectrum by a measured lamp spectrum with known spectral irradiation. This is done in the course of the spectral preprocessing for the retrieval program PROFFIT (see sec.2.2.2). Some detectors show a non-linear response function, leading to low-resolution artifacts in the spectra. These have to be removed before doing the retrieval (Abrams et al. (1994)). As the spectrometer itself has a certain temperature, it is emitting infrared radiation, which can disturb the solar spectrum. To minimize

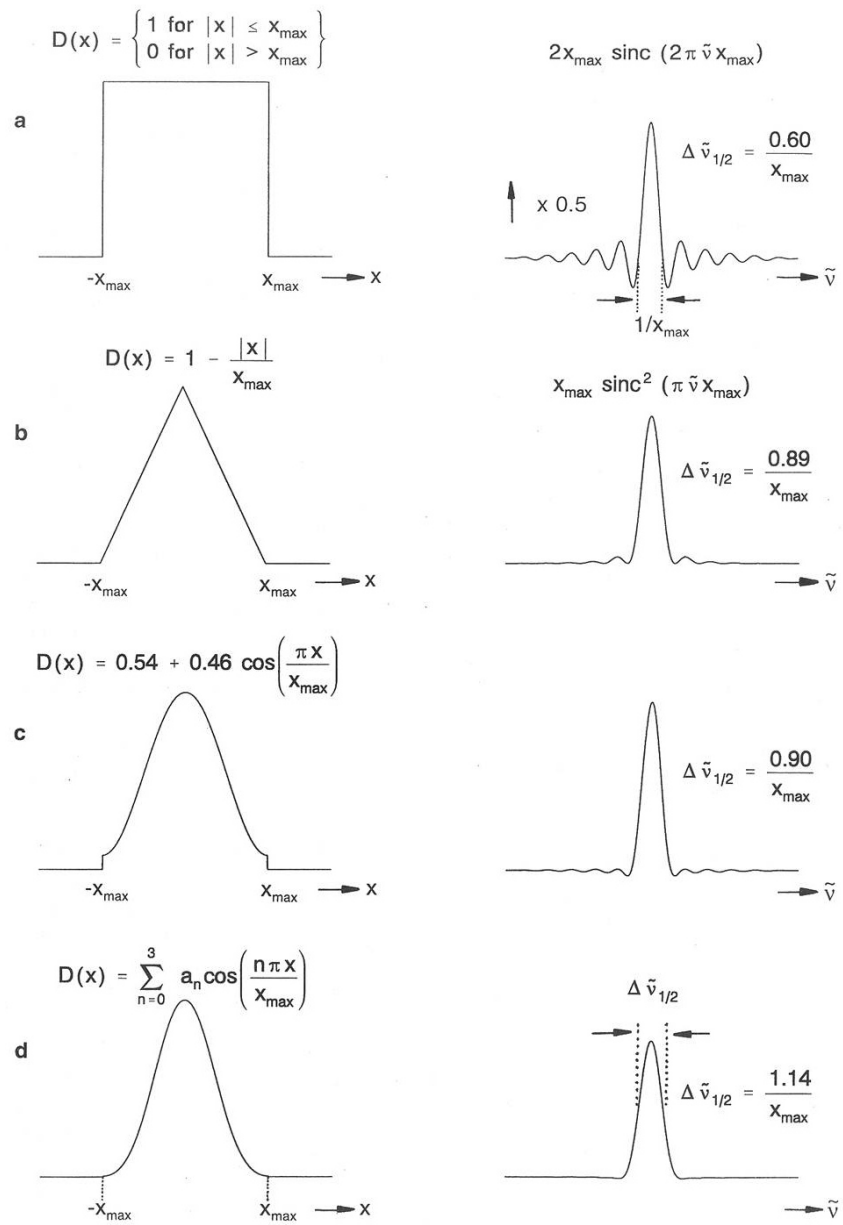


Figure 2.4: Effect of different apodization functions. a) boxcar, b) triangle, c) Happ-Genzel, d) 3-Term Blackman-Harris. (Taken from Günzler and Heise (1996))

this effect, a second field stop often is introduced in a second focal plane in front of the detector. Effects from detector noise lead to statistical variations in the spectrum, which are of secondary importance for solar measurements due to the large intensity of the available radiation. Fluctuations of the solar intensity, for example due to clouds, introduce variations in the amplitude of the interferogram which leads to distortions in the spectrum and errors in the retrieval results. These effects can be reduced, which will be the topic of section 3.5. The necessary precision of the interferogram (IFG) sampling position is very high, as missampling effects cause artifacts in the resulting spectrum. Due to technical reasons, many FTIR spectrometers suffered from erroneous sampling effects for many years. Therefore a correction scheme was developed, which will be presented in sec. 3.6.

Besides the aforementioned effects, OPD dependent wavefront errors cause additional systematic deviations in the measured spectrum. These spectrometer-intrinsic characteristics can be expressed by a specific spectral response function, and should advantageously be used by the analysis software, especially when evaluating high-resolution spectra. For FTIR spectrometers this instrumental line shape (ILS) is advantageously separated into two parts.

The limited OPD and the inherent self-apodization of an FTS with circular field stop lead to a special spectral response function, which also exists for ideally aligned spectrometers. This contribution can be calculated easily from the spectrometers field-of-view and the optical path difference of the interferometer. The self-apodization occurs, since the light in the interferometer is not perfectly parallel. Therefore the interference rings on the detector become smaller with increasing optical path differences (see Fig. 2.5), and the detector averages over several of the Haidinger Fringes, which results in lower interference amplitudes.

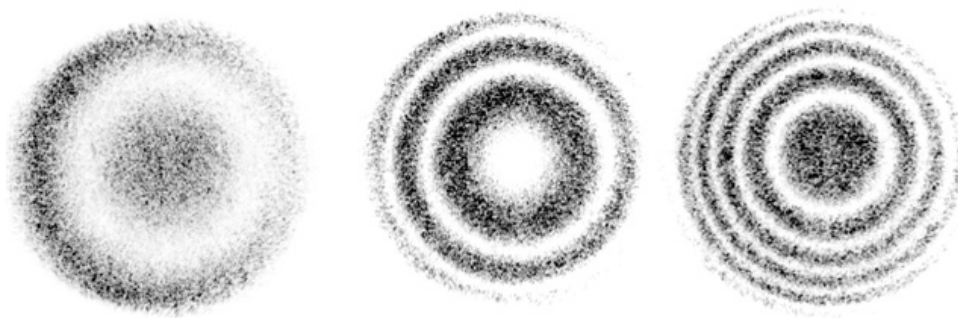


Figure 2.5: Pictures taken by F. Hase (Hase (1995)) of the signal in the detector plane are shown on the right for optical path differences of 10, 40 and 70 cm. These so-called Haidinger fringes form due to the finite field stop diameter.

The deviation from the parallel beam path in the interferometer results from a field stop radius r greater than zero. Therefore, light enters the interferometer with a maximum angle of:

$$\alpha_{max} \approx \frac{r}{F} \quad [2.8]$$

where F denotes the effective focal length of the collimating mirror in front of the field stop. α_{max} is often denoted as the semi-Field of View (semiFOV) of an FTIR spectrometer. This finite acceptance cone alters the ILS of the spectrometer in a way, that in the spectral domain, the spectrum is convoluted with a box function of width

$$\Delta\tilde{\nu} = \frac{\tilde{\nu}_0 \cdot \alpha_{max}^2}{2} \quad [2.9]$$

Obviously this width is proportional to the wavenumber $\tilde{\nu}_0$, and therefore is not constant within the spectrum. Therefore the size of a field stop has to be adapted to the desired resolution, which becomes more critical towards higher wavenumbers. In addition, the box function is shifted by half its width, resulting in a shift of the measured spectrum towards lower wavenumbers.

There is no unique optimum condition for the field stop radius which should be used for a measurement. On the one hand, a greater radius increases the intensity and therefore reduces the noise, on the other hand, this results in a degradation of the spectral resolution because of the self-apodization. The requirement to have a maximum modulation efficiency for the largest useful wavenumber ν at maximum optical path difference leads to the condition:

$$r = F \cdot \frac{1}{\sqrt{\nu \cdot OPD_{max}}} \quad [2.10]$$

As an example, the standard NIR measurements in Karlsruhe have a OPD_{max} of 65 cm. With a focal length of 418 mm and a maximum useful wavenumber of 10000 cm^{-1} , this results in a ideal radius of about 0.5 mm.

The second component of the ILS can be described by a complex modulation efficiency (represented by a modulation amplitude and a phase error, both functions of optical path difference) which result from misalignments, optical aberrations and the electronic components of the spectrometer. These parameters have to be derived by experiment, e.g. by evaluating gas cell measurements (Hase et al. (1999), Hase (2012)) and can lead to symmetric and asymmetric distortions of the ILS.

The effect of a non-ideal ILS is visualized in Figures 2.6 and 2.7 for the spectral- and the interferogram domain.

When retrieving gas concentrations from spectra (see section 2.2.2), the real apparent ILS is one of the input parameters, which has to be supplied. Of course, the spectrometer should be well aligned, so that the second contribution to the ILS is small (modulation efficiency close to 1 and phase error close to 0). Examples of current, well aligned high-resolution ILS fitting results with LINEFIT version 14 are shown in figures 2.8 and 2.9.

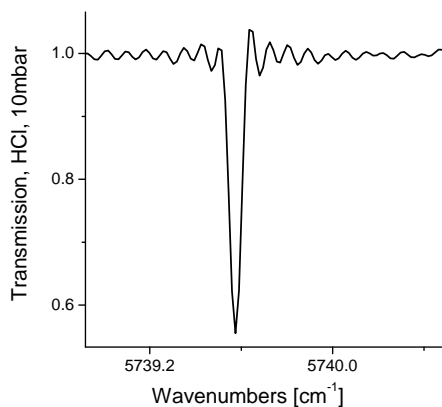


Figure 2.6: Asymmetric spectral line shape due to a misaligned spectrometer.

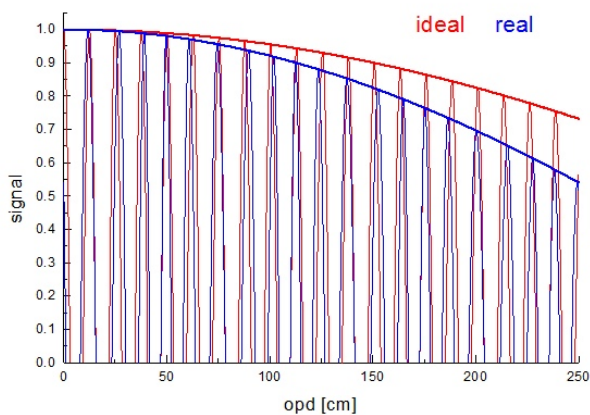


Figure 2.7: ILS effect in the IFG domain. In this illustration the amplitude of a monochromatic light source decreases more rapidly as calculated from pure self-apodization. In addition, the position of the zero crossings are shifted. These two effects can be described by a OPD-dependent modulation efficiency amplitude and a phase error. (Source: F. Hase priv. comm.)

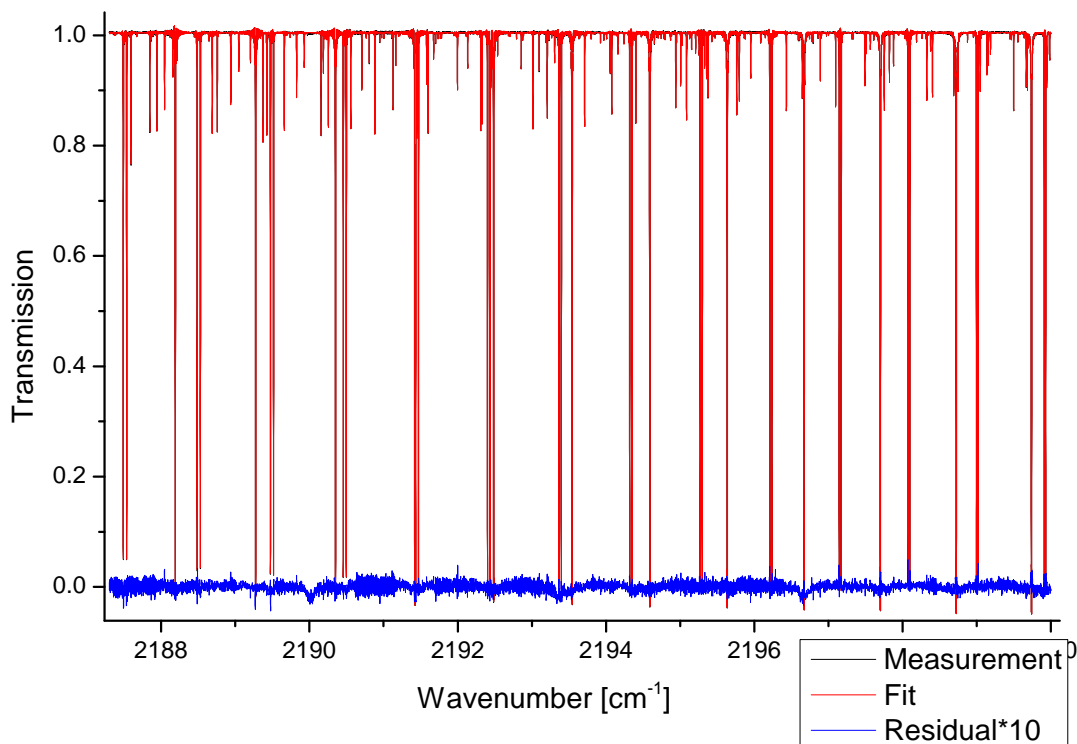


Figure 2.8: Broadband fit of a gas cell (1 mbar N₂O) with LINEFIT for determining the ILS of a IFS125HR spectrometer (Source: F. Hase priv. comm.)

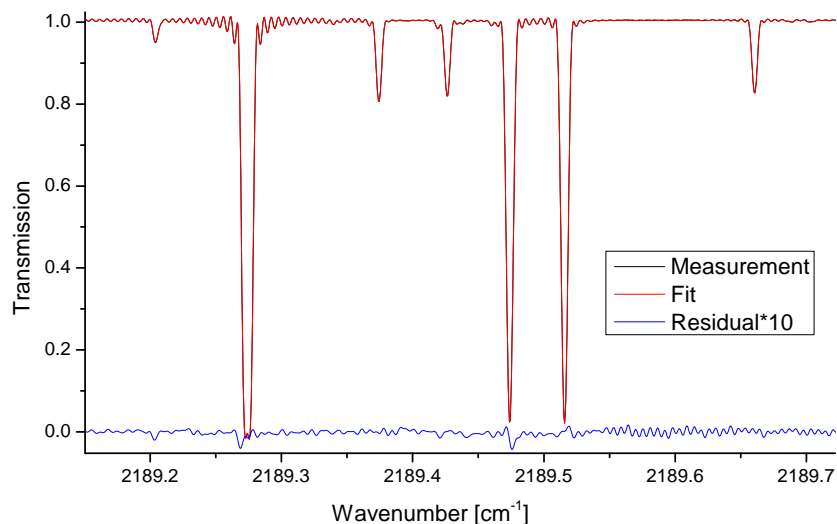


Figure 2.9: Zoom into Fig. 2.9

2.2 Atmospheric trace gas measurements using FTIR spectrometers

The positions and intensities of spectral absorption lines are gas-specific. Therefore these spectral signatures can be used as a fingerprint for identifying the presence, and for quantifying the abundances of gases, e.g. in the Earth's atmosphere.

The light which is analyzed can originate from the atmosphere itself (emission) or from a non-atmospheric background radiation source. For the measurements presented in this work, the Sun was used as the light source causing, due to its high intensity, the emission of the atmosphere to be negligible. For measurements below 1500 cm^{-1} (e.g. ozone at 1000 cm^{-1}), the atmospheric emission is not negligible. In contrast, limb-sounders on satellites, stratospheric balloons and aircraft such as MIPAS or GLORIA, record pure atmospheric limb emission spectra. A third common way is to detect radiation by instruments on satellites, for example the solar radiation scattered back from the Earth's surface (GOSAT or OCO-2) or to record the self emission in the long wave infrared from a satellite instrument such as IASI.

The list of gases which can be measured with the FTIR technique is comprehensive. It encompasses many greenhouse gases such as CO_2 , CH_4 and H_2O , ozone, many gases involved in ozone chemistry such as ClONO_2 , NO_2 , ClO , BrONO_2 , HNO_3 , HCl and many chlorofluorocarbons (CFCs). Therefore, FTIR measurements play a major role in detecting and monitoring changes in the atmospheric constitution and chemistry. The ozone hole and the increase of greenhouse gases are two prominent examples.

2.2.1 IR-absorption spectroscopy

IR spectroscopy is based on the interaction of molecules with radiation in the infrared spectral region. The energy is absorbed or emitted by the molecule, resulting in a change of the vibrational and rotational state. The energy quanta a molecule is able to absorb or to emit depend on its constitution and shape, resulting in highly molecule-specific spectral features.

Spectral lines

The possible changes of rotational and vibrational states of molecules, due to an absorption or emission of radiation, are limited by quantum-mechanical selection rules. These have their origin in the value of the quantum mechanical transition matrix. In this section a short overview is given, more details can be found in Petty (2006), Atkins (2006) or Demtröder (2010). In the dipole approximation, a change from the states i to f can be written as

$$\mu_{fi} = \langle f | \vec{\mu} | i \rangle$$

where $\vec{\mu}$ is the electric dipole operator. A vanishing value indicates a forbidden transition.

The general quantum-mechanical selection rule which has to be fulfilled in an absorption process, is the existence or the change of the molecule's electrical dipole moment. The first condition has to be fulfilled for pure rotational transitions, the latter for rovibronic transition. For example, the symmetric stretching vibration (see Fig. 2.10) of the linear CO₂ molecule does not change the dipole moment. Therefore this can not be excited or changed by an infrared absorption process: it is "IR-inactive". The asymmetric stretching vibration or the bending vibration, however, do change the dipole moment, so these transitions are "IR-active". Another obvious effect from this requirement is the IR-inactivity of homonuclear diatomic molecules such as N₂ or O₂¹.

The vast majority of the observed spectral features in the NIR and MIR results from rovibrational transitions², where the vibration quantum number ν changes at least by 1, and in general, the rotation quantum number J changes as well. The relevant selection rules therefore are:

$$\Delta\nu = 1, 2, 3, \dots$$

and

$$\Delta J = -1, 0, 1$$

In contrast to an ideal quantum-mechanical harmonic oscillator, the allowed changes in $\Delta\nu$ are greater than 1, however they occur with decreasing probability, resulting in much weaker spectral lines.

¹In fact, these restrictions only hold for the electric dipole-transition. The less likely electronic or magnetic multipole transitions allow many more transitions, so that the O₂ and N₂ signatures can be observed with solar absorption spectroscopy. These two molecules can be detected due to their huge abundance in the atmosphere.

²Some spectral features from pure rotational transitions can be observed as well, requiring the molecule to have a permanent dipole moment.

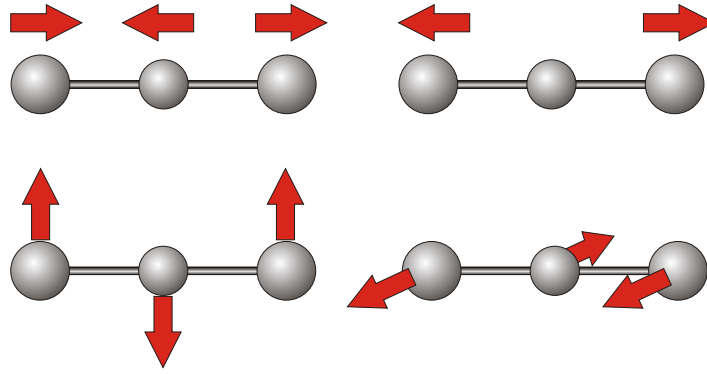


Figure 2.10: The 4 vibration modes for a linear, triatomic molecule, such as CO_2 . In contrast to the asymmetric stretching (top left), the symmetric stretching is IR-inactive. The energies to excite these vibrations, and therefore the corresponding spectral lines, are $\nu_1=2349\text{ cm}^{-1}$ (asymmetric stretching) $\nu_2=1388\text{ cm}^{-1}$ (symmetric stretching) and $\nu_3=667\text{ cm}^{-1}$ (bending).

Whether the rotation quantum number J has to change by ± 1 or not for an allowed absorption process, depends on the type of molecule and the type of vibration. In case of a linear molecule, like CO_2 or CO , the stretching vibrations change the dipole moment parallel to the molecular axis (therefore also called parallel band), which forbids the $J=0$ case due to a selection rule. Bending vibrations, however, cancel the linearity of the molecule and change the dipole moment perpendicular to the molecule's axis (perpendicular bands) which allows the rotation quantum number to stay the same. Diatomic molecules, as they only have parallel bands, do not allow the $J=0$ -case³.

The energies that correspond to a molecular vibrational state can be approximated for low vibrational states by a harmonic oscillator. For higher states this is not a good approximation, as the parabolic potential would not allow the molecules to dissociate. Therefore some anharmonicity is needed in the molecule's potential, which can be expressed by a Morse potential which is shown in Fig. 2.11. The resulting energies of the molecule then become:

$$E_{\text{vib}}(\nu) \approx \left(\nu + \frac{1}{2}\right) \nu_0 - \left(\nu + \frac{1}{2}\right)^2 \cdot \frac{\nu_0^2}{4D_e} \quad [2.11]$$

where ν_0 is a constant depending on the mass and D_e is the depth of the potential. The first part can be identified as the energies of a harmonic oscillator, the second part is introduced by the anharmonicity in the potential. In contrast to the harmonic oscillator, the Morse potential allows $\Delta\nu$ values greater than 1.

The energies corresponding to a molecular rotational state are given by

$$E_{\text{rot}}(J) = hcBJ(J+1) - hcD_J[J(J+1)]^2 - \alpha\left(\nu + \frac{1}{2}\right)J(J+1) \quad [2.12]$$

where the first part is derived from an rigid rotator, the second takes into account the fact, that the molecule expands with increasing rotation due to centrifugal forces, and the third the variable sizes of

³An exception to this rule is the paramagnetic NO molecule. This has an electronic orbital angular momentum parallel to the symmetry axis, which enables a $\Delta J=0$ transition.

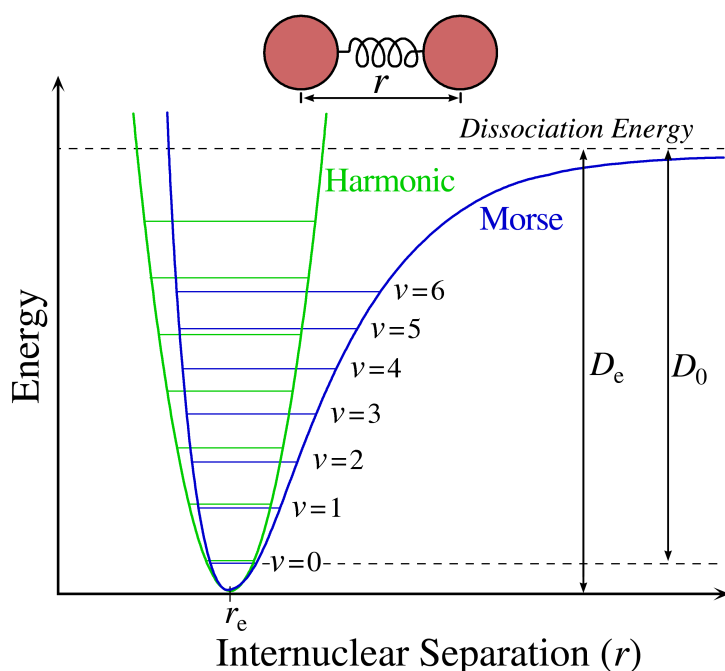


Figure 2.11: Visualization of the potential energies given by a harmonic oscillator and the Morse potential. The differences between the vibrational states become smaller for higher ν in the Morse potential. (Image taken from Wikipedia)

the molecule due to vibrations (vibration-rotation coupling). The principal rotational constant B is given by

$$B = \frac{\hbar}{4\pi cI}$$

with the moment of inertia I . The centrifugal distortion constant D_J is an empirical value, depending on the force needed to stretch the molecule.

The energy of a photon which is needed to be absorbed by a molecule is given by the energy difference between the molecule's final and initial ro-vibronic state, as described above. The major part comes from the change in vibration energy, whereas the energy to change the rotational state is rather small. A level scheme visualizing the possible transitions is given in Fig. 2.12. As all the lines to a specific $\Delta\nu$, which are called a spectral band, are grouped by their value of ΔJ , they are named as a P-, Q- and R-branch of a band, corresponding to a ΔJ of -1, 0 and +1, respectively.

A resulting spectral band of CO_2 is displayed in Fig. 2.13 where one clearly observes the P- and R-branches. The intensities of the lines, and therefore the general shape of the band, is determined by the transition matrix element μ_{fi} and the temperature of the gas, as this determines the population n_i of the molecular states. The ratio can be described using the Boltzmann statistics:

$$\frac{n_J}{n_0} = \frac{g_J}{g_0} e^{-\frac{(E_J - E_0)}{k_b T}} = (2J + 1) e^{-\frac{(E_J - E_0)}{k_b T}}$$

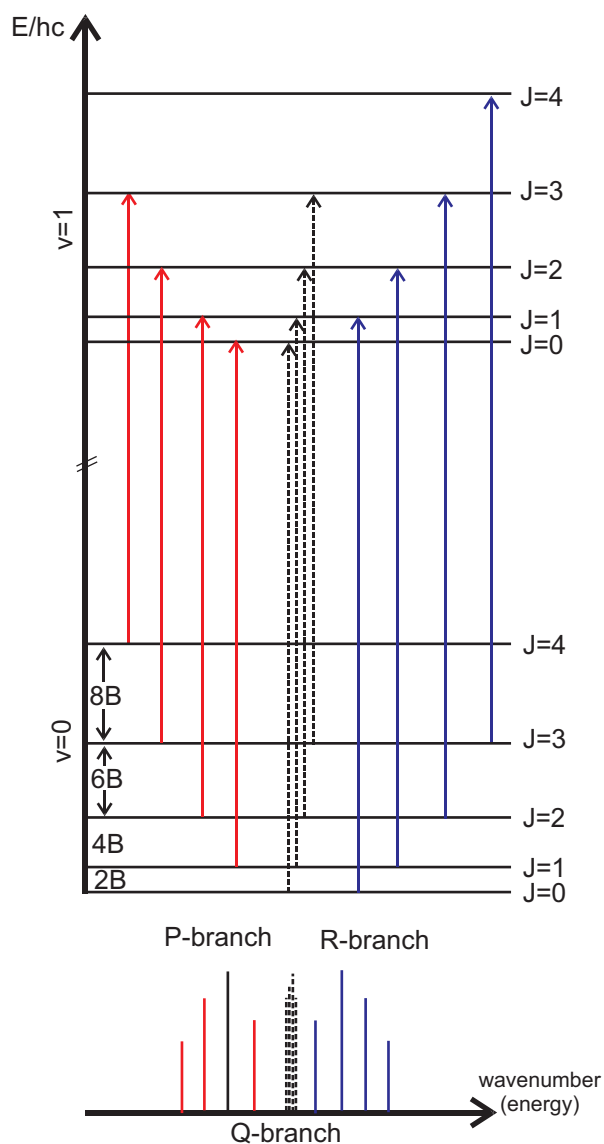


Figure 2.12: Possible transitions of a molecular state. In the case of a rigid rotator, the distance of the rotational levels are a multiple of B , as indicated in the figure. The lines in the P- ($\Delta J = -1$) and R- ($\Delta J = +1$) branch then are equidistant, and all the lines of the Q-branch have exactly the same energy.

The factor g is the degeneracy of a rotational energy level. For low J , close to the center of a band, the factor $(2J+1)$ is dominating, causing the lines to become stronger for higher J , until the thermal distribution of the molecular states becomes the dominating effect, which causes a decrease in line intensities for increasing J .

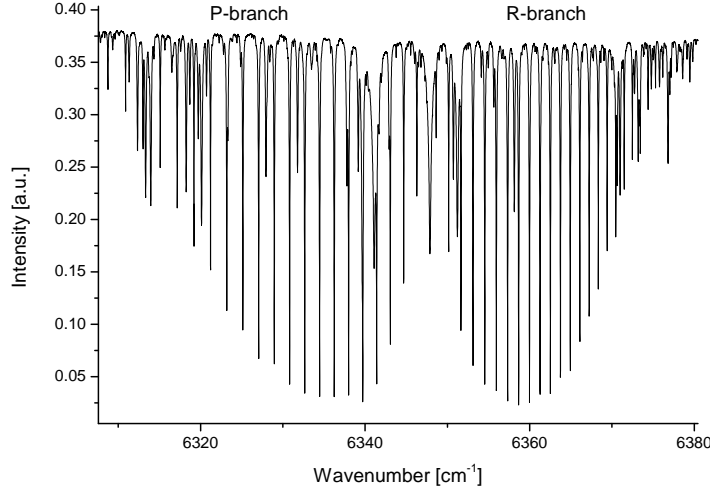


Figure 2.13: Spectral absorption band of CO_2 from a solar absorption measurement with the IFS125HR spectrometer in Karlsruhe and a resolution of 0.014 cm^{-1} . The presented lines belong to a so-called combination band, which are formed by exciting a combination of different vibration modes. In this case it is formed by $\nu_1 + 2 \cdot \nu_2 + 2 \cdot \nu_3$ with the definition in Fig. 2.10 on page 15.

Spectral lineshapes

The spectral lines induced from emission or absorption are not infinitesimally narrow. Instead, several factors contribute to a specific width and shape, where the Doppler- and the pressure broadening mechanisms are the main components. The (always existing) natural line width due to radiative decay can be neglected for atmospheric conditions.

Doppler-broadening: If a molecule moves parallel to incoming radiation, the observed wavenumber $\tilde{\nu}$ depends on the parallel velocity component u_{\parallel} of the molecule due to the Doppler effect:

$$\tilde{\nu}_{\text{doppler}} = \tilde{\nu} * \left(\frac{c + u_{\parallel}}{c - u_{\parallel}} \right) \quad [2.13]$$

In a thermal gas with a molecular mass of m and temperature T , the distribution of the absolute velocity $u=|\vec{u}|$ is given by the Maxwell-Boltzmann distribution:

$$P(u) = 4\pi \left(\frac{m}{2\pi k_B T} \right)^{\frac{3}{2}} u^2 \cdot e^{-\frac{mu^2}{2k_B T}} \quad [2.14]$$

The resulting width of the spectral line depends on the temperature T and has a Gaussian shape:

$$f_G(\tilde{\nu}) = \frac{1}{\sigma\sqrt{2\pi}} \cdot e^{-\frac{1}{2}\left(\frac{\tilde{\nu}}{\sigma}\right)^2} \quad [2.15]$$

with the standard deviation $\sigma = u\sqrt{\frac{k_B T}{m}}$. The full width at half maximum is $\Delta\tilde{\nu} = \frac{\tilde{\nu}}{c}\sqrt{\frac{8k_B T \ln 2}{m}}$. The Doppler-broadening therefore is proportional to the wavenumber.

Pressure-broadening: In the presence of many molecules, there will occur collisions, with a probability dependent on the total pressure and the temperature. These collisions can be elastic, resulting in a broadening of the lines, and inelastic, which also causes a shifting. The broadening can be understood as an interaction-induced shortening of the lifetime, leading to a broadening of the energy due to the uncertainty-relation $\delta E = \hbar/\tau$. The same is true for the natural line width, which results from the uncertainty-relation of its radiative decay, which however is negligible in many cases. The combined line width then is $\gamma = \gamma_{natural} + \gamma_{impact}$ and the resulting spectral line has a Lorentzian shape:

$$f_L(\tilde{\nu}) = \frac{\gamma/(2\pi)}{\tilde{\nu}^2 + (\gamma/2)^2} \quad [2.16]$$

The pressure broadening effect is dependent on the type of interacting molecules. In practice, the pressure broadening width γ is calculated as the sum of tabulated parameters for the self-broadening (collisions with the same molecule) and the foreign-broadening (collisions with other molecules):

$$\gamma = \gamma_{self}^0 p_{self} \left(\frac{T_0}{T}\right)^s + \sum_i \gamma_i^0 p_i \left(\frac{T_0}{T}\right)^s \quad [2.17]$$

where i stands for the other molecule types, the variables with the index 0 denote the values to be applicable for reference conditions T_0 and p_0 . The variable p stands for the partial pressures of the respective gases, and s can be calculated as 0.5 from an ideal gas, using the impact approximation.

Voigt profile: In general, both Doppler and pressure broadening contribute to the shape of a spectral line. The resulting profile therefore is the convolution of a Gaussian with a Lorentzian function which gives a Voigt profile:

$$f(\tilde{\nu}) = \int f_L(\tilde{\nu}) \cdot f_G(\tilde{\nu} - \tilde{\nu}') d\tilde{\nu}' \quad [2.18]$$

This convolution integral, however, can not be solved analytically. Instead, numerical approximations are used, which can be found in literature (Puerta and Martin (1981), Ouyang and Varghese (1989), Humlíček (1979), Olivero and Longbothum (1977), Liu et al. (2001)).

2.2.2 Atmospheric retrieval procedure

To retrieve atmospheric trace gas abundances, the recorded spectra are analyzed by a computer program. This applies a model of the radiative transfer in the Earth's atmosphere to generate an atmospheric spectrum from a set of relevant input parameters (forward model). These contain atmospheric quantities such as temperature, pressure and various volume mixing ratios (VMRs), auxiliary parameters such as the solar zenith angle (SZA) and the ILS parameters and spectral information of the relevant gases, most often provided by linelists such as HITRAN⁴. The forward model has to be adapted to the type of measurement

⁴<http://www.cfa.harvard.edu/hitran/>

(ground-based, spaceborne, absorption, emission, scattering,...) as the different measurement geometries have to be included and different effects (scattering, nonlocal thermodynamic equilibrium,...) are more or less prominent. In this work, only ground-based solar absorption FTIR spectra and their analysis will be discussed.

A second part of the analyzing software calls the forward model repetitively and ‘tries’ to match (to ‘fit’) the measured spectrum by varying a selected set of variables. Unfortunately the retrieval problem can be ill-posed, meaning that some retrieval variables can not be determined unambiguously from a measured spectrum. Therefore, additional informations have to be provided. For example, a-priori information is used, which are parameters describing the atmosphere to the best available knowledge. Other values often are kept fixed, such as the temperature profile obtained from other sources (see sec. 3.7). In addition, several constrains (“regularization” parameters) have to be introduced, limiting the allowed variation of the retrieved values to prevent non-physical results.

A widely used regularization is the Tikhonov-Phillips method (Hase (2000)), which, in its most simple form, performs a scaling of a given gas profile. This approach is justified for gases such as CO₂, having a very small vertical variability in the volume mixing ratio. A more general approach is to adjust the profile as a function of altitude. This of course activates a huge set of input parameters for the fit, for which reason constraints on the resulting shape and values of the profile are required to achieve a useful solution.

Currently three atmospheric retrieval programs are widely used for ground-bases solar absorption FTIR spectroscopy: GFIT, SFIT2 and PROFFIT.

GFIT is used as the official analysis code for the Total Carbon Column Observing Network (TCCON) (see section 2.2.3) and is maintained by G. Toon at the California Institute of Technology. In the TCCON it is used as a part of the software package GGG, which also includes preprocessing of the interferograms and post-processing of the resulting XCO₂. More details can be found in (Wunch et al., 2011).

PROFFIT is widely used in the Network for the Detection of Atmospheric Composition Change (NDACC) and maintained by Frank Hase at the Karlsruhe Institute for Technology (KIT) (Germany). It is well established for work within the NDACC FTIR network and has been validated in various studies (Schneider et al. (2008), Schneider et al. (2010) and Sepúlveda et al. (2012)). For this work, most of the spectra were analyzed with PROFFIT.

SFIT2 is widely used in the NDACC and maintained by J. Hannigan at the National Center for Atmospheric Research (NCAR) in Boulder (USA), N. Jones at the University of Wollongong (Australia) and M. Palm at the University of Bremen (Germany). A comparison with PROFFIT can be found in Hase et al. (2004).

2.2.3 FTIR networks

Ground-based solar absorption Fourier Transform Infrared (FTIR) measurements are performed at numerous sites worldwide to retrieve trace gases in the terrestrial atmosphere. To monitor and investigate the composition and the chemistry of the atmosphere, most FTIR stations take part in networks, ensuring a uniform quality standard both on the measurement and the retrieval side. In addition, public access to the dataset is possible due to a centralized storage of retrieval results.

Prominent FTIR networks are the “Network for the Detection of Atmospheric Composition Change” (NDACC⁵) and the “Total Carbon Column Observing Network” (TCCON⁶). The FTIR section of the

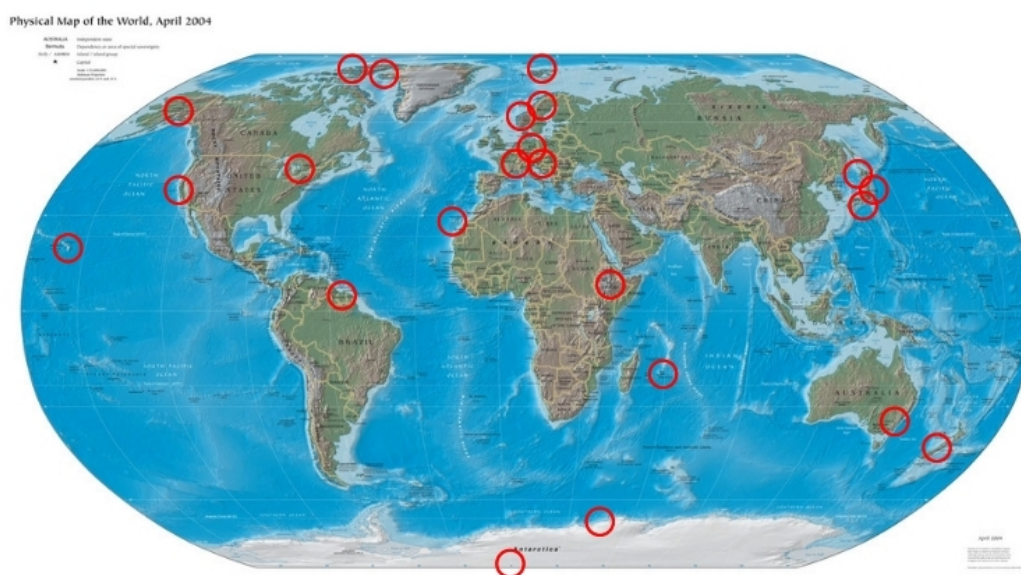


Figure 2.14: Location of the NDACC FTIR stations. Image taken from <http://www.ndacc.org/>

NDACC operates in the mid-infrared (MIR) spectral region and encompasses over 20 measurement sites worldwide (see Fig. 2.14). Its observations aim for an understanding of the physical and chemical state and change of the upper troposphere and the stratosphere. As the measurement time series reach back up to 20 years, it is well suited for investigating long-term changes, such as the ozone column amount. The MIR spectral region allows for detecting a large number of gaseous atmospheric components, such as O_3 , N_2O , NH_3 , CO_2 , HNO_3 , HCl , HF , CO , N_2O , CH_4 , HCN , C_2H_6 , $ClONO_2$ and many more.

The TCCON focuses on column measurements of greenhouse gases, mainly CO_2 but also CO and CH_4 , in the near infrared (NIR) at about 20 sites worldwide (Toon et al., 2009; Wunch et al., 2010, 2011). It

⁵<http://www.ndsc.ncep.noaa.gov>

⁶<http://www.tccon.caltech.edu>



Figure 2.15: Locations of the TCCON station. Image taken from Wunch et al. (2011)

was founded to support and validate the satellite-born NASA instrument OCO/OCO-2 which will presumably be launched in 2014, and is, similar than the Japanese satellite GOSAT⁷, exclusively dedicated to measuring greenhouse gases. To make the network results comparable to WMO (World Meteorological Organization) standards, they are compared with in situ profiles measured in the framework of aircraft campaigns (Wunch et al. (2010), Messerschmidt et al. (2011), Geibel et al. (2012)). For example the X_{CO_2} value (see eqn. 3.3 on page 26) retrieved by TCCON FTIR instruments is divided by an empirical calibration factor of 0.989.

2.3 IMK-related FTIR stations

The ground-based FTIR group at the “Institute of Meteorology and Climate Research” (IMK) in Karlsruhe runs 3 sites (Kiruna, Teneriffe and Karlsruhe) and 2 additional sites in close cooperations with local working groups (Addis Ababa and Altzomoni). A few facts about these stations will be given in the following, further details are given in table 2.1.

Kiruna (Lapland, Sweden): This station is part of the NDACC. The high latitude of this site enables measurements of the polar vortex in the late winter and early spring which are very valuable for investigating the ozone chemistry in the atmosphere. It is equipped with special detectors for lunar measurements. It is placed in a lab below the roof of the “Swedish Institute of Space Physics”⁸.

Izaña (Canary Islands, Spain): This station is part of the TCCON and the NDACC. This subtropical high altitude station lies above an inversion layer, enabling nearly undisturbed measurements of the free troposphere. As it is co-located with a Global Atmosphere Watch (GAW⁹) station, numerous in-situ-instruments such as CH_4 , CO_2 and N_2O are available¹⁰. In addition, it is a Brewer Calibration Center, at which regular ozone measurement comparison and calibration campaigns are performed. The spectrometer is housed in a climatized 20 ft container.

⁷http://www.jaxa.jp/projects/sat/gosat/index_e.html

⁸<http://www.irf.se/>

⁹http://www.wmo.int/pages/prog/arep/gaw/gaw_home_en.html

¹⁰<http://www.izana.org/>

Karlsruhe (Germany): This station is part of the TCCON and the NDACC. The urban surrounding area of this station is helpful for the detection of anthropogenic trace gases in the atmosphere. In addition, the flat orography makes this station an excellent site for satellite validation measurements. A dichroic filter is used, which reflects the NIR part of the radiation to one detector, while the MIR radiation is transmitted onto the other detector. This novel technique allows the instrument to perform NDACC and TCCON measurements simultaneously. It is housed in a climatized 20 ft container.

Addis Ababa (Ethiopia): Due to the sparse abundance of NDACC stations in Africa, this tropical site has high importance regarding a global monitoring of atmospheric trace gases. This site is operated in cooperation with the group of Gizaw Mengistu at the Addis Ababa University. This station will become part of the NDACC.

Altzomoni (62 km southeast of Mexico City): This site will presumably become operational in late 2012 and is built into a climatized 20 ft container. It is operated in cooperation with the group of Michel Grutter at the Universidad Nacional Autónoma de México (UNAM). This station will become part of the NDACC.

Site	Location	Operational since	Instrument	OPD _{max} / Resolution	Detectors
Kiruna	67.84° N, 20.41° E, 420 m. asl.	1996	IFS120/5HR	360 cm ($\cong 0.0025 \text{ cm}^{-1}$)	LN-InSb LN-MCT
Izaña	28.30° N, 16.48° W, 2370 m. asl.	1999	IFS120/5HR	257 cm ($\cong 0.0035 \text{ cm}^{-1}$)	InGaAs LN-InSb LN-MCT
Karlsruhe	49.10° N, 8.4385° E, 110 m. asl.	2010	IFS125HR	257 cm ($\cong 0.0035 \text{ cm}^{-1}$)	InGaAs LN-InSb
Addis Ababa	9.035° N, 38.766° E, 2320 m. asl.	2009	IFS120/5M	257 cm ($\cong 0.0035 \text{ cm}^{-1}$)	LN-InSb LN-MCT
Altzomoni	19.119° N, 98.655° W, 4000 m. asl.	2012	IFS120/5HR	257 cm ($\cong 0.0035 \text{ cm}^{-1}$)	LN-MCT InGaAs LN-InSb

Table 2.1: Details about the FTIR measurement sites part of, or cooperating with the IMK. The spectrometers denoted as IFS120/5 are older 120 spectrometer types with update, so these are similar to the IFS125 spectrometers.

3 Reduction of error sources in solar absorption FTIR measurements

Due to the complex measurement subject (the atmosphere), the variable measurement geometry (moving light source) and also the highly sophisticated (but sensitive) measurement procedure, there are numerous error sources that can lead to erroneous atmospheric trace gas retrieval results, already on the experimental side. The efforts to continuously increase the accuracy of the retrieved column-averaged abundances of atmospheric constituents lead to increasing requirements towards the minimization of error sources. In this chapter several of these sources are characterized, and solutions for their minimization are presented as necessary. A method to increase the line-of-sight (LOS) of the solar tracker is presented in chapter 4, as this is a main part of this work.

When performing spectroscopic measurements using the Sun as source of radiation, the apparent solar position on the sky has to be calculated. This position is needed both to obtain coordinates for the solar tracker and to calculate the LOS when evaluating the spectra. A method to precisely determine the apparent solar position was developed, and is presented in sec. 3.3.

To record a single spectrum usually takes several minutes. Within this time the solar position may change significantly. Resulting effects onto the trace gas retrieval will be investigated in section 3.4.

Clouds passing in front of the Sun while recording an interferogram lead to distorted spectra. A procedure which is capable to reduce the effect of these solar intensity variations is presented in 3.5.

As temperature and pressure in the course of one measurement day may change significantly, the usage of intraday pressure and temperature profiles is necessary in the trace gas retrieval, which is presented in section 3.7.

Non-equidistant sampling positions when recording an IFG introduce artifacts lead to erroneous retrieval results. The relevant mechanisms are presented in 3.6, together with a possible a-posteriori correction scheme.

3.1 Previous developments to reduce impacts of error sources

For monitoring the atmospheric variability of greenhouse gases, the usage of column-averaged dry air mole fractions (DMF) is beneficial, as the column amount is affected by the variability of the ground pressure. The definition of a column-averaged DMF of a gas G (X_G) is the following:

$$X_G = \frac{G_{column}}{DryAir_{column}} \quad [3.1]$$

The dry air column can be estimated by the ground pressure and the humidity of the atmosphere. A superior method to derive the dry air column is the by ratioing over the the O₂ column amount in the atmosphere, as this quantity can be derived with high precision from FTIR measurements made in the NIR spectral range:

$$DryAir_{column} = \frac{O_{2,column}}{0.2095} \quad [3.2]$$

The factor 0.2095 is the DMF of O₂ in the atmosphere, which is constant up to an altitude of about 100 km. For XCO₂ the formula is:

$$XCO_2 = \frac{CO_{2,column}}{O_{2,column}} \cdot 0.2095 \quad [3.3]$$

As the column of the gas G under investigation and the O₂ column are derived from the same spectrum, several errors sources have similar impacts on the retrieval. The ratioing therefore leads to a reduction of these detrimental impacts, e.g. from pointing offsets, erroneous surface pressure values or wrong times saved for each measurement.

The TCCON makes use of this ratioing as it derives the most relevant gases (CO₂, CH₄,...) from the NIR spectral range. The beneficial effect with respect to several error sources are presented in Wunch et al. (2011). For NDACC measurements which are made in the MIR no equivalent reference gas column can be retrieved with useful accuracy.

However, rationing the CO₂ by the O₂ does not compensate perfectly for all error sources (e.g. an erroneous ground pressure value which will be shown in sec. 3.7), major efforts were undertaken to improve the spectrometer and the interferogram preprocessing, such as

- The characterization of the instrumental line shape (ILS) by using gas cells with known gas constituents and pressures (Hase et al. (1999) and Hase (2012)). The results can both be used to check the apparent alignment of the spectrometer and as an input parameter in the retrieval itself (see sec. 2.2.2).
- The recording of absolute detector values instead of the AC component and the application of a DC correction on the interferogram (Keppel-Aleks et al., 2007). Details are presented in section 3.5, as a similar procedure was implemented in PROFFIT within this work.
- The detection and improvement of the sampling accuracy when recording the interferograms (Messerschmidt et al., 2010) to avoid ghost artifacts. A method for reducing sampling errors is presented in section 3.6.
- The characterization and correction of detector non-linearities (Abrams et al., 1994)

3.2 The importance of precise solar tracking¹

When using the Sun as a source of light for atmospheric absorption spectroscopy, one usually aims to point the interferometer's field-of-view to the center of the solar disk equivalent to centering the solar disk on the circular entrance field stop of the interferometer. Any deviations from the assumed LOS introduce errors in the retrieval of the gas concentrations of the atmosphere. The main problem caused by a pointing error is that the actual observed air mass differs from the air mass assumed in the analysis. The error resulting from a line-of-sight (LOS) error depends strongly on the zenith angle of the Sun and is shown in Fig. 3.1. With a desired tracking range from 0° to 80° solar zenith angle (SZA), one gets up to 9.6% air mass change per degree SZA change. TCCON currently strives for a total CO₂ column precision of 0.1% in order to constrain the interhemispheric gradient (Olsen and Randerson, 2004). To achieve this overall precision, an error in the total gas column due to the tracking of less than 0.05% is desirable. If one wants to maintain this for a tropospheric gas up to a solar zenith angle of 80°, a tracking accuracy of about 19 arc s is required.

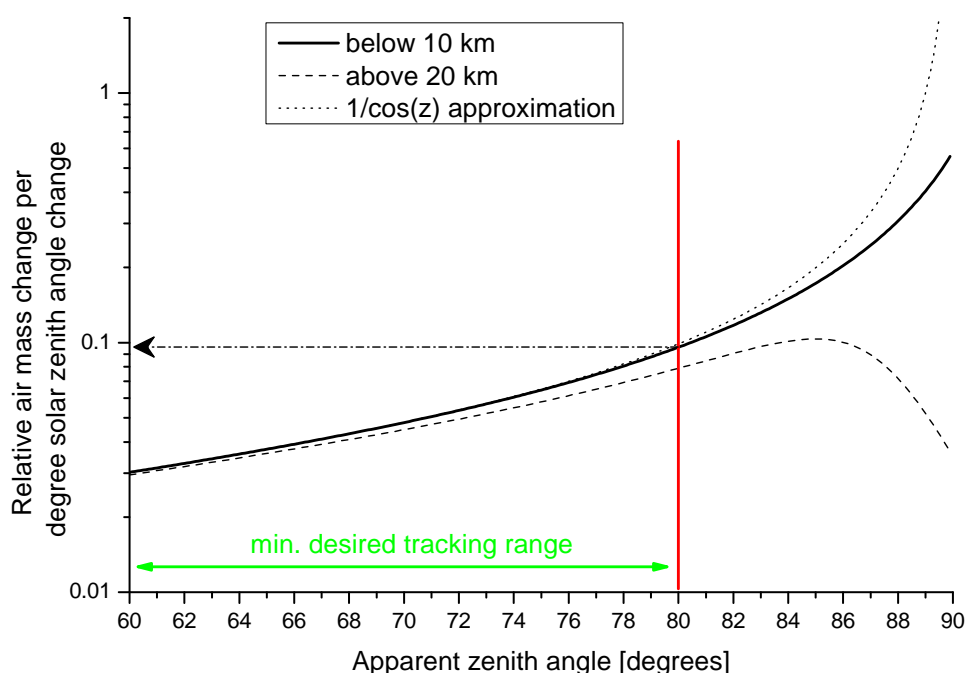


Figure 3.1: Sensitivity of the effective air mass as function of solar zenith angle for the observation of a tropospheric gas with constant VMR up to 10 km (bold line), for the observation of a stratospheric gas with constant VMR above 20 km (dashed) and for the often used analytical approximation $1/\cos(z)$ (dotted). (Graph adopted from Hase, 2000.)

As mentioned above, in the NIR spectral range it is possible to reduce the tracking impact by ratioing the CO₂ slant column to the O₂ slant column as they can be retrieved from the same spectrum. Nevertheless

¹Some sentences from the publication “Camtracker: a new camera controlled high precision solar tracker system for FTIR spectrometers” by Gisi et al. (2011) were adapted for this section.

an excellent tracking knowledge is highly desirable, because this allows to recognize other problems by monitoring the observed O₂ column.

Therefore, within this work, a new and highly precise tracking system was developed, which is explained in detail in chapter 4.

3.3 The solar position

In the retrieval of trace gases, the spectrometer's LOS has to be known for calculating the spectral absorption of the solar radiation when passing through the atmosphere. For this, the time and the duration of each measurement is saved, from which the required effective solar elevation (respectively the solar zenith angle (SZA)) can be calculated². The unrefracted astronomical position of the Sun for a given time and observer location can be accessed on-line from the Jet Propulsion Laboratory (JPL)³. However, the access to these data requires a permanent Internet connection. As this is not always possible, e.g. at remote sites, or during measurement campaigns. For this reason, a self-standing program for the calculation of apparent solar positions is preferable. However, the necessary astronomical calculations are not trivial. In addition, the radiation is not passing the atmosphere along a straight line. Instead, the temperature- and pressure- dependent refractive index of the atmosphere causes a "bending" of the straight line. This effect is referred to as refraction.

To reduce the errors induced from the SZA calculation, both the astronomical calculation of the solar position and the refractive index calculations were significantly improved for the PROFFIT retrieval setup within this work, which will be described in the following.

3.3.1 Celestial coordinate systems

To describe the position of stars and planets, several celestial coordinate systems are used. A short overview about those relevant for this work will be given in the following:

Horizontal coordinate system The observer's local horizon is used as the fundamental plane, which divides the sky into two hemispheres. The points located perpendicularly above and below the observer are called zenith and nadir, respectively. The angle of an object above the horizon is called altitude or elevation. Often the zenith angle is used (e.g. solar zenith angle (SZA)), which is defined as 90°-elevation. The other angle in this spherical coordinate system is called azimuth. It is defined as the angle across the horizon to the point below the object, measured in a clockwise direction (South → West → North → East), starting either from the South or the North. It always has to be taken care which one of these definitions is used. In this work, South will be referenced as an azimuth of zero.

²The standard analysis codes assumes a pencil beam LOS

³<http://ssd.jpl.nasa.gov/horizons.cgi>

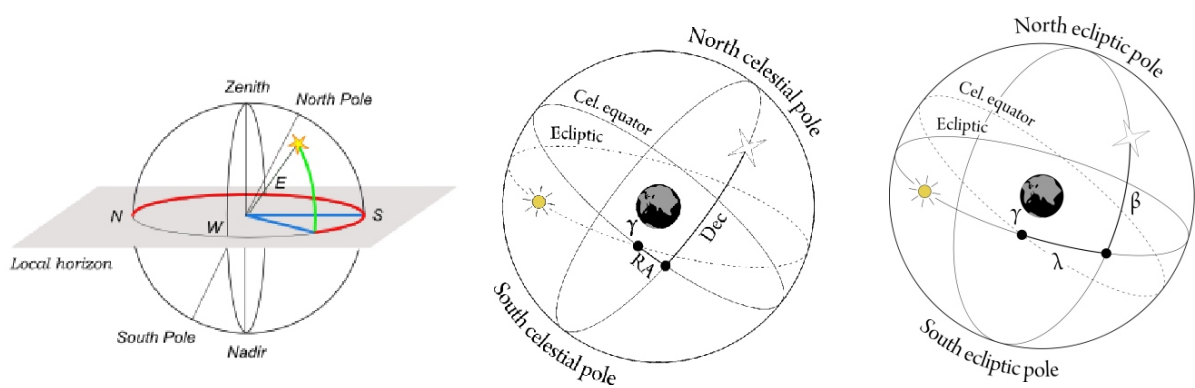


Figure 3.2: Coordinate systems. Left: horizontal, middle: equatorial, right: ecliptical. (Source: en.wikipedia.org)

Equatorial coordinate system This spherical coordinate system is formed by projecting the Earth's poles and equator to the celestial sphere, forming the celestial poles and the celestial equator. The plane of this equator is used as the fundamental plane of this coordinate system. The great circle on which the Sun is apparently moving over the sky in the course of the year is called the ecliptic. The intersection points of these two circles are called equinoctial points (or equinoxes): the sun passes the vernal equinox on 20th or 21th of March and the autumnal equinox on 22th or 23th of September. The vernal equinox is taken as the starting point for the two angles (right ascension and declination) in the equatorial coordinate system. The right ascension (RA) is the angle along, the declination (Dec) is the angle perpendicular to the celestial equator, to get from the vernal equinox to an object on the sky. The measurement direction for RA is towards East, ranging from 0° to 360° . The declination ranges from -90° to 90° , where the celestial North Pole is 90° . The angle between the equatorial plane and the plane of the ecliptic is called axial tilt or obliquity of the ecliptic and is of the order of about $23^\circ 26'$. Due to nutation effects of the Earth's rotation axis, this value is not constant. At present, the axial tilt decreases at a rate of about 47 arc seconds per century.

The precession of the Earth's rotation axis causes the vernal equinox to move by about 50 arc seconds per year in negative direction along the ecliptic. Therefore the position of the stars measured from the vernal equinox vary steadily, so that star catalogs give the right ascension and declinations relative to a reference equinoctial point apparent at a certain point in time. This time is commonly referred to as epoch, designated by J2000.0 (1st of January 2000) or J1900.0.

Ecliptic coordinate system In this celestial coordinate system the plane of the ecliptic is used as the fundamental plane. As in the equatorial system, the vernal equinox is used as the starting point, from where one angle along, and the other one perpendicular to the ecliptic is measured to locate a desired object on the sky. The two angles are called ecliptic longitude and latitude respectively.

Observer's position The position of an observer on the Earth is defined by its geographic longitude, latitude and height. The latitude of a position on the Earth's surface is the angle between the Earth's equatorial plane and a line through the respective point which is perpendicular to the surface. The angles range from -90° for the South Pole to $+90^\circ$ for the North Pole of the Earth. To define longitudes, the Earth's surface is sectioned by meridians, which are great circles going from pole to pole. For historical reasons, the Prime Meridian (longitude of 0°), is defined to lie on the Greenwich Observatory in London, UK. All other meridians are defined by their angles from the Prime Meridian in eastward (positive) or westward (negative) direction.

Another aspect with respect to an observer's position is the shape of the Earth. Instead of a sphere, it can be better approximated as an ellipsoid. The most common "reference ellipsoid" is the WGS 84⁴, defining an equatorial semi-axis of 6378137 m and a polar semi-axis of 6356752.3142 m, which is a difference of 0.33%. The non-spherical shape of the Earth has to be taken into account

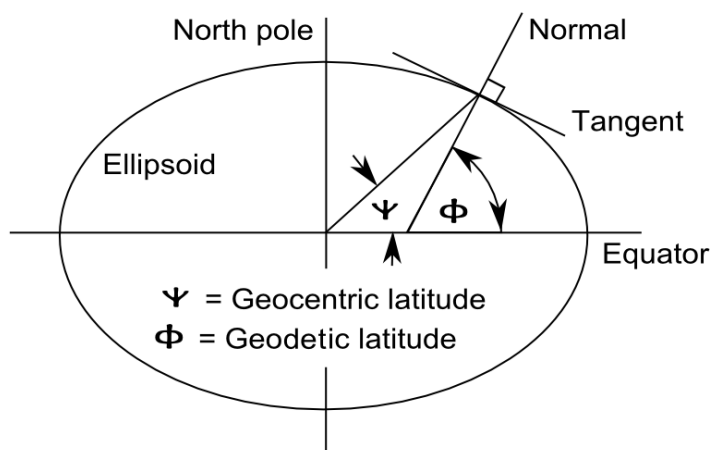


Figure 3.3: Definition of geodetic and geocentric latitude on an ellipsoid, where the first often is referred to as geographic latitude (Source: en.wikipedia.org)

when defining the latitude. Two possible and common definitions are the geocentric and the geodetic latitude (see Fig. 3.3), where the latter often is meant when the notation geographic latitude is used. The height is measured in the direction perpendicular to the ellipsoid surface. These features complicate the transformations between the described coordinate system and geocentric coordinates system significantly (see Gerdan and Deakin (1999)). The latter one was used to model a light path through the atmosphere as will be described in section 3.7.

⁴The official WGS 84 definition can be downloaded at <http://earth-info.nga.mil/GandG/publications/tr8350.2/wgs84fin.pdf>

3.3.2 Variations in Earth's rotation

The Earth's rotation speed is variable. Several effects such as tidal friction and motion of mass within the Earth lead to unpredictable changes in the rotation speed. This causes the length of the solar days to vary and the extraterrestrial objects to appear at slightly different positions in the horizontal coordinate system. To account for this, there are several different time scales, where the most important ones are listed below:

UT1 (Universal Time) is based on the actual rotation of the Earth with respect to the mean position of the Sun. Therefore the second has no fixed length. UT1 is suited to calculate the apparent position of an extraterrestrial object for an observer on the rotating Earth.

UTC (Coordinated Universal Time) is the primary time standard which has fixed seconds as determined by atomic clocks (TAI). UTC approximates UT1 by adding leap seconds if necessary so that the difference $DUT1 = UT1 - UTC$ is kept below 0.9 seconds.

TAI (International Atomic Time) is the basis for UTC and also has a fixed time for a second (SI second). The accuracy is maintained by averaging over 200 atomic clocks worldwide. The difference TAI - UTC changes every time a leap second is introduced in UTC, and is amounts currently +35 seconds (30th of June 2012).

DT (Dynamical time scale) is used for astronomical calculations. It has a fixed second (SI second) by definition, however takes into account relativistic effects, and therefore is dependent on the location. It is an ideal homogeneous time, therefore there may be deviations from TAI, which are very small however ($<10 \mu\text{s}$ in > 10 years). 1977 DT was defined as TAI + 32.184 seconds and therefore is +67.184 (July 2012).

JD (Julian Day) is the number (and fractions) of days since January 1, in the year 4713 BC in Greenwich at noon. E.g. 2451545.0 is January 1, 2000 at 12:00, and 2451545.5 is January 2, 2000 at 00:00. Julian Days are often used in astronomical calculations, as they are easy to calculate with. It is important to state to which time scale (UT1, UTC, DT, ...) the Julian Day refers to (JD_{UT1} , JD_{DT} , ...). A variant of the JD is the Modified Julian Day (MJD), which is defined as $MJD = JD - 2400000.5$ ⁵. There exist several web pages for transforming the Julian Day from a common date and vice versa^{6,7}.

LST (Local Sidereal Time) is a time scale based on the Earth's rotation measured relative to the vernal equinox (introduced in ch. 3.3.1 on page 29). The sidereal time is dependent on the observer's longitude, as it is defined as zero when the vernal equinox is above the observer's meridian. The Earth's precession movement is already accounted for in the Sidereal Time. The nutation, however, which also shifts the position of the vernal equinox is included in the Local Apparent Sidereal Time

⁵Julian day 2400000.5 corresponds to 17th of November 1858 at midnight.

⁶<http://aa.usno.navy.mil/data/docs/JulianDate.php>

⁷http://www.onlineconversion.com/julian_date.htm

(LAST) in contrast to the Local Mean Sidereal Time (LMST). The knowledge of the LAST is very useful in astronomical calculations when transforming from or into the horizontal coordinate system, as it directly gives the right ascension of the stars directly above the observer's meridian. The LAST can be calculated by

$$LAST = GMST + \Delta\psi \cdot \cos \varepsilon - Longitude \quad [3.4]$$

where $\Delta\psi$ is the longitude of nutation and ε the obliquity of the ecliptic. GMST (Greenwich Mean Sidereal Time) can be calculated by:

$$GMST = 280.46061837 + 360.98564736629 \cdot T \cdot 36525 \\ + 0.000387933 \cdot T^2 - \frac{T^3}{38710000}$$

and T is the centuries since 1st of January 2000 12:00 in UT1 ($T = \frac{JD_{UT1} - 2451545}{36525}$).

As the positions of extraterrestrial objects, when observed from the Earth's surface, depend on the true apparent rotational angle of the Earth, the UT1 time has to be used, as this is based on the Earth's rotation. However UT1 is not precisely available for present or future points of time. To get the exact time difference DUT1 = UT1 - UTC for days in the past, one can use data provided by the International Earth Rotation and Reference System Service (IERS) to get the desired DUT1 data⁸. Predictions for about 1 year into the future are also available⁹. The DUT1 values from 1972 to 2012 are given in Fig. 3.4.

3.3.3 Calculation of the solar position

The calculation of the apparent astronomical solar position in horizontal coordinates (elevation and azimuth), can be performed using the following steps:

1. Determine the heliocentric longitude and latitude of the Earth in the ecliptic coordinate system, and from this the geocentric solar coordinates in the ecliptic coordinate system.
2. Calculate the position of the sun in the equatorial geocentric coordinate system taking into account the nutation of the Earth.
3. Include the aberration, caused by the finite speed of light
4. Calculate the observer's position in geocentric coordinates and take parallax effects into account
5. Transform from geocentric equatorial to horizontal coordinates

To calculate the geocentric ecliptical coordinates of the Sun, one can use the VSOP87 theory by Bretagnon and Francou (1988) to calculate the heliocentric ecliptical position of the Earth. The geocentric coordinates of the Sun are then obtained by changing the signs of the Earth's coordinates. The VSOP87

⁸<http://hpiers.obspm.fr/iers/eop/eopc04/eopc04.62-now>

⁹<ftp://maia.usno.navy.mil/ser7/ser7.dat>

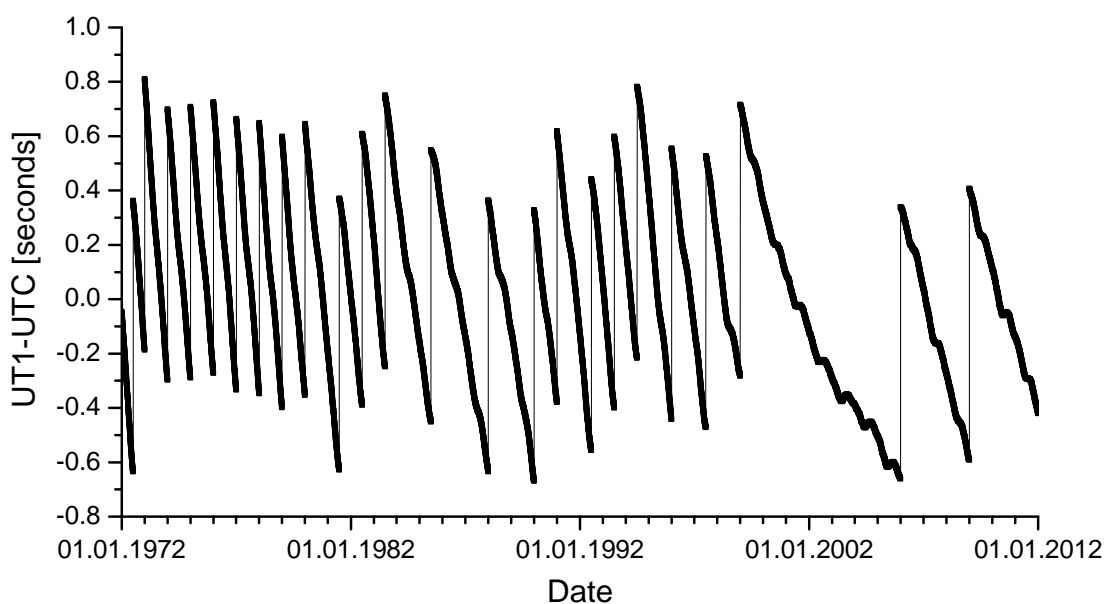


Figure 3.4: Difference between UT1 and UTC (source IERS). The vertical gaps appear upon introduction of a leap second. On average, the duration of one day is somewhat larger than 24 hours.

consists of thousands of periodic terms, which have to be evaluated for a given date and added up to give the desired astronomical coordinates. There are various versions VSOP87A-E, giving the coordinates in different coordinate systems and for different equinoxes. The version used within this work is the VSOP87D, giving the heliocentric coordinates of a planet at a given date: ecliptic longitude (L) and latitude (B) and distance from Sun (R), for the equinox at the given date. These terms take into account the influence of the Earth's precession, the moon and the other planets.

The terms look like:

$$L = 10^{-8} \cdot \sum_i \left(\sum_j A_{L_{i,j}} \cdot \cos(B_{L_{i,j}} + C_{L_{i,j}}) \right) \tau^i$$

where $\tau = \frac{JD_{DT} - 2451545}{365250}$, which are the millennia since the year 2000. JD_{DT} is the Julian Day in Dynamic Time. The parameters $A_{L/B/R_{i,j}}$ can be downloaded from the Internet (see Bretagnon and Francou (1988)). For this work, only the most important 195 terms were used which also were given in Meeus (1991), and provide an accuracy of better than an arc second for L and B which is, by far, sufficient for the purposes of atmospheric trace gas retrievals with the Sun as the light source.

The transformation from the ecliptic coordinate system to the equatorial coordinate system consists of a simple coordinate transformation. This is not constant as the equinoxes are not fixed due to the Earth's precession movement (see Sec. 3.3.1). Also, the obliquity of the ecliptic is variable which, however, can be calculated by a short formula with an accuracy of better than 0.01 arc seconds. In addition, the rotating Earth performs a nutation movement mainly caused by the influence of the Moon, which influences the

ecliptical longitude and latitude of all celestial elements. The nutation movement, however, is quite complex so that a huge number of oscillating terms has to be calculated.

When an observer moves perpendicularly to the observing direction, the apparent position of the observed object is displaced from its true position. This effect is called aberration of light, and results from the finite speed of light. It is directly proportional to the perpendicularly velocity. One can divide the aberration into several types such as the “annual aberration” caused from the movement of the Earth around the Sun and is of the order of 20 arc seconds. The “diurnal aberration” results of the rotation of the Earth, is dependent on the latitude of the observer and has a maximum value of 0.32 arc seconds. For the purposes within this work, it is sufficient to take into account the annual aberration only.

An observer on the Earth’s surface changes his position in space due the movement of the Earth around the Sun, but also due to its rotation. This effect causes a variation of the observing direction of extraterrestrial objects in the course of one day, and is called diurnal parallax. The size of this effect depends on the distance from the observer to the Earth’s rotation axis. For distant stars, this effect is very small, for the Sun this effect is up to about 9 arcseconds and for the Moon up to 2° . To calculate this effect, the observer’s geocentric orthogonal coordinates have to be taken into account. These include the geoid shape of the Earth as well as the observer’s latitude, height above the ground and Local Apparent Sidereal Time (LAST).

To calculate the solar angle in the observer’s horizontal reference system, a coordinate transformation has to be done, taking into account the observer’s latitude and LAST. The LAST is advantageously to be taken instead of the longitude to incorporate the variations of the Earth’s rotation.

To check the accuracy reached with this approach, the data was compared with the astronomical calculations from the Jet Propulsion Laboratory (JPL)¹⁰. As mentioned before, these data are available on-line only. Due to the need of solar position calculations during measurement campaigns and at remote sites without Internet access, a self-standing program based on the described algorithms is required. The difference of the currently implemented calculations with respect to the JPL values of more than 20 years are shown in the upper part of Fig. 3.5 on the facing page demonstrating an agreement within 0.25 arcseconds. This is by far sufficient for the purposes in solar absorption spectroscopy. If the DUT1 information is not taken into account or available (e.g. calculations for future times), good accuracy can’t be maintained. Omitting DUT1 information leads to errors in the elevation of up to ± 10 arcseconds for an observer at 49° latitude and up to 13.5 arcseconds for observer locations near the equator.

To reach the desired accuracy of 0.5% for the trace gas retrieval, a tracking accuracy of 19 arc seconds is desired as shown in section 3.2. Therefore, the true variation of the Earth’s rotation should be taken

¹⁰<http://ssd.jpl.nasa.gov/horizons.cgi>

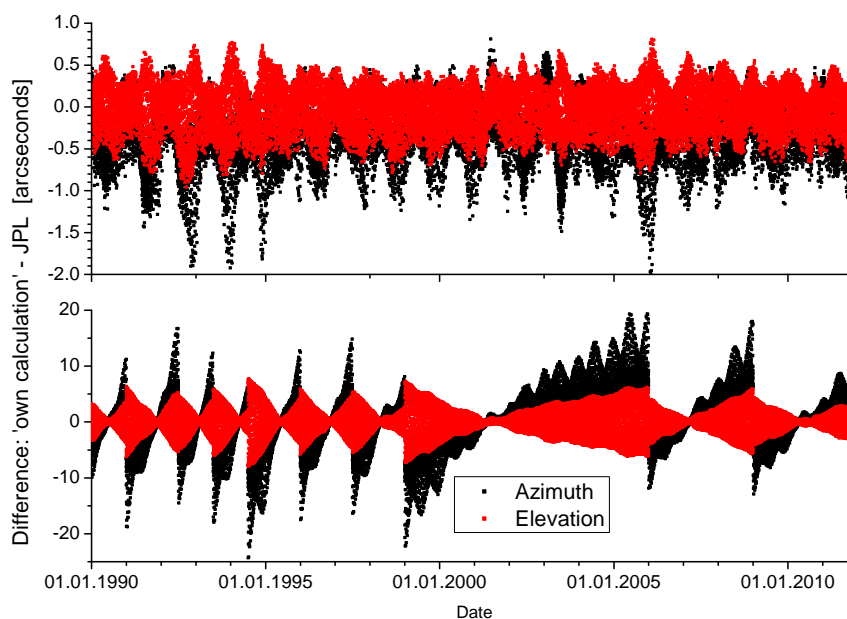


Figure 3.5: Difference of elevation and azimuth values of the Sun between our own calculation and JPL data. The upper graph shows the results including UT1 corrections having mean values of -0.02 ± 0.25 (1σ) and -0.3 ± 0.3 arcseconds for elevation and azimuth respectively. The lower graph simulates $DUT1 = 0$ ($=UT1-UTC$). The effect of introducing leap seconds which keeps $|DUT1| < 0.9$ seconds, can be seen nicely. The observer is located in Karlsruhe ($8.44^\circ E$, $49.1^\circ N$, 100 m asl).

into account for the retrieval. In the software developed within this work, this can be done easily by downloading a file from the IERS¹¹, which contains the UT1-UTC values.

3.3.4 Refractive index of air

To calculate the path of solar radiation propagating through the atmosphere, a good knowledge of the refractive index of air is needed. The refractive index depends mainly on the density of the atmosphere which can be calculated by the pressure and temperature, but also on other factors such as the composition of gases (humidity, CO_2 ,...) and also on the actual wavelength of the radiation. In literature several experimental values can be found which were used to create empirical formulas to calculate the refractive index. The most common ones were published by Ciddor (1996) and Edlén (1966) (of which updates were published by Birch and Downs (1993) and Birch and Downs (1994)). The formula given in the latter one is the following:

$$n_{Tp} - 1 = (n - 1)_s \cdot \frac{p}{96095.43} \cdot \frac{273.15}{T} \cdot \left[1 + 10^{-8} \cdot \frac{0.00972 \cdot T - 164.073}{p} \right] \quad [3.5]$$

¹¹<http://hpiers.obspm.fr/iers/eop/eopc04/eopc04.62-now>. This list is updated nearly daily and the values range up to about one month in the past.

where $(n - 1)_s$ is defined as:

$$(n_s - 1) \cdot 10^8 = 8342.54 + \frac{1406147}{130 - \frac{1}{\lambda^2}} + \frac{15998}{38.9 - \frac{1}{\lambda^2}} \quad [3.6]$$

The wavelength λ has to be given in μm , the pressure p in pascal, the temperature T in Kelvin. As one can see, the refractive index is in a good approximation, proportional to p/T . For moist air, with a partial pressure f in Pascals of water vapor, the dry refractive index n_{Tp} has to be further modified:

$$n_{Tpf} = n_{Tp} - f \cdot \left[3.7345 - 0.0401 \frac{1}{\lambda^2} \right] \cdot 10^{-10} \quad [3.7]$$

These formulas were derived from lab measurements in the visible and near-infrared spectral range (0.2 to $2\mu\text{m}$). As there are only very few experimental data available for longer wavelengths (such as Matsumoto (1982) for $3.4\mu\text{m}$ and Marchetti and Simili (2006) for $10.57\mu\text{m}$), in the Mid-Infrared (MIR) used in the NDACC, the accuracy of formula 3.5 is limited. In addition, there are many strong absorption bands in the MIR causing the refractive index to vary very strongly so that it can't be described by a simple formula.

To get information about the refractive index in the MIR, efforts were made to calculate the dispersion of air based on the HITRAN spectroscopic database (Mathar (2004) and Mathar (2007)). This is possible because each spectral line contributes a change of the refractive index n , as illustrated in figure 3.6. Therefore n often is written as a complex refractive index $n = n' + i\kappa$, where the imaginary part κ describes the absorption and n' the refractive index. n can be calculated as:

$$n' - 1 \propto \frac{(\omega_0^2 - \omega^2)}{(\omega_0^2 - \omega^2)^2 + \gamma^2 \omega^2} \quad [3.8]$$

$$\kappa \propto \frac{\gamma \omega}{(\omega_0^2 - \omega^2)^2 + \gamma^2 \omega^2} \quad [3.9]$$

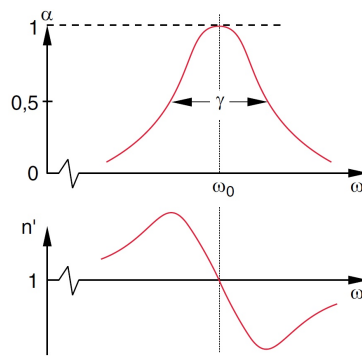


Figure 3.6: Absorption coefficient $\alpha = 2\omega_0/c \cdot \kappa$ and real part n' of the refractive index in the vicinity of a spectral line of width γ located at frequency ω_0 . Image taken from Demtröder (2009)

Using the freely available C++ source code written by Richard Mathar and the HITRAN2008 database, calculations were made for comparison. As one can see in figure 3.7 on the next page, the “Edlen” equation agrees quite well with the “Mathar” calculations in the visible and the near infrared (NIR). The

differences become bigger below 3000 cm^{-1} when strong absorption bands distort the smoothly varying function. However, for the purposes of atmospheric refraction, these effects are negligible (see section 3.3.5).

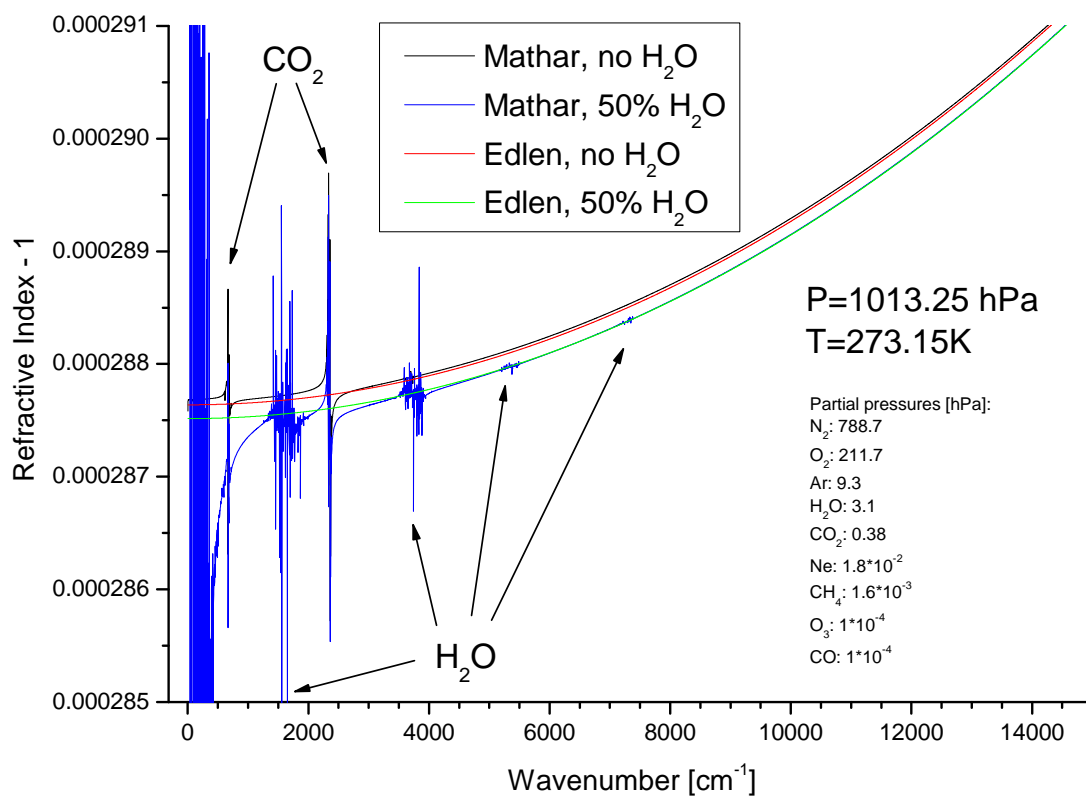


Figure 3.7: Calculations of the refractive index of air with the “Edlen” equation and the “Mathar” calculation for air with zero and 50% relative humidity at 1013 hPa and 0°C. The constituents given in the inlay refer to the wet air case. A zoom into the water vapour signature around 1600 cm^{-1} is shown in Fig. 3.8.

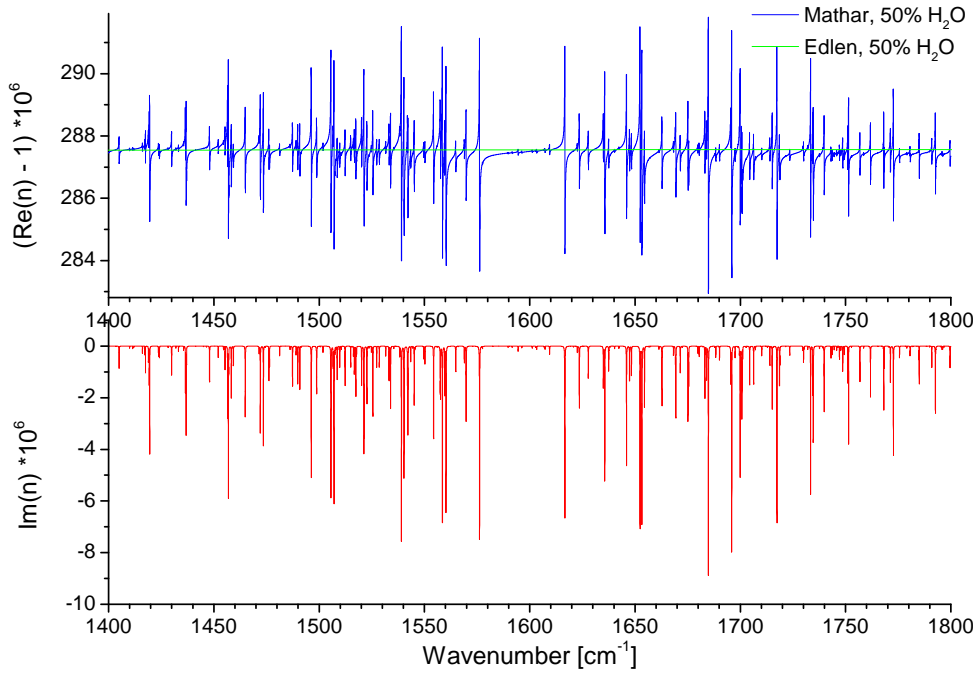


Figure 3.8: Zoom into Fig. 3.7, showing the refractive index values calculated by the Edlen equation and the Mathar calculations at 50% H₂O. In the vicinity of spectral lines, which are shown in the lower graph, the refractive index shows the expected asymmetric features. The y-axis, which is κ from equation 3.9, is linked to the absorption coefficient α in Lambert-Beer’s absorption law by the formula $\alpha = 4\pi\kappa\tilde{\nu}$.

3.3.5 Refraction

When the solar radiation propagates through the atmosphere towards the observer on the Earth’s surface, the light path does not follow a straight line. Instead, the variable refractive index causes an effect called refraction, resulting in a bending of the path, so that extraterrestrial objects appear higher above the horizon as they would without atmosphere. The size of the refraction depends on the elevation angle of the incoming light and is about 1 arc minute at 45° elevation and ranges up to about 35 arc minutes for light coming from the horizon. As the Sun has an apparent diameter of about 0.5°, it causes the surprising effect, that the solar disk appears completely above the horizon when, in reality, it is below the horizon. To calculate the effect of refraction, different methods can be used. A simple formula was published by Þorsteinn Sæmundsson (1986), which gives an empirical approximation of the refraction:

$$R = \frac{1.02}{\tan\left(h + \frac{10.3}{h+5.11}\right)} \cdot \frac{P}{1010} \cdot \frac{283}{T} + 0.0019279 \quad [3.10]$$

where R is the refraction in arc minutes, h the true elevation in degrees, P the ground pressure in mbar and T the ground temperature in Kelvin.

In order to calculate the refraction more precisely, a full ray-tracing model of the atmosphere can be used. One was developed by Hase and Höpfner (1999) which uses a temperature-pressure-profile of the

atmosphere and determines the bending of the ray at each position along the trajectory according to the local gradient of the refractive index. The results of this method are shown in figure 3.9 for Kiruna on a number of days from January 2007 to May 2011.

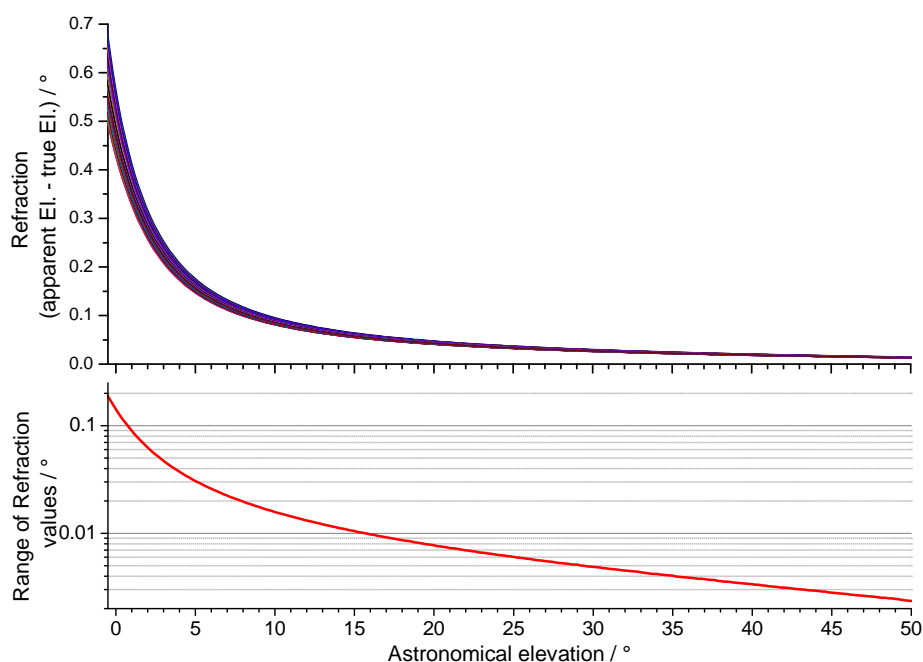


Figure 3.9: Refraction calculated by the model by Hase and Höpfner (1999) for the p-T-profiles of 355 measurement days in Kiruna from January 2007 to May 2011. The variations in the refraction values resulting from varying pressures and temperatures are about one arc minute for 10° elevation and range up to 11 arc minutes for -0.5° astronomical elevation. At this elevation, the center of the refracted solar disk appears approximately at the height of the horizon.

When comparing the full ray tracing model with the approximation of equation 3.10, one finds that the differences increase for decreasing elevation angles. They remain below 25 arc seconds down to 6° elevation. Below 3° the differences increase rapidly, e.g. ± 75 arc seconds for 0° , which shows the ultimate limit of the approximation. To keep the differences for elevation angles above 5° smaller 5 arc seconds, a modification to the simple formula can be used, derived from the previously mentioned 355 measurement days in Kiruna, by adding an exponential part:

$$R = \frac{0.96052}{\tan\left(h + \frac{8.73457}{h+4.55868}\right)} \cdot \frac{P}{1010} \cdot \frac{283}{T} \cdot e^{-\frac{h-12.86618}{1536.2745}} + 0.00267 \quad [3.11]$$

The differences between these formulas (eqns. 3.10 and 3.11) and the full ray-tracing model are shown in figure 3.10 on the next page.

The effect of the wavelength dependent dispersion of air on the refraction is shown in table 3.1, the effect on the air mass in table 3.2. Compared to the effects from the varying pressure and temperature, it is very small. Therefore, for most cases it is sufficient to use a very simplified form of the Edlen equation 3.5 for refractive index variation, such as $(n - 1) \propto p/T$.

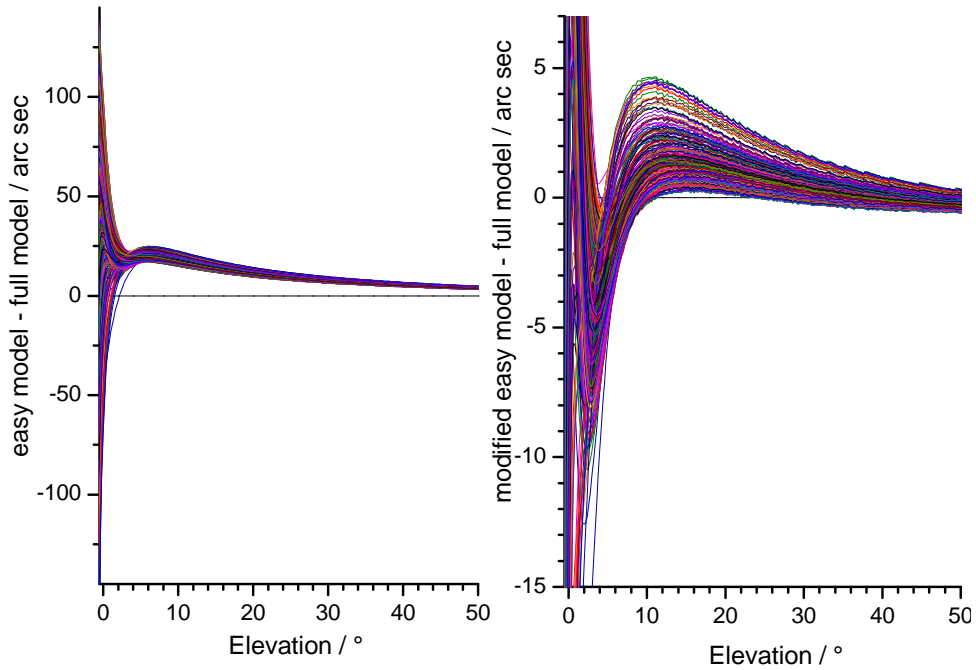


Figure 3.10: Difference of the empirical refraction formula with the ray-tracing calculation. Left: equation 3.9 on the previous page, right: modified empirical formula (eqn. 3.11).

Astron. SZA	refractive index in arc minutes		
	@14000 cm ⁻¹	@8000 cm ⁻¹	@1000 cm ⁻¹
50	-1.115	-1.107	-1.103
60	-1.617	-1.605	-1.599
70	-2.55	-2.53	-2.52
80	-5.11	-5.07	-5.05
90	-28.3	-28.1	-28.0

Table 3.1: Refraction values for three wavenumbers in arc minutes. The used refractive indexes for 0°C and 1013.25hPa are 1.00029079, 1.00028860 and 1.00028758 as calculated from the “Edlen” formula 3.7 for 30% relative humidity. The pressure- and temperature-dependency was calculated by the simple p/T scaling approach. A mean pressure-temperature profile for Kiruna was used.

3.3.6 Apparent air mass

The effort to investigate the refraction in the atmosphere is driven by the need to calculate the air mass the radiation passes along a given line-of-sight to the observer. This air mass is needed to calculate a total vertical column or a volume mixing ratio of a desired gas, as erroneous values are directly related to the retrieved gas column.

The effect upon the calculated air mass introduced from a mispointing of the tracker was shown in Fig. 3.1 on page 27. The effect from the refraction is shown in Fig. 3.11 for an average p-T-profile in Kiruna. Although the error is smaller than 0.5% for a tropospheric gas below a SZA of 77° , it should be considered in the retrieval as neglecting the refraction would give systematically lower gas column values.

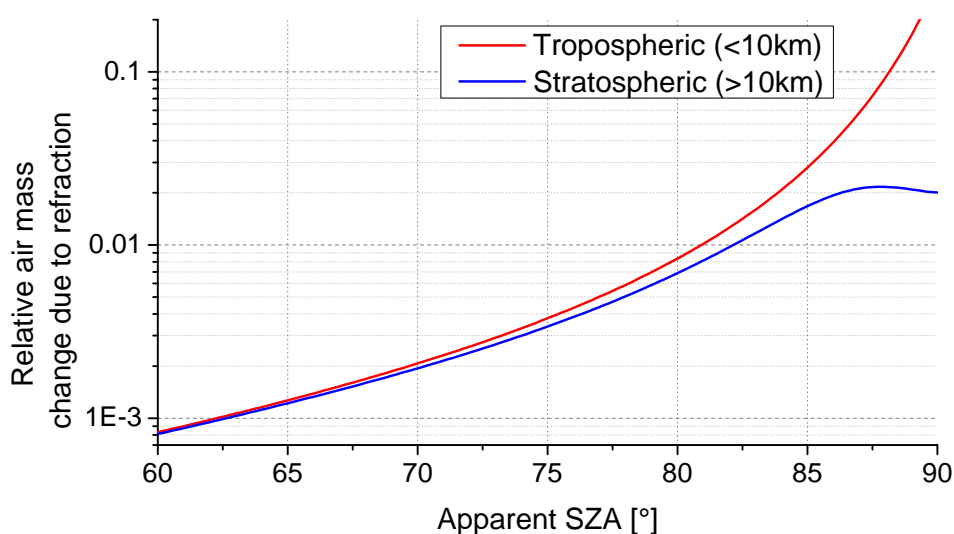


Figure 3.11: Change of the observed air mass induced by refraction.

The size of the errors onto the air mass, when neglecting the wavelength dependency of the refraction was not yet investigated. For this reason, it is examined in this section. The way to calculate the correct air mass is sketched in Fig. 3.12: The solar-zenith-angle of the spectrometer's pointing direction is determined by the optical feedback of the tracker, at least as long as the solar disk is centered ideally on the input aperture stop. This feedback, which can be a camera or a quadrant diode, often use the visual part of the spectra. As the refraction is dependent on the wavelength, the NIR or MIR ray path relevant for the airmass of the measured spectrum, differs from the visible ray path. The angle at the observer is the same, but the visual ray path is slightly more bent. Therefore, when calculating the SZA for a specific spectrum based on it's recording time, the refraction has to be calculated from the solar position using a refraction based on the refractive index of air which is correct for the spectral range used by the optical feedback of the tracker. When evaluating the spectra, the ray path, and therefore also the effective air mass, has to be calculated starting at the ground with the previously calculated apparent SZA, but

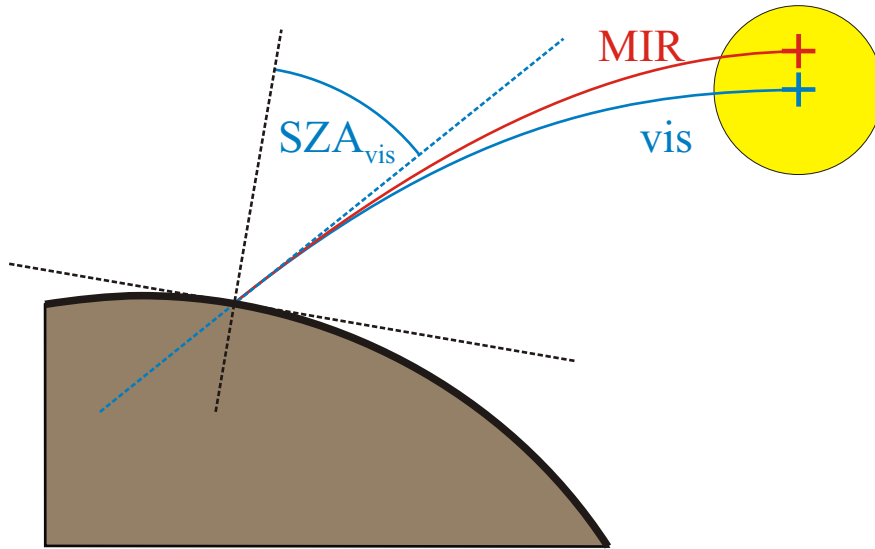


Figure 3.12: Scheme of the ray path in the infrared (MIR/NIR) with an optical tracker feedback operating in the visual range of the spectrum.

applying the refractive index for the actual measurement range in the NIR or MIR.

The size of this effect is shown in table 3.2. As it turns out to be smaller than 0.01% up to 80° SZA, it can be neglected, as it is at least 1 order of magnitude smaller than other errors occurring in the atmospheric trace gas retrieval. Nevertheless, it is included in PROFFIT, in case it may become important for future applications.

refracted SZA	14000 cm ⁻¹ → 8000 cm ⁻¹	14000 cm ⁻¹ → 1000 cm ⁻¹
70	0.006‰/ 0.01‰	0.008‰/ 0.02‰
80	0.02‰/ 0.05‰	0.03‰/ 0.08‰
90	0.7‰/ 0.4‰	1.1‰/ 0.6‰

Table 3.2: Relative change in observed air mass below and above 15km caused by different wavenumbers. The ray paths start with the given refracted SZA from the ground. The parameters are the same as in table 3.1.

3.4 Finite duration of measurements

As the Sun moves in the sky while taking a measurement, the air mass and therefore the trace gas under investigation which is detected by the instrument, changes. At high elevation angles, this effect is negligible. However, for low-latitude sites at low elevation angles, the variable slant column may cause an error in the retrieval result. In addition, the background continuum transmission of the observed atmosphere changes due to the variable air mass while a single measurement is taken, which may have an

additional effect. The simulation of this effect is complex, as the FTIR records interferograms, not spectra. Therefore, different sections of the IFG correspond to different solar elevation angles and therefore to variable trace slant columns. In order to achieve a first approximate estimation whether the mentioned effects affect the trace gas retrieval, in this work a simplified situation is investigated. It is assumed that a measurement which may take a certain time to complete, is an average of single and undisturbed sequentially recorded spectra. Up to a certain degree this approach is realistic, as the measurements done in Karlsruhe, Izaña and Kiruna are averages of 4 to 6 interferograms, of which each corresponds to a single spectrum.

To do the investigation, single spectra with constant atmospheric CO₂ volume mixing ratios (VMRs) (396.6 ppm) were simulated using PROFFIT for time intervals of 30 seconds over a time period corresponding to SZAs from 70 to 90 degrees. The simulated spectral range encompasses the two CO₂ windows around 6300 cm⁻¹ which are used in the TCCON (see section 6.4.3 on page 106). On these spectra a moving average was applied, containing a certain number of spectra, so that the resulting averaged spectra then represent longer measurement durations. For example, averaging 4 spectra corresponds to a duration of 2 minutes. When analyzing these simulated averaged spectra with PROFFIT, the solar zenith angle was calculated for the middle of the measurement, as is done in practice.

This procedure was made for a day in Karlsruhe (10th of April 2010) and Addis Ababa (30th of August 2011). Addis was chosen as its low latitude gives high rates of changes of the solar zenith angle. The resulting changes in the effective air mass are presented in Fig. 3.13 for both days and sites, where the values for Addis are about 1.5 times higher.

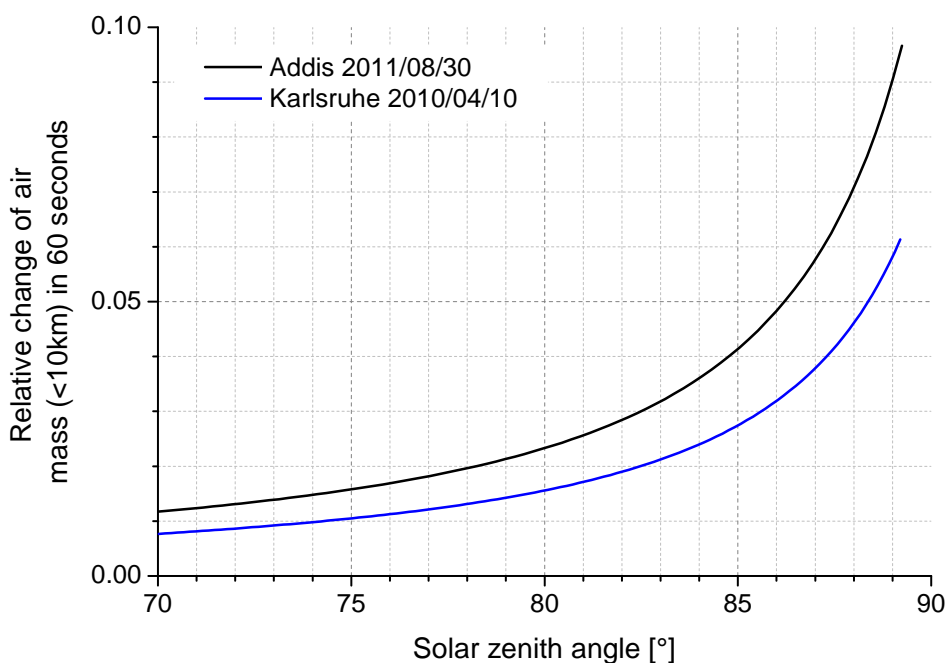


Figure 3.13: Change of the tropospheric air mass (<10 km) per minute at a given apparent SZA. Compared to Fig. 3.1 the values rise less rapidly towards higher SZAs due to the increasing effect of refraction.

The effect of extended measurement times on a CO₂ retrieval result are shown in figures 3.14 and 3.15 for Karlsruhe and Addis, respectively. The lower panels show the solar zenith angle as function of time. In Karlsruhe, only the 10 minutes average lead to errors above 0.1%. The CO₂ errors for TCCON measurements, which are recorded in Karlsruhe with a 3.5 minutes average, never exceed 0.05%. So these are well within the desired accuracy of TCCON.

At the site in Addis Ababa, the errors are much greater, as could be expected from the faster ascends and descends of the Sun near horizon. A 10 minutes average results in an error of 0.1% already at 73° SZA. The 0.05% error range for Karlsruhe-like TCCON measurements is exceeded above about 80° SZA.

To conclude, for up to about 3.5 minutes the errors are acceptable. Above 5 minutes recording time, the errors become greater than 1% above 80° SZA, so this duration should not be exceeded when making measurements at low latitude sites. For example, the standard high-resolution MIR measurement setup of Kiruna is not suited for low latitude sites at low SZAs, as the measurement take up to 10 minutes due to averaging 4 interferograms.

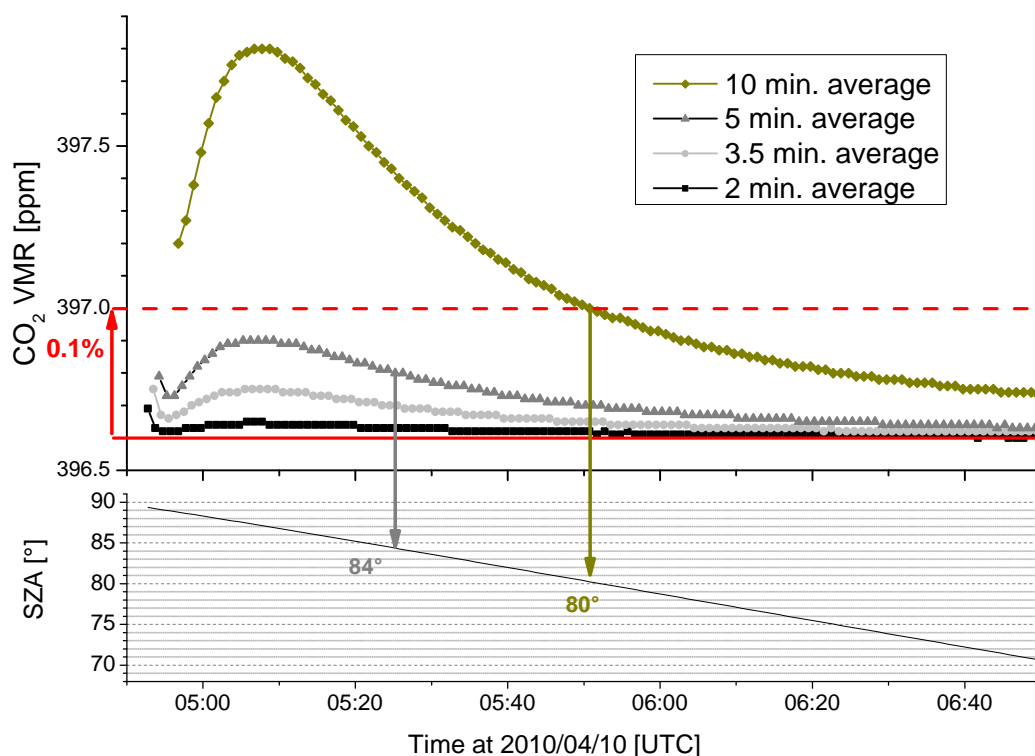


Figure 3.14: Effect of averaging measurements at the site in Karlsruhe at 10th of April 2012. The unaltered CO₂ VMR value is 396.6 ppm.

The transmission of the atmosphere decreases for increasing SZA values due to the increasing air mass the solar radiation is passing. For example, near the horizon the air mass is about 40 times higher as in zenith direction. This variable opacity caused by the continuum absorption of the atmosphere is currently not considered in the retrieval. To include this effect, an opacity of 0.055 was estimated for a sample

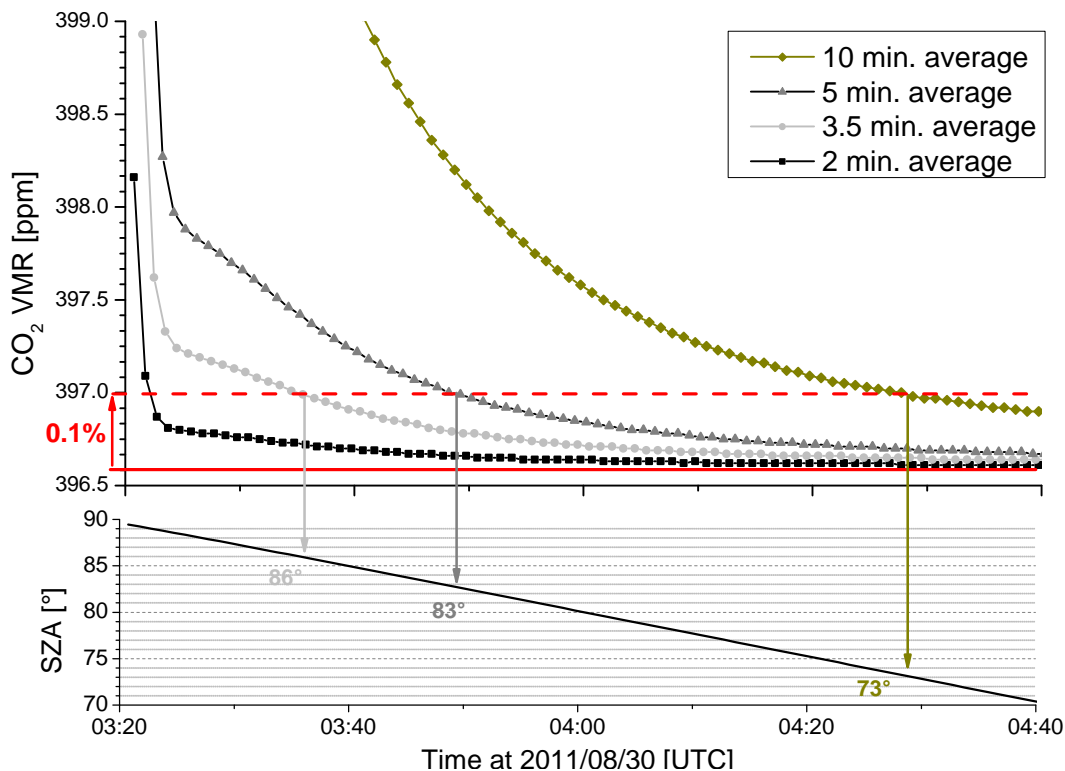


Figure 3.15: Effect of averaging measurements at the low latitude site in Addis Ababa at 30th of August 2011.

day at a wavelength of 5956.363 cm^{-1} (using the formula $\text{transmission} = e^{-\text{opac} * \text{AM}}$ with AM being the respective air mass relative to the air mass in zenith direction). This value was then used in the forward calculations. The effect in the CO_2 retrieval was a reduction of the errors of about 13% at 75° SZA, 25% at 80° SZA and 42% at 85° SZA. Obviously the increasing opacity helps in reducing the errors induced from long measurement times.

These effects can be understood, as the retrieval errors from long measurements mainly are the result from a non-linear variation of the air mass (which behaves approx. like $1/\cos(\text{SZA})$ as can be seen from Fig. 3.1). Therefore the half of the measurement with lower SZA observes air masses disproportionately higher than the other half. When including an opacity, the influence of the high air mass spectra is reduced, which leads to a decrease of the errors.

As shown, these effects are negligible for many common cases of solar absorption spectroscopy. However, they pose a systematic error source, which can be removed if higher accuracies are required in the future. A correction can be performed, for example by using effective measurement times instead of the mean times, or effective air masses. The determination of these effective values is not trivial, as they depend on many factors such as the ascending or descending rate of the Sun, the duration of the measurement, the continuum opacity, but also the vertical distribution of gas under investigation in the atmosphere.

3.5 Correction of source intensity variations

Resulting from limitations by the analog to digital converters (ADC), especially the limited dynamic range, traditionally the recorded interferograms were high-pass filtered before being converted to digital values. The IFG values then are centered around 0 which simplifies the recording and usage of IFGs with variable detector gains (gain-switching), e.g. low gain for the centerburst region and higher gain in regions with large OPD, to make a better use of the dynamic range. In addition, many ADC which are in use were designed to record values symmetrically around 0.

In the simplest case, in the absence of source brightness fluctuations (SBF) within the course of recording one IFG, the AC coupling is an appropriate method. However, for ground-based measurements with the Sun as the light source, the source intensity can be regarded as constant at very clear days only. On most days, SBF due to thin (cirrus) clouds or fog, are rather common. The effect of a passing cloud is a multiplicative reduction of the IFG amplitude causing a distortion of the spectrum. The type of distortion depends on the position of the amplitude reduction in the IFG, as the region around ZPD determines the continuum level and the regions with higher OPD determine the high-frequency part of the spectrum and therefore the shape of the narrow absorption lines.

Up to a certain degree, these effects can be corrected with the knowledge of the SBF, which can be estimated by recording the direct, unfiltered detector signal (DC coupling), as this contains both the spectral information and the underlying slowly varying source brightness fluctuations. This usage of the DC IFG values was proposed by James W. Brault and Luc Delbouille in 1980s. However, only after the availability of low-cost ADCs with a significantly higher dynamic range (24bit) about 10 years ago, gain switching became unnecessary and this recording scheme became common for solar FTIR measurements. It was also driven by the precision requirements of the TCCON (see section 2.2.3) and Keppel-Aleks et al. (2007)). The publication by G. Keppel-Aleks investigates a possible correction procedure in detail and also estimates effects such as the fact, that the scattering of clouds and aerosols in the atmosphere depends on the wavelength of the light, resulting in unknown non-gray SBF.

To make use of the DC interferogram, for the standard pre-processing of the retrieval program PROFFIT (see section 2.2.2 on page 19, a suitable SBF correction (later on called “DC correction”) algorithm was implemented within this work. It is performed in the framework of the PROFFIT specific pre-processing (“calibration”) and will be presented shortly in the following.

As the frequencies of the SBF in the IFGs are much lower compared to the frequencies corresponding to the wanted spectral information, it is possible to separate these two parts. In the PROFFIT calibration the source intensity is estimated by applying a moving average to the IFG several times, suppressing the high frequency spectral information and giving a smoothed interferogram (IFG_{sm}). A division of the original IFG (IFG_{orig}) by IFG_{sm} then leads to a normalization of the amplitude over the entire IFG and also cancels out the low-frequency part. The formula used is:

$$IFG_{corr} = (IFG_{orig}/IFG_{sm} - 1) * DC_{offset} \quad [3.12]$$

The resulting corrected IFG is similar to an AC coupled IFG, but corrected for SBF. The scalar multiplier “ DC_{offset} ” ideally is the real DC offset of the IFG in case of no clouds, which has to be multiplied to preserve the original IFG amplitude. In highly distorted IFGs the true value cannot be retrieved, which however causes an erroneous scaling factor in the spectral domain only. In the current implementation the DC_{offset} value is retrieved in a region around the IFG centerburst, as this region in the IFG determines the general shape of the spectrum. A schematic overview of the correction is shown in Fig. 3.16, while in Fig. 3.17 an example using a real interferogram is presented.

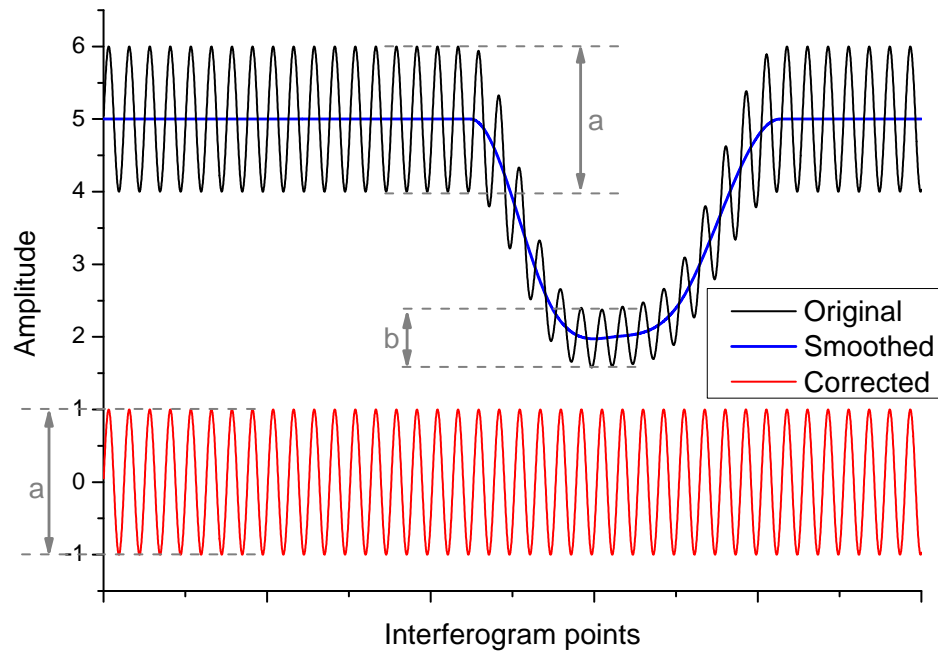


Figure 3.16: Scheme of the DC correction. For simplification, a pure sine function is used. The “measured” IFG has a lower amplitude (b) in areas with lower source intensity. By the division with the low-frequency (“smoothed”) signal, subtraction of 1, and a following multiplication with the “true” DC offset (here 5), the original IFG is recovered (of course with a lower signal to noise ratio in the distorted regions).

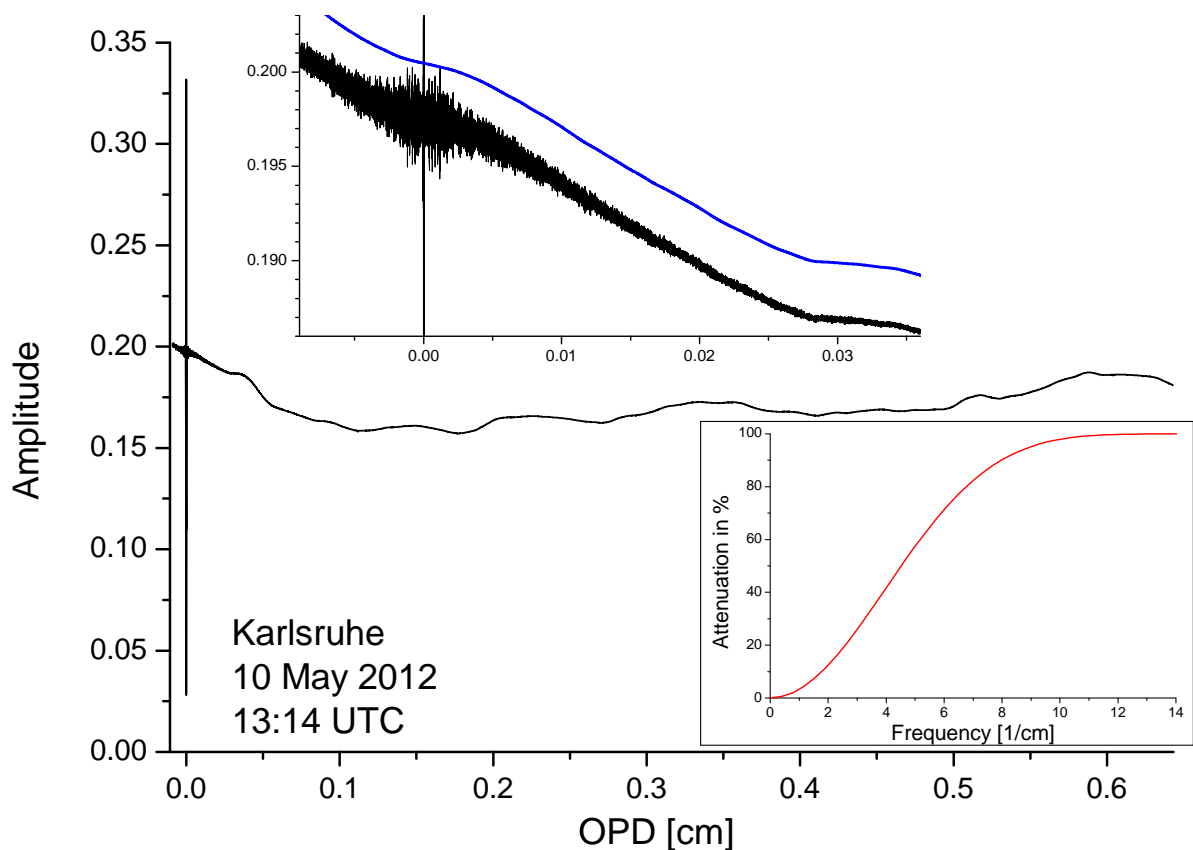


Figure 3.17: Example of a real interferogram recorded by the TCCON instrument in Karlsruhe which shows intensity variations due to thin clouds. The smoothed IFG is shown as a blue curve in the upper graph (for visualization reasons with a constant offset of +0.003), which is a magnification around the centerburst region. The attenuation characteristic of our smoothing kernel is shown in the bottom right corner.

In figure 3.18 O₂ and CO₂ retrieval results for IFGs recorded at the Karlsruhe site are shown. On this day (23th of May 2010) thin cirrus clouds distorted the solar intensity. The maximum distortion of the IFGs are similar to the IFG shown in Fig. 3.17. The DC correction has an impressive effect on the accuracy of the retrieved gas concentrations.

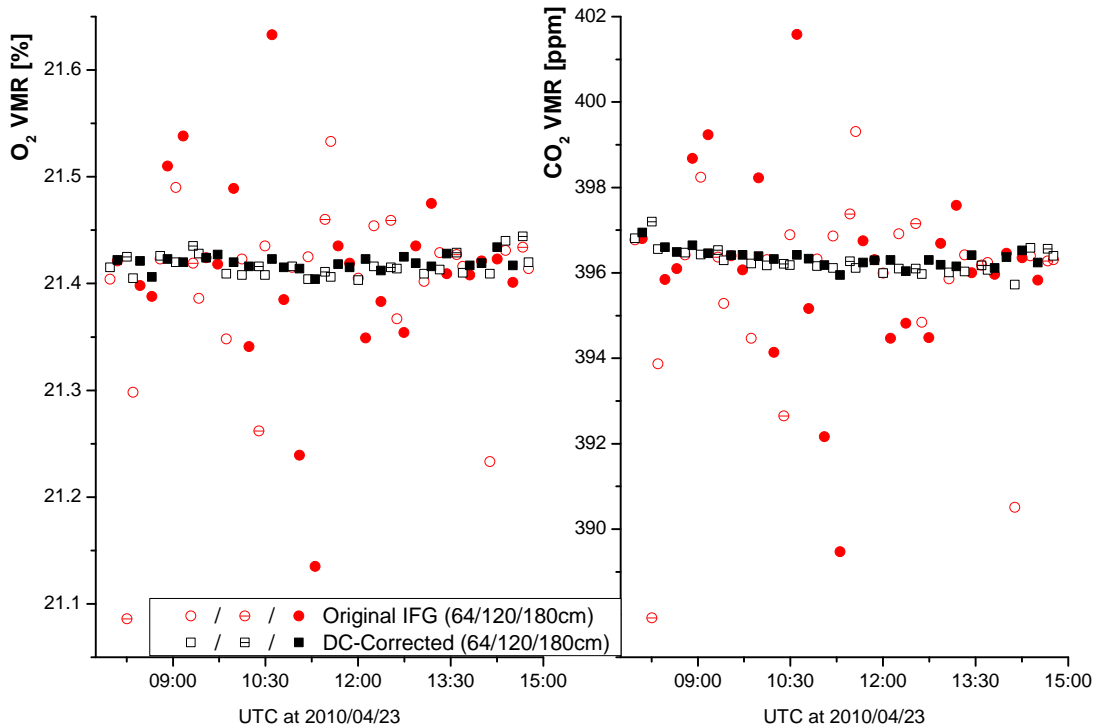


Figure 3.18: PROFFIT retrieval results for a measurement day with thin cirrus clouds, without and with a correction for the solar intensity variation of the measured interferograms. The respective standard deviation values differ by a factor of 10. The IFGs were recorded with the InGaAs detector, with optical path differences between 64 and 180 cm.

3.6 Sampling-Ghost artifacts

Fourier transform spectrometers pose stringent requirements on the accuracy of the interferogram sampling position. As noted above in section 2.1.1, the moving mirror position is commonly detected and controlled by detecting interference patterns from a monochromatic laser, which also passes through the interferometer. Periodic systematic errors, expressed as a fraction α of the IFG sampling interval, generate so-called “Frequency Modulation Ghosts”. These are artifacts in the spectrum that have the shape of the original spectral features, multiplied by a factor $\pm\text{GPR}$ (Ghost-to-Parent ratio) and located with an offset of $\pm n \cdot \tilde{\nu}_{err}$ with respect to the original spectral position ($n=1,2,3,\dots$). In case the periodic errors appear in space domain (e.g. at every HeNe laser fringe position), $\tilde{\nu}_{err}$ is the wavenumber corresponding to this periodicity. For periodic errors in the space domain with a frequency f_{err} (e.g. from

mechanical vibrations or the external power line frequency of 50 or 60 Hz), $\tilde{\nu}_{err}$ can be calculated by $\tilde{\nu}_{err} = \tilde{\nu}_{HeNe} \cdot f_{err} / \nu_{sc}$, where $\tilde{\nu}_{HeNe}$ denotes the wavenumber of the laser, ν_{sc} is the scanner frequency (number of HeNe laser wavelengths change in OPD per second). The GPR can be calculated using the sampling step Δ by the formula: $GPR = \pi \cdot \tilde{\nu}_{err} \cdot \alpha \cdot \Delta$. Further details about the theory of ghost artifacts can be found in Learner et al. (1996), Guelachvili (1981) and Davis et al. (2010). If the spectral region of the ghost artifacts is not in between the low- and the high folding limit, it is aliased (folded back) in the original spectral region, as schematically displayed in figure 3.19.

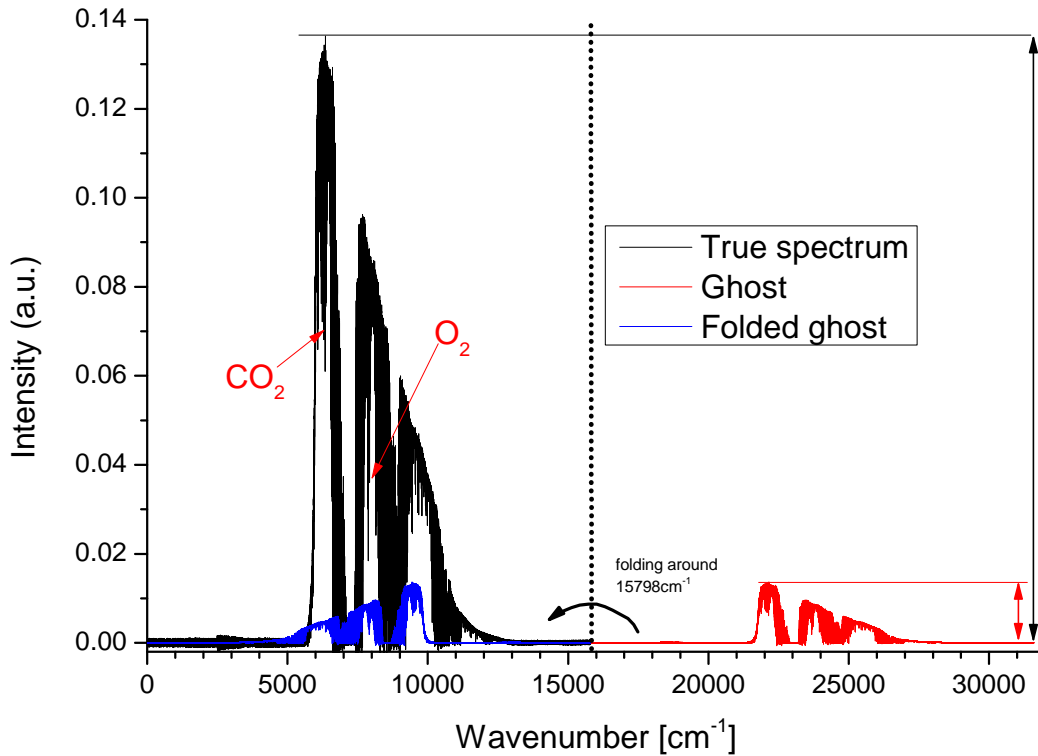


Figure 3.19: Schematic illustration of a ghost artifact (with $n=1$) in the NIR with a high folding limit and a value of $\tilde{\nu}_{err}$ of 15798 cm^{-1} . The spectrum retrieved from the missampled IFG is the sum of the black real spectrum and the blue folded ghost. For illustration reasons a very large Ghost-to-Parent ratio of 0.1 was used.

The IFS125HR spectrometers used in the TCCON suffered significantly from IFG sampling errors when measuring in the NIR spectral range (Messerschmidt et al., 2010), before an electronic upgrade became available in 2011. In the NIR, the desired high-folding limit is above 7900 cm^{-1} , so it is not sufficient to sample every rising edge of the HeNe reference laser operating at 15798 cm^{-1} , as it can be done in the MIR. Instead, every rising and falling edge of the sinusoidal HeNe signal has to be detected. In the IFS125HR this is done by a comparator detecting the zero crossings of the HeNe signal. An erroneous setting of the voltage at which the comparator switches causes non-equidistant sampling intervals as shown in figure 3.20, and a $\tilde{\nu}_{err}$ of 15798 cm^{-1} , leading to the situation described in Fig. 3.19.

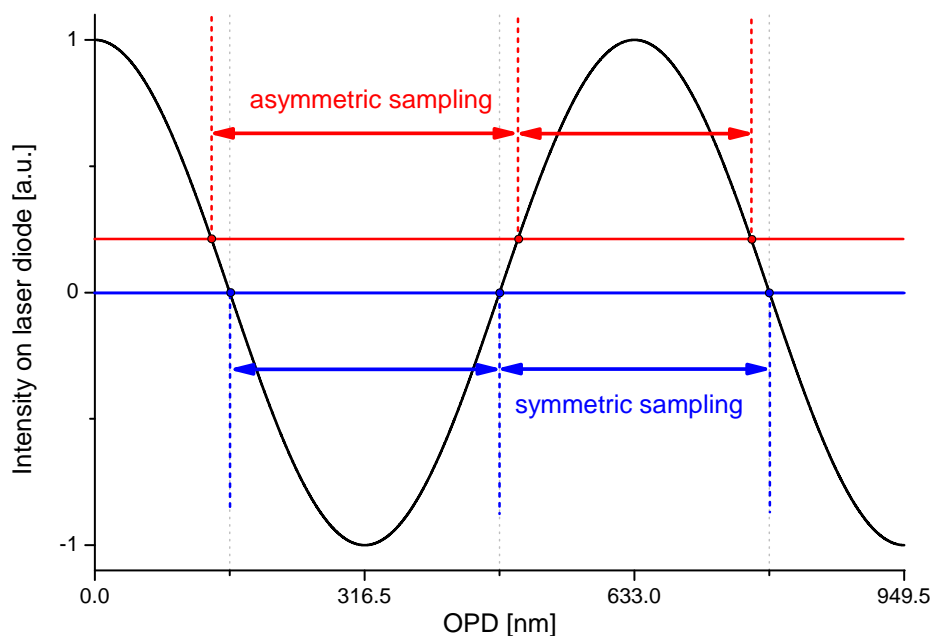


Figure 3.20: The AC signal of a HeNe reference laser. In the ideal case, the rising and falling edges are detected at 0 (blue). An offset in the internal comparator introduces systematic changes of the sampling intervals (red).

In general, the switching value of the comparator (in the ideal case 0V) can be adjusted manually by a potentiometer, to ensure equidistant sampling. This procedure, determined by minimizing the ghosts in a measured spectrum, then compensates for numerous electronic and optical error sources. For example, these can be non-linearities of the laser diodes causing a distortion of the sine shape, the alignment of the laser, but also distortions of the sine shape due to digital sampling electronics, leading to a different behavior of rising and falling voltages. However, the downside of this approach is, that it is dependent on the chosen scanner speed and the laser amplitude. A different scanner velocity, a degrading HeNe laser intensity or a realignment of the interferometer requires a retuning of the potentiometer.

To further reduce the sensitivity of the adjustment, the electronics upgrade includes an exchange of the prior laser-detectors, which suffered from nonlinearity effects.

3.6.1 Correction of ghost artifacts

The TCCON recommends a GPR value below ($1 \cdot 10^{-4}$) for the used IFS125HR spectrometers, in order to keep the desired level of accuracy in the gas retrievals as low as a few tenth of a percent. For example, at the site in Kalsruhe the GPR is in the order of $1 \cdot 10^{-5}$. However, for the time before the laser diode upgrade in 2011, the TCCON spectra of most stations show values significantly higher than $1 \cdot 10^{-4}$. Despite the ratioing with the O_2 column, the TCCON XCO_2 retrieval is not independent of the ghosts,

as the intensity and shape of the ghost signal differs between the CO₂ and the O₂ retrieval range, which can be seen in figure 3.19.

Recently F. Hase proposed a correction scheme, which can be used to reduce the ghosts in the spectra. As the spectrometer in Karlsruhe was equipped with the linear laser diodes from the beginning of operational measurements and therefore shows a very small GPR, and the instrument in Izaña poses additional complications (as will be shown in this section), spectra provided by V. Sherlock at the NIWA¹² were used for testing the new algorithms. The NIWA instrument in Lauder (NZ) has a long time series of spectra showing ghost artifacts, which is a ideal basis for testing and improving the ghost correction algorithm. Currently, a publication is in preparation (see Dohe et al. (2012/2013)) describing the procedures and results.

The basis of the ghost correction scheme is to determine and to correct the erroneous sampling shift α of every second point in the interferograms. For most spectra the mis-sampling can be determined in opaque spectral regions such as the 7290 to 7360 cm⁻¹ region recorded at a large SZA, as displayed in Fig. 3.21. A repeated testwise resampling of a low-resolution apodized double-sided IFG is performed to minimize the value in the nearly opaque spectral range. The associated ghost parent region is 8440 to 8510 cm⁻¹, which offers reasonable signal levels.

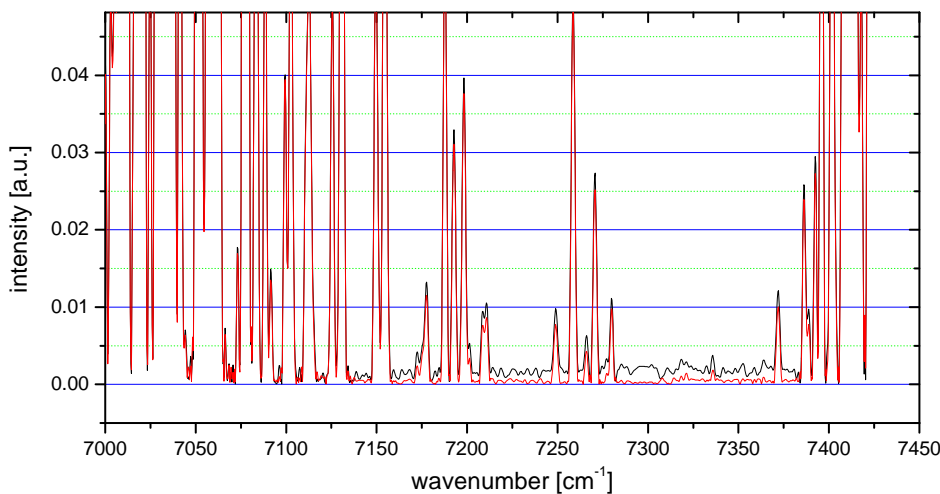


Figure 3.21: Spectral region which is nearly opaque due to strong water absorption features. Black: Original spectrum with an offset originating from underlying ghost features. Red: Corrected. The corresponding IFG was supplied by V. Sherlock (NIWA).

The apparent sampling error then can be determined by minimizing the mean flux in the opaque regions by “shifting” every second point in the IFG using a sinc-interpolation. A sample plot of mean fluxes for 2 spectral regions versus a variable sampling error is displayed in Fig. 3.22.

¹²<http://www.niwa.co.nz/>

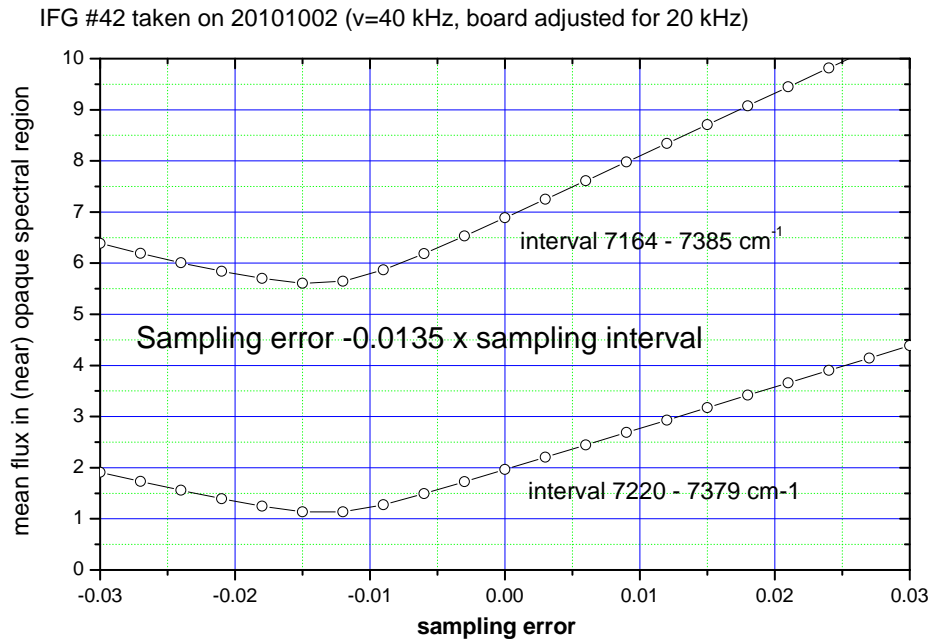


Figure 3.22: Flux in near opaque spectral regions for different sampling position in the IFG domain. The sampling error in this example is about 1 %, which is as low as 4 nm in the optical path difference. The IFG was recorded in the TCCON station Lauder in New Zealand and provided by V. Sherlock. (Plot courtesy of F. Hase.)

In general, it can be assumed that the missampling is stable on shorter timescales and jumps occur upon intervention such as realignments, laser exchange, etc. Therefore, the proposed procedure is to detect time series of similar sampling offsets by analyzing sample spectra with high SZA, and to correct the IFGs in each timeseries with the same sampling offset.

To calculate the interferogram with “shifted” values for every second datapoint, the IFG can be resampled by convolution with a sinc-like function. This should be apodized, e.g. with a cosine, to ensure a smooth fadeout at the ends of the folding kernel:

$$kernel(i) = \frac{\sin(\pi[i-h+\alpha])}{2\pi(i-h+\alpha)} \cdot \left[1 + \cos\left(\frac{\pi(i-h)}{h}\right) \right] \quad [3.13]$$

where α is the erroneous fraction of the sampling step and h is the radius of the sinc averaging kernel¹³. First tests for spectra from Izaña and the TCCON site in Lauder, New Zealand, show that this approach can be successfully used. First results of retrieved O₂ columns for Izaña are shown in fig 3.23.

However, some problems remain open. First the determination whether the even or the odd datapoints have to be corrected is not trivial, as this may change upon a reset of the instrument. To find the correct points by analyzing the position of the centerburst helps in many cases. However, due to phase effects this may be asymmetric, so the determination of the correct centerburst position often can not be done

¹³In the current implementation a value of 60 is used for h .

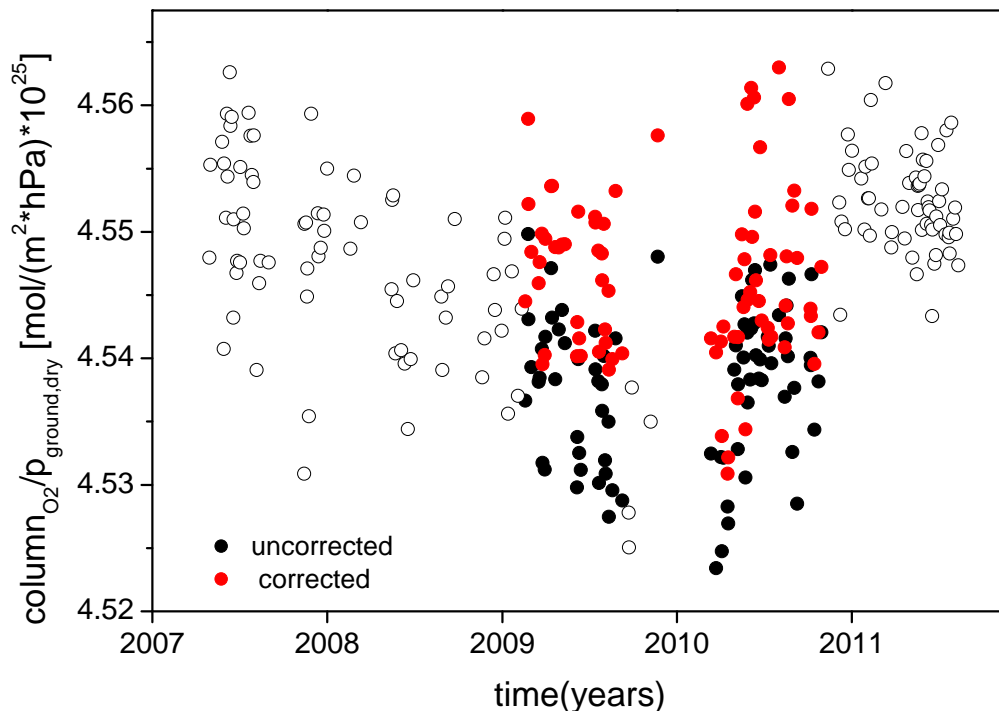


Figure 3.23: Timeseries of retrieved O_2 for Izaña with original and corrected values. The datapoints in and after 2011 are supposed to be correct, as they were recorded with the new laser sampling board. Although the corrected values are significantly improved, they still are a bit too low. As mentioned, Izaña poses severe problems for determining the size of the sampling error α . (Image courtesy of S. Dohe)

unambiguously. To make it worse, the shape of the centerburst depends on the spectral distribution of the recorded radiation (lamp, Sun). Even after a phase correction, the correct position may be exactly in between 2 sampling points, making a robust detection impossible. To avoid these problems, F. Hase recently suggested a new method for defining the ZPD position (phase-slope matching approach). A second problem, which may occur is the presence of detector nonlinearities, which, if not corrected appropriately, could disturb the above-mentioned procedure. Fortunately, the nonlinearities of the InGaAs detectors used in the NIR is negligible. A third difficulty was experienced for the spectra recorded in Izaña. Due to its altitude (2340 meters a.s.l) the spectral regions to detect the mis-sampling size are not opaque, even at high SZAs, resulting in severely erroneous values. Therefore, the best values were determined interactively for selected sample spectra as shown in Fig. 3.24.

Following a suggestion by F. Hase, a set of narrow-band filters was ordered and distributed within the TCCON in 2012, to monitor the GPR values. These filters transmit between 5500 and 6500 cm^{-1} which enables to determine the GPR values easily as the parent and the ghost signals do not overlap. The filters can be moved automatically into the spectrometer's light path, which is done in the standard measurement procedure in Karlsruhe.

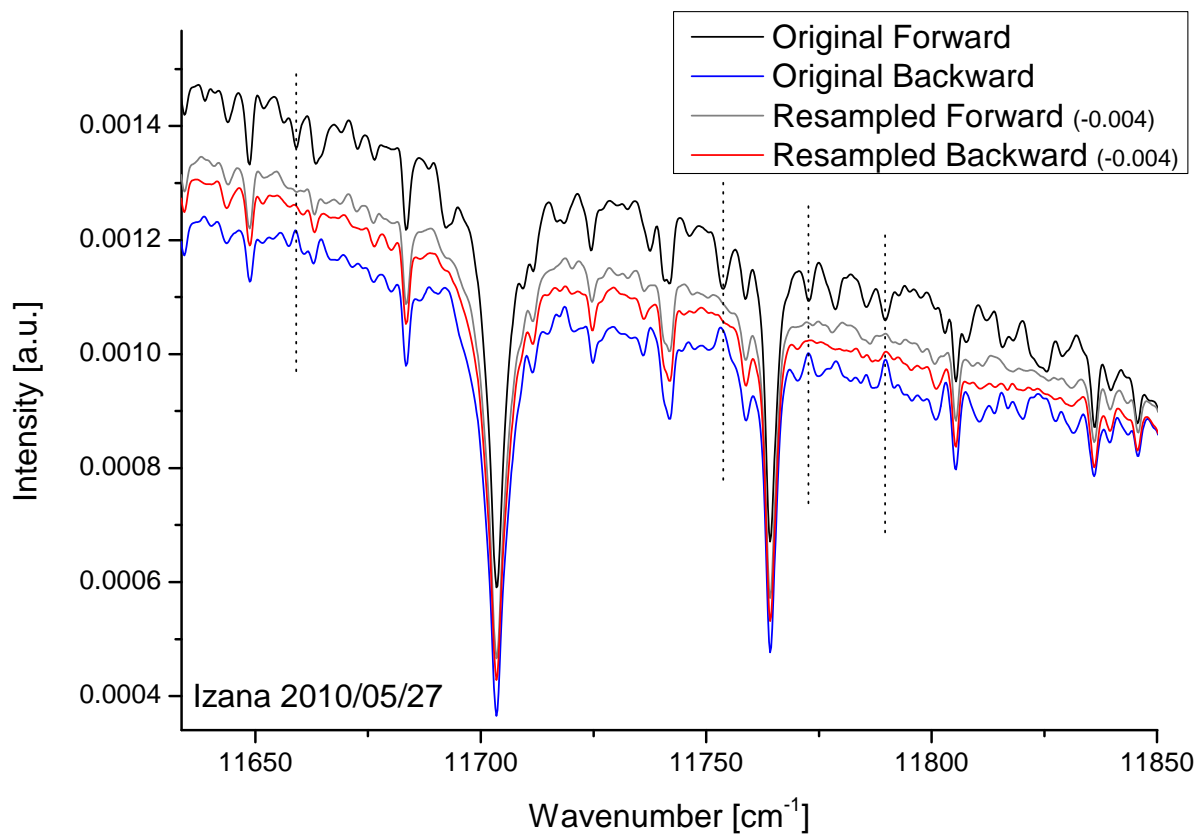


Figure 3.24: Example for manually approximating good resampling values for Izaña spectra which do not show sufficiently opaque areas. Due to special instrumental reasons, the ghosts from the forward- and the backward interferogram recording direction contribute with different signs. Therefore it is possible to identify ghost lines by nonphysical opposing lines (see marked positions in the figure). A resampling value can then be found by removing these artifacts. However, this approach is not very precise and difficult to implement in an automated code. The spectra were calculated from an average of 13 interferograms on 27th of May 2010.

3.7 Intraday temperature and pressure variability

To derive trace gases in the atmosphere, a good knowledge of the temperature and pressure profile along the light path is necessary in order to precisely retrieve gas concentrations. These p-T-profiles can be obtained by in-situ measurements (e.g. radiosonde ascends on stratospheric balloons) or meteorological models. Typically, there are no in-situ measurements close to a FTIR station available, except for the ground pressure and temperature. Therefore one has to retrieve the profiles from models such as provided by the “National Centers for Environmental Prediction” (NCEP), the “Global Modeling and Assimilation Office” (GMAO) or the “European Centre for Medium-Range Weather Forecasts” (ECMWF). NCEP data can be retrieved by using the “Goddard Automailer”¹⁴ for single days and positions (which is the standard procedure for PROFFIT) or for regions and longer time series at once via the “National Oceanic & Atmospheric Administration” (NOAA) website¹⁵, which is used by the TCCON. The NCEP data is freely available for the synoptic times 0, 6, 12 and 18 UTC on a global 2.5 x 2.5 degrees grid only few days after real time. It supplies p-T-information down to 10 mbar (corresponding to about 32 km altitude a.s.l.), so it is suited for tropospheric gases. However, for stratospheric gases, p-T data at higher altitudes are advantageous.

To get p-T-data for higher altitudes and smaller grid sizes, the “Modern-era retrospective analysis for research and applications”¹⁶ (MERRA) data from the GMAO was implemented to be used in PROFFIT. MERRA data is freely available and the p-T-information range down to the 0.1 mbar pressure level (about 64 km above sea level), 4 times a day on a 1/2 x 2/3 degrees grid or 8 times a day on a 1.25 x 1.25 degrees grid.

In the implementation of MERRA data done to create the p-T-profiles used by PROFFIT, the 8 times per day data product was used. In the following the course procedure is outlined. Especially for high latitude sites such as Kiruna, the Sun has very low elevation angles. Therefore the solar radiation passes through air masses, which are far away from the actual observer location, so that a single vertical p-T-profile is not sufficient. For that reason, a sufficiently large area around the observer’s location can be downloaded. When creating a p-T-profile for a given day, the solar direction from the observer’s position is calculated for the 8 available model data times. Using this direction, the light path is modeled upwards (refraction is neglected for simplicity) through the model grid, where the resulting values are interpolated from the 8 surrounding model data points. The temperature is interpolated linearly with height, the pressure

¹⁴The Goddard Automailer is operated by L. R. Lait, P. A. Newman and M. R. Schoeberl at the Chemistry and Dynamics Branch at NASA Goddard Space Flight Center http://acdb-ext.gsfc.nasa.gov/Data_services/automailer/. NCEP data can be retrieved for a specific date (e.g. 6th of March 2012 at 6 UTC) and location (e.g. 8.44E and 49.1N for Karlsruhe) by sending an email to science@hyperion.gsfc.nasa.gov with the subject “metprofile 2012-03-06T06 8.44 49.1 10 1000 ANY” and the result is sent back to the sender. The minimum pressure level is 10 mbar however. Lower pressures down to 1mb can be obtained by “metprofile 2012-03-06T12 8.44 49.1”, which returns meteorological data from the objective analyses at the Climate Prediction Center (CPC) at NCEP. However, this data is available for 12 UTC only.

¹⁵<http://www.esrl.noaa.gov/psd/data/gridded/data.ncep.reanalysis.html>

¹⁶<https://gmao.gsfc.nasa.gov/merra/>

in an exponential way, using the barometric equation, the temperature and humidity profile. For the necessary non-trivial transformation from the Cartesian to the Geographic coordinate system the method by Bowring (1976) was used, as explained in Gerdan and Deakin (1999). As the MERRA model data is given in pressure levels, the ground pressure is not available, especially if the observing station is located below the 4 surrounding model grid points due to the apparent orography. For this case, a constant lapse rate, or a file containing data of on-site temperatures and pressures can be given as an input.

For the altitudes above the available data, climatological information is used, such as given by the WACCM¹⁷ model.

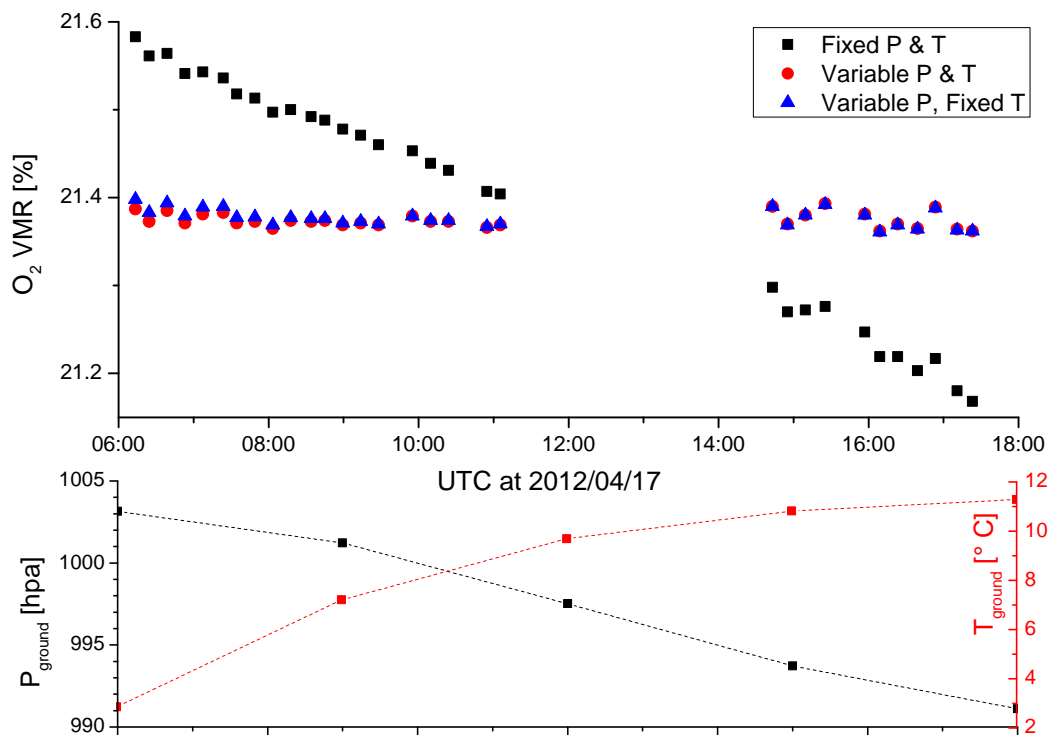


Figure 3.25: Influences of intraday temperature and pressure changes for TCCON measurements taken in Karlsruhe. The O_2 volume mixing ratio was retrieved due to its low variation in the atmosphere. The lower graph shows the intraday ground temperatures and pressures used for the retrieval, as derived by the MERRA data and the meteorological measurement tower of the IMK at the KIT in Karlsruhe. The p-T-data is available for PROFFIT every 3 hours, as this is the minimal time step provided by the MERRA data. The intermediate values are interpolated linearly by PROFFIT as indicated by the dotted lines. The O_2 values for the 3 retrieval types change in the course of the day by -2%, -0.1% and -0.17%, in the order given in the legend. The data gap results from a temporary failure of the FTIR instrument. The complete vertical temperature profiles are shown in Fig. 3.26.

An example of the influences of varying temperatures and pressures is shown in Fig. 3.25 for a sample day recorded with the TCCON instrument at the Karlsruhe site. The influence of the temperature seems

¹⁷http://www.cesm.ucar.edu/working_groups/WACCM/

rather low (≈ 0.0064 per $^{\circ}\text{C}$ ground temperature change). However, a realistic ground temperature increases during summer days of about 15 K causes an increase of 0.1% in the O_2 VMR. The influence of the ground pressure is significantly higher (0.16% per hPa). For the sample day, the decrease of 11.1 hPa (-1.1%) results in an O_2 VMR change by an absolute value of -0.38%. In total, including pressure and temperature information for several times per day into the retrieval, increases the accuracy significantly: the change in O_2 VMR drops from 2% to 0.1%.

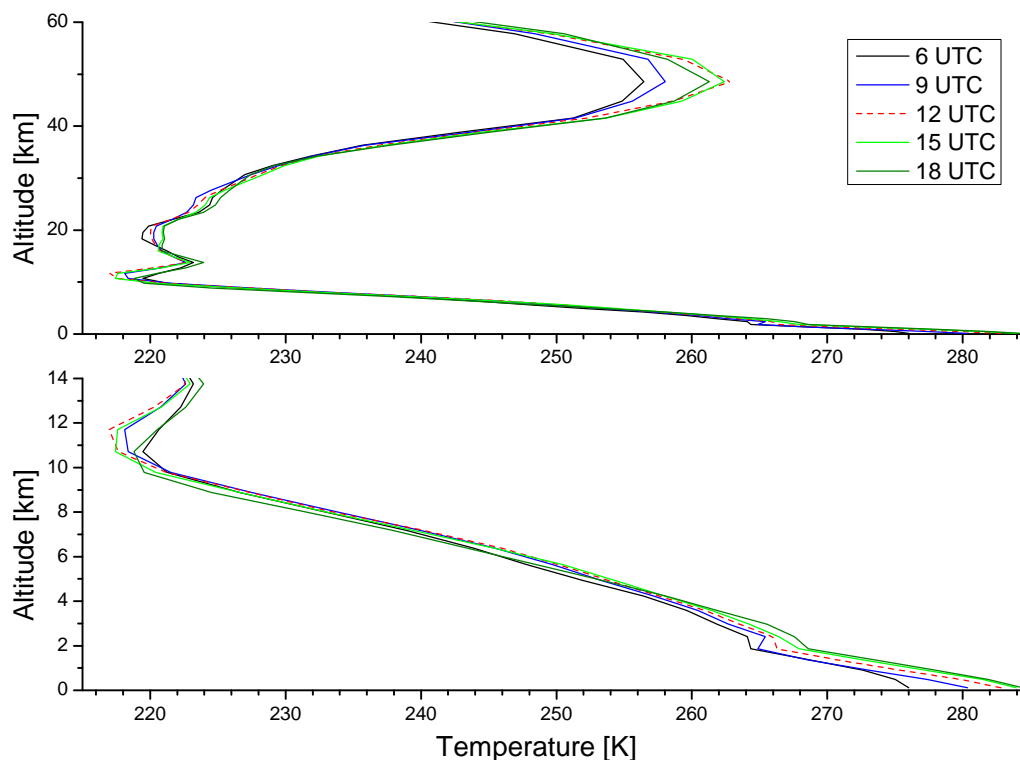


Figure 3.26: Vertical temperature profile used for Karlsruhe at 17th of April 2012. In the troposphere, the intraday temperature variations become very small above about 3 km, which is the reason for the low influence on O_2 . Due to the high variability at 50 km, the influence on stratospheric gases may be different.

To minimize the effect of erroneous atmospheric p-T-information, in the NIR the ratioing with the well known O_2 column can be used (denoted as XCO_2 or XCH_4) as many errors can be reduced by this approach (see eqn. 3.3 on page 26). However, its quality depends on how similar the O_2 and the unknown retrieved trace gas concentrations are affected by erroneous input values. In case of the XCO_2 and the sample day used in Fig. 3.25, the O_2 ratioing overcompensates the effect for the retrieved XCO_2 , as can be seen in Fig. 3.27. The O_2 retrieval seems to be more affected by the pressure than the CO_2 retrieval. Therefore a pressure change of 11 hPa induces an error of about 0.32% in the XCO_2 . To conclude, the usage of variable pressure values in the retrieval is essential to achieve high accuracies. The ratioing with the O_2 column is not suited for compensating erroneous pressure values.

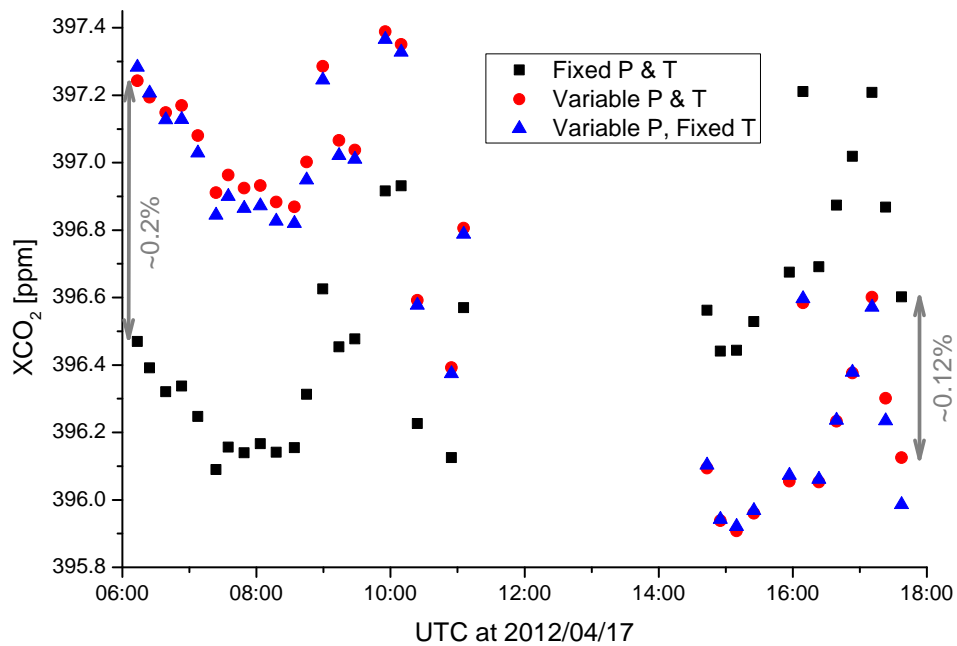


Figure 3.27: Influence of variable pressures and temperatures on retrieved XCO₂. The red circles indicate the use of variable temperature and pressure informations. As these lead to very precise O₂ VMR values as shown in fig. 3.25, the red circles can be assumed to be very close to the true XCO₂ values. When neglecting the variability of the temperature and pressure (black squares), the course of the XCO₂ values within the day is significantly disturbed.

3.8 Conclusions of investigating error sources

The impacts of several errors and inaccuracies in the course of recording and evaluating spectra were investigated in this chapter. For cases in which indicated adverse effects onto the desired trace gas retrieval accuracy in excess of 0.1 % were found to be possible, correction measures were presented.

A program providing high precise astronomical solar positions for a given time and observer's location on Earth was developed. The accuracies for the elevation- and azimuth angles were found to be -0.02 ± 0.25 (1σ) and -0.3 ± 0.3 arc seconds. In addition, the effect of refraction was investigated, especially in context of a pressure, temperature and wavelength dependence of the refractive index. The pressure and temperature profiles of the atmosphere have a significant impact onto the calculation of the total air mass, and therefore onto the trace gas retrieval. The wavelength dependence, however, showed minor effect only.

The duration of a single measurements should not exceed a certain time, as the moving Sun, and therefore the variable air mass, impacts the retrieval results. To keep the error below 0.5 % for SZA smaller than 80° , the duration should not exceed 3 minutes for equatorial sites and 6 minutes for mid-latitude sites.

The variation of the solar intensity during a single measurement showed significant adverse effects onto the trace gas retrieval. Therefore a highly efficient correction scheme was presented. For a sample day with thin cirrus clouds, the scattering (1σ standard deviation) of the trace gas results was reduced by a factor of 10.

Sampling inaccuracies in the recording of interferograms induce distortions in the spectra and lead to significant errors in the retrieval results. As many instruments worldwide recorded mis-sampled interferograms for many years, a correction scheme was developed and presented in this chapter.

The usage of variable temperature and pressure profiles in the course of a measurement day, instead of a single profile, turned out to be essential. For this reason a program was created, which extracts the required values from meteorological model data. For a sample day, an erroneous intraday descend of 2 % of the O_2 column values could be reduced below 0.1 %. In addition, it was found that the O_2 ratioing is not capable of compensating erroneous pressure values to a sufficient degree.

4 Camera-based optical tracker feedback

A main part of this work was dedicated to improve the tracking accuracy of solar tracker systems, as slight inaccuracies of the resulting line-of-sight (LOS) may contribute strongly to the retrieval results (see sec. 3.2 on page 27). In this chapter a new optical feedback mechanism will be presented, which will be denoted as “CamTracker” in the following. The setup was published in Gisi et al. (2011). Some parts of this chapter were adopted from this publication.

A key point was to abandon the commonly used quadrant diode. Instead the information supplied by a camera to monitor and correct the spectrometer’s LOS is used. The respective optical setups are presented in sections 4.1 and 4.2.

The operation principles of the newly developed software, including the image processing and the setup procedures for a camera-based tracker control are given in section 4.3.

An overview of principal advantages of a camera-based setup follows in section 4.4.

Accuracies reached with the new system at the three sites, at which the new system was installed until 2012, are given in section 4.5, together with an error approximation. In section 4.7 the user interface to control the tracking system is described briefly.

4.1 Previous quadrant based optical feedback

The current approach to obtain a good tracking precision is the application of a quadrant diode, which registers deviations from the ideal pointing direction of the tracking system. For this, a part of the radiation has to be lead onto a quadrant diode in front of the spectrometer’s input field stop. The diode signal is then fed in the control loop of the tracker (Adrian et al., 1994; Notholt et al., 1995; Washenfelder et al., 2006). However, these systems do not achieve the required accuracy (see section 3.2) in some conditions, e.g. at low solar elevation angles. A main reason is the vulnerability to misalignments. As the system centers the solar image intensity on the center of the quadrant diode, a slight displacement of the diode causes a deviation of the true relevant LOS, which is defined by the spectrometer’s field stop position. For the commonly used IFS125HR spectrometers, a shift of the quadrant diode of as little as 0.1 mm results in a systematic LOS offset of about 51 arc seconds, which in general, can’t be corrected afterwards.

In addition, quadrant diode systems also require strict conditions on the shape and intensity distribution of the light source, as the quadrant diode centers the center of intensity of the radiation.

A main part of the efforts done in context of this work was to overcome these problems by controlling the tracking with a new camera-based system.

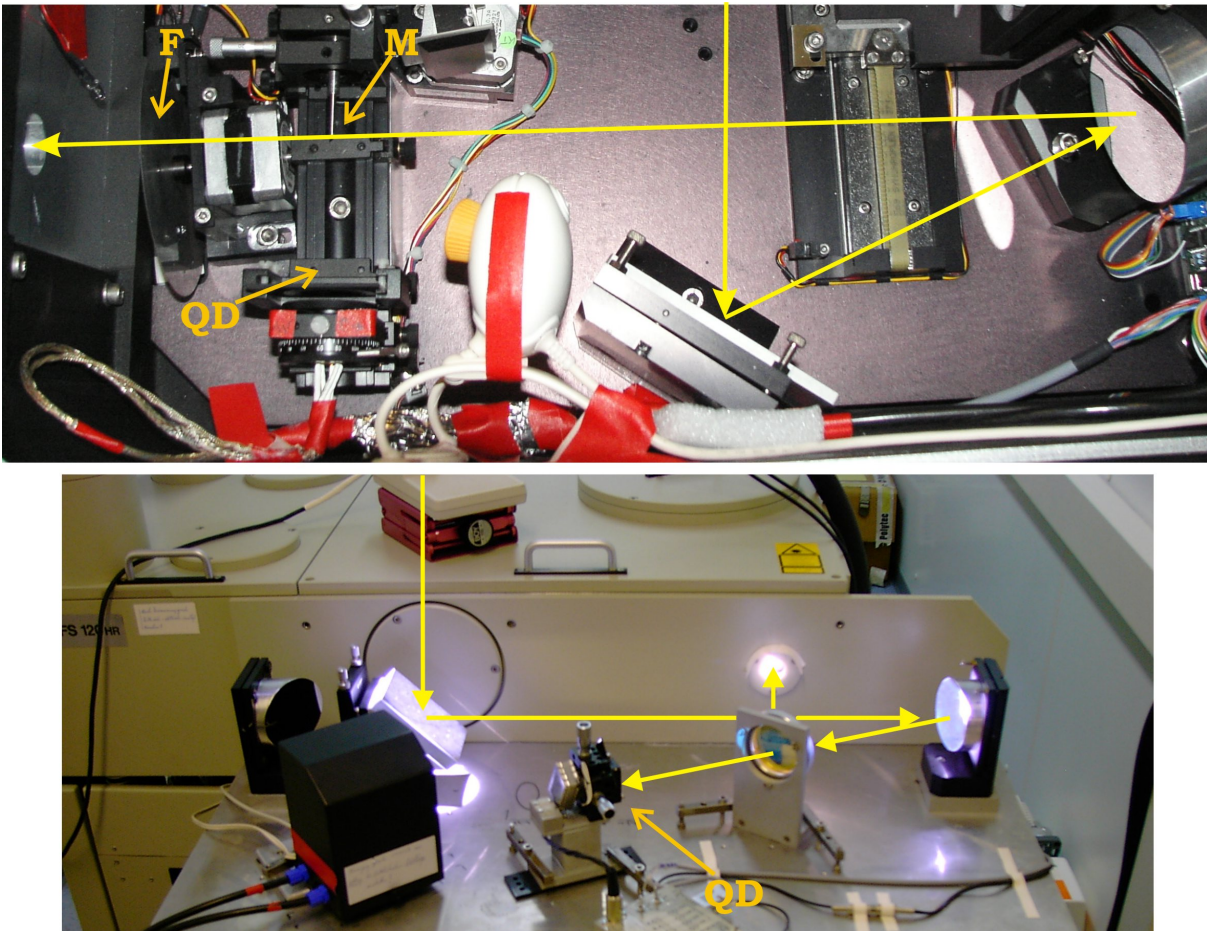


Figure 4.1: Optical quadrant diode setups of the pre-optics in Kiruna (top) and Izaña (bottom). In Kiruna, a part of the beam is deflected by a small mirror (M) in front of the field stop (F) onto the quadrant diode (QD). This setup is common for FTIR spectrometers. In Izaña, the diode is placed behind a semitransparent mirror.

In figure 4.1 the quadrant diode setups of Kiruna and Izaña are presented.

The upper image in Fig. 4.1 shows the setup of Kiruna until September 2010, before it was replaced with a camera-based system. An additional small mirror at the end of a thin metal bar in front of the field stop reflects a part of the radiation out of the main light path onto the quadrant diode. Deviations in this mirror orientation directly affect the tracking.

The lower image shows the setup as it was operational in Izaña until April 2012. A plane semitransparent mirror is inserted between the spectrometer's focusing parabolic mirror and the entrance aperture, which covers the full beam diameter and reflects the IR radiation towards the spectrometer while a fraction of the VIS radiation is transmitted towards the quadrant sensor on which an image of the Sun is created. This is beneficial, as no additional misalignment is introduced by any additional optical element in the light

path. As the same beam is used by the quadrant sensor as by the spectrometer, this setup is insensitive against optical aberrations of the off-axis paraboloid such as astigmatism and has not been realized at other FTIR sites so far. As a consequence, the tracking accuracy in Izaña is exceptionally good, as will be shown in Fig. 4.15.

The Kiruna setup may be representative for most FTIR solar trackers in operation, whereas the Izaña setup is presumably the optimum which can be achieved with the quadrant diode approach.

4.2 Camera setup

To achieve an improved tracking accuracy, a camera-based system was set up and used. For this process, it was applied first at the measurement site in Karlsruhe in 2010. As the tests showed an excellent tracking accuracy, the same system was installed in Kiruna (2010) and Izaña (2012). In the following, the setup in Karlsruhe will be described. General details about the measurement stations were given in section 2.3 on page 22.

The tracker in Karlsruhe is mounted on top of the container and has, except for the motor-types, the same technical setup as the trackers in Izaña and Kiruna. The mechanical setup of this alt-azimuthal tracker type is shown in Fig. 4.2, further informations about the various tracker setups used and built within this work are given in section 5.1.

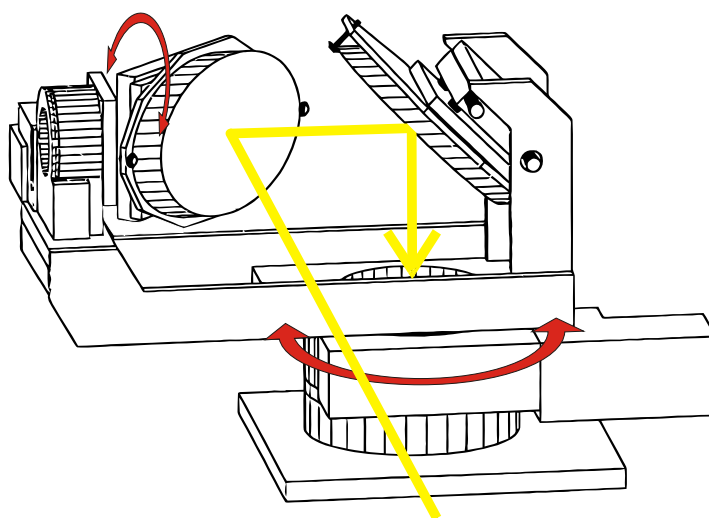


Figure 4.2: Schematic setup of the tracker in Karlsruhe, Izaña and Kiruna (adapted from Huster (1998))

The setup of the camera-based system inside the container is shown in Fig. 4.3. The optical path from the second tracking mirror to the input window of the spectrometer spans about 2.5 m. An off-axis parabolic mirror with an effective focal length of 418 mm focuses the radiation onto the input field stop of the spectrometer. This field stop is an important component of a high-resolution FTIR spectrometer as it defines the interferometer's field of view. It is realized by a thin steel disk with round holes of different diameters along the perimeter, which can be rotated to select a desired field stop diameter. It

is slightly tilted ($\approx 10^\circ$) with respect to the passing light, to prevent reflections inside the spectrometer. The input field stop diameters used are smaller than the size of the solar disk image on the field stop wheel (3.8 mm), as the field stop should be illuminated completely and homogeneously in order to have a well-defined ILS. After passing the field stop, the light is parallelized by a collimator and then enters the interferometer after which it finally is focused onto the detectors.

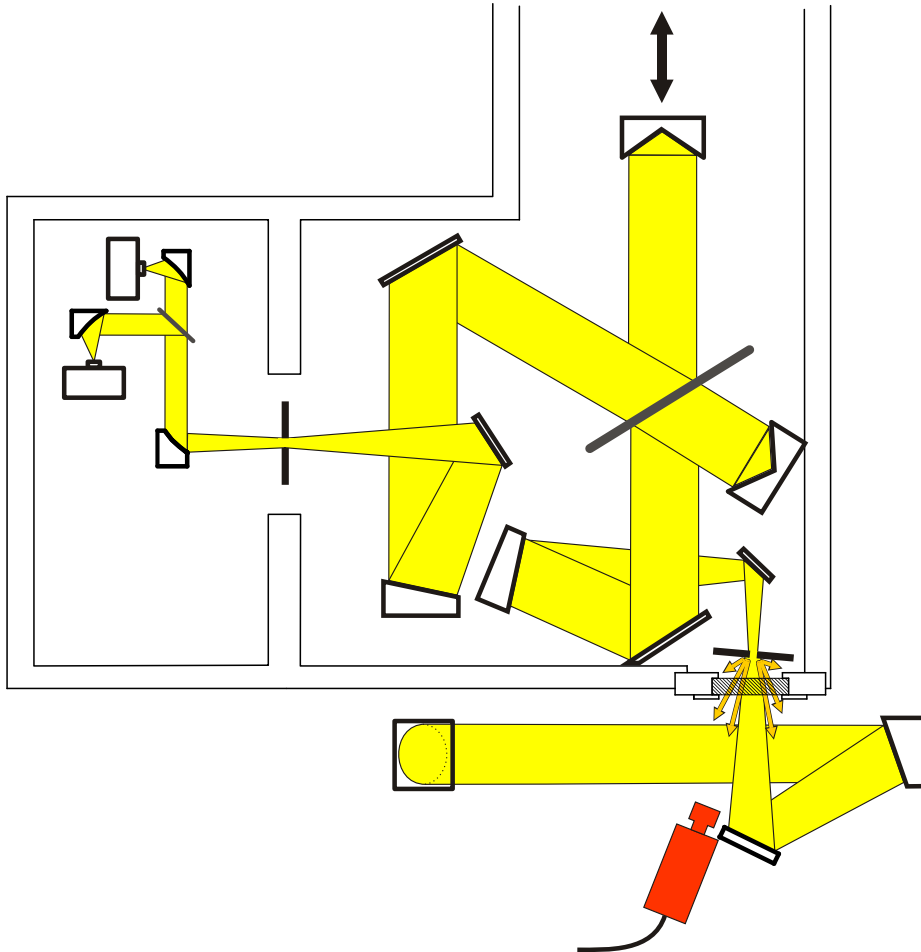


Figure 4.3: Schematic drawing of the top view of the camera set up and the light path in front of and inside the spectrometer at the Karlsruhe site. The light falls from the tracker on the roof, perpendicular to the plane of the drawing onto the first mirror. The arrows indicate radiation scattered off by the aperture wheel, part of which is observed by the camera. (Image from Gisi et al. (2011))

To monitor and control the pointing of the tracker, a standard CMOS USB camera (VRmagic VRM C-9+PRO BW with 1280×1024 pixels) was used as optical feedback, which records the radiation scattered back diffusely from the illuminated side of the field stop wheel (see Fig. 4.8). A CMOS sensor was chosen instead of a CCD sensor to prevent smearing effects. These artifacts occur at standard CCD sensors without a mechanical shutter and are dominant when recording strong light sources, which is the case when recording the solar image. The camera's distance from the field stop wheel is about 24 cm. It is positioned as close to the incoming beam as possible to minimize perspective distortions,

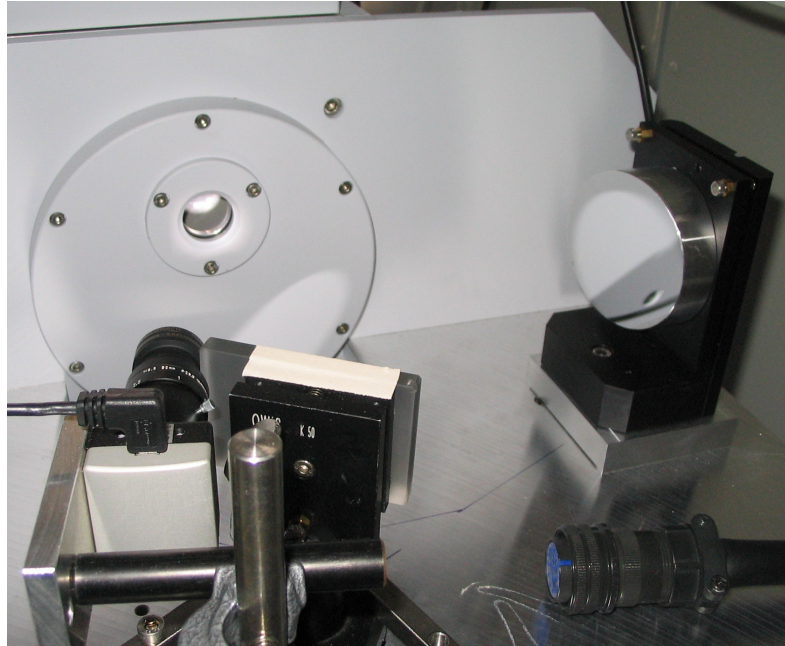


Figure 4.4: Image of the camera system in Karlsruhe, recording the solar image on the field stop, which is located inside the spectrometer's housing behind the entrance window.

without disturbing the wanted signal used by the spectrometer. The camera is equipped with a standard objective lens and appropriate optical filters to adjust for the illumination level. Due to the wavelength-dependent refractivity of air, in the case of NIR and MIR spectroscopic observations it is advantageous to equip the camera with an infrared longpass filter which transmits radiation beyond 750 nm. In connection with the spectral sensitivity of current CCD and CMOS cameras this choice defines a bandpass of about 100 nm width. Further details on atmospheric dispersion is given in sec. 3.3.5 and 3.3.6. With this setup, the solar disk has a diameter of about 240 pixels, the field stop diameters cover a range from about 30 to 160 pixels. This results in an angular size of about 8 arc seconds per pixel. The pictures containing the information about the positions of the solar image and the field stop are evaluated on a standard PC in real-time. A software was developed for this purpose (see section 4.7) which uses appropriate image processing algorithms to determine the actual tracking position accuracy. In case of deviations from the ideal pointing direction, necessary corrections to the astronomical tracking mirror angles are calculated. The program then sends the tracking commands to the motor controller (Newport XPSTM) via an IP connection.

4.3 Principle of operation

The operation principle of the camera based tracker is a combination of astronomical algorithms (see sec. 3.3) to provide the coarse mirror angles, with a superposition of small corrections to these angles derived from the optical feedback provided by the camera. The recorded pictures are evaluated by the specifically

developed CamTracker software (see sec. 4.3.1) in real-time, in order to determine both the central position of the field stop opening and the solar disk. Then the necessary mirror angle corrections to “move” the solar disk on the field stop wheel to the desired position relative to the input field stop opening are calculated (see sec. 4.3.2). This is done about 4 to 8 times per second. For about 5 seconds these mirror angle corrections are accumulated, checked for consistency, combined and send to the tracking system, after being superimposed to the result from the astronomical calculations. In the intermediate time the mirrors move with a constant speed, to avoid stepwise operations which could lead to vibrations of the mirrors. This procedure with the long accumulation period was chosen as it is less prone to distortions, e.g. from clouds. It makes use of the slow varying solar position. For applications on moving platforms such as ships, the accumulation time has to be adapted. The way the necessary mirror corrections are accumulated and used is presented in Fig. 4.5. A simple averaging of the accumulated correction values is not correct, as in general these change systematically.

If no usable positions for the solar disk and the field stop opening can be determined, for example due to clouds, the system continues tracking on the basis of the astronomical coordinates together with previously saved offset values for similar tracking angles. Offsets in the course of one example day retrieved from the camera optical feedback are presented in Fig. 4.6.

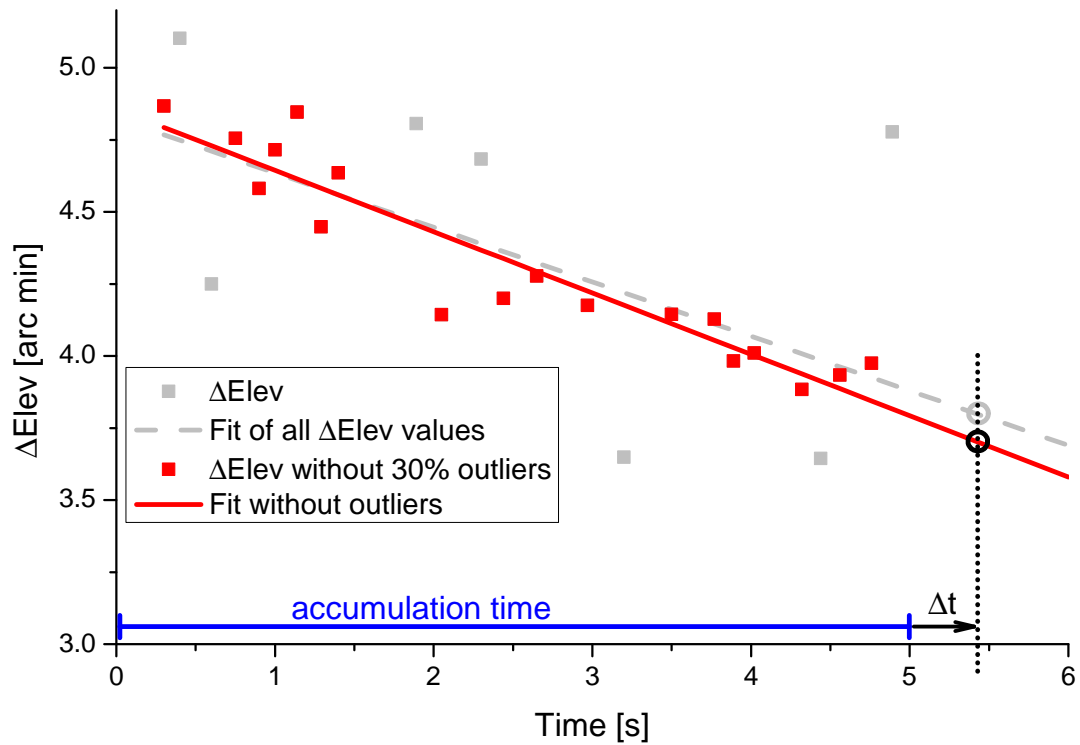


Figure 4.5: Procedure of accumulating necessary correction angles over a longer time period. In this schematic overview, the corrections for the elevation mirror (ΔElev) are accumulated for 5 seconds (gray and red squares), where the time information is saved as well. A linear fit (gray dashed line) to these values could be used to retrieve the actual correction needed (gray circle), a variable time step Δt after completing the accumulation. The usage of a Δt is beneficial, to compensate for the time passing, from the recording time of the last evaluated image (more precise the middle of this time) to the time when the correction signals are sent to the motors. The influence of outliers in the diagram, which may be induced from clouds, are minimized by ignoring a variable number of values (here 30%) which have the greatest distance from the fit. The remaining values (red squares) are then used for a better fit (red line) and a better correction value (red circle).

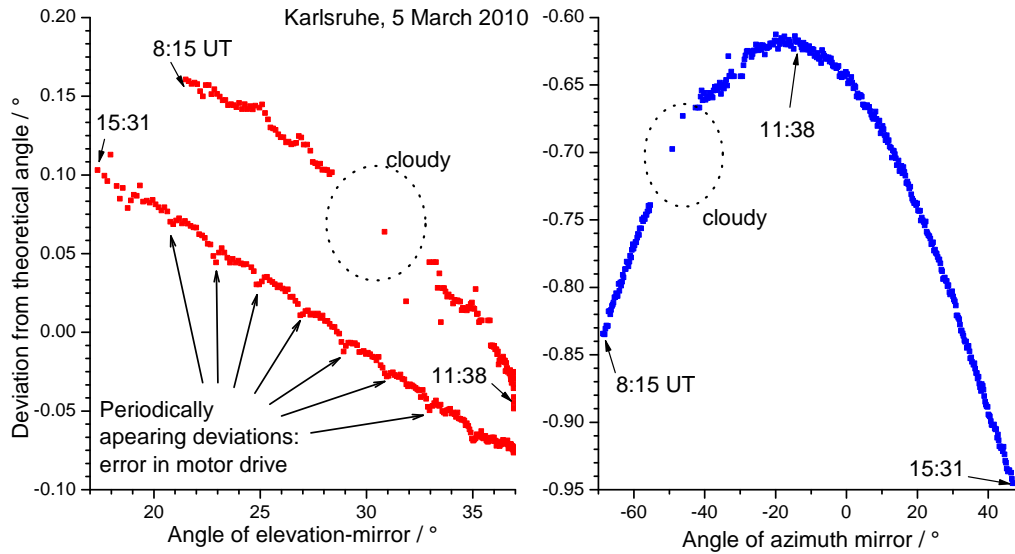


Figure 4.6: Required offsets to center the solar image on the field stop for both motor angles in the course of one measurement day, as derived from the camera-based optical feedback. In the left graph every 2 degrees an additional offset was necessary, which could be identified to stem from a damaged gear in the rotation stage.

4.3.1 Image processing

The main steps in determining the central positions of the solar image and the field stop from the camera pictures are the following:

1. Finding an appropriate threshold value to separate the bright area illuminated by the Sun from the dark, non-illuminated rest of the field stop wheel, and the dark opening of the field stop. This is done by analyzing the brightness histogram of the image (see Fig. 4.21), in which the two areas can be identified quite easily under normal conditions.
2. Creating a binary (black/white) picture by applying the threshold.
3. Modifying the image with morphological operators (open¹ and close²) to suppress small structures at the rim of the solar disc region.
4. Finding the contours along the obtained areas (solar disk and field stop).
5. Fitting 2 ellipses along the contours (in a least squares sense), and a circle along the bigger contour. The use of an ellipse is necessary, as the image of the Sun is not completely circular. This results from a non-perpendicular projection direction of the solar radiation on the field stop wheel, an angled observing direction of the camera and astigmatism effects due to non-ideally aligned off-axis parabolic mirrors. In the cases of a partly cloud-covered Sun or an incompletely illuminated

¹[http://en.wikipedia.org/wiki/Opening_\(morphology\)](http://en.wikipedia.org/wiki/Opening_(morphology))

²[http://en.wikipedia.org/wiki/Closing_\(morphology\)](http://en.wikipedia.org/wiki/Closing_(morphology))

Moon (see Fig. 4.11), the fit of a circle is more robust and is therefore better suited to approximate the center of the Sun or the Moon. To make the circle fit less prone to clouds passing in front of the Sun, the used cost function is dependent on the direction of the contour relative to the circle. Regions of the contour extending into the solar disk region have a significantly lower effect than convex parts of the contour.

6. Performing consistency checks, whether the obtained ellipses and the circle can be the contours of the solar disk and the field stop opening in terms of criteria like radius, position and eccentricity.
7. If the previous step was successful, the central positions of the ellipses are used as centers of the solar disk and the round field stop opening, and it's relative offset is used to correct the tracker's line-of-sight. If the big ellipse did not pass the quality check, whereas the circle did, this central position is used as the solar center.

In figure 4.7 the intermediate results after each image processing step are displayed. Figure 4.8 shows the solar image superimposed with the retrieved ellipses.

The described image processing procedure showed to be the most robust way to determine the rims of the Sun and the field stop. Other possibilities such as gradient based algorithms were tested. However, the high spatial scattering variability of the field stop material strongly disturbed the gradient detection algorithms.

After the first start of the image processing, the threshold in the histogram is determined by searching a minimum value between the maxima related to the dark and illuminated pixels. The number of "Sun-pixels" which are brighter than this threshold is saved. A typical value for Karlsruhe is 45000. For the subsequent images the threshold is set to a brightness value which gives the same number of "Sun-pixels". This way of determining the threshold is advantageous, as it neglects the influence of varying total intensities and reduces the influence of clouds significantly. However, care must be taken in case of changing aperture stop diameters, which changes the illuminated area and therefore the number of "Sun-pixels".

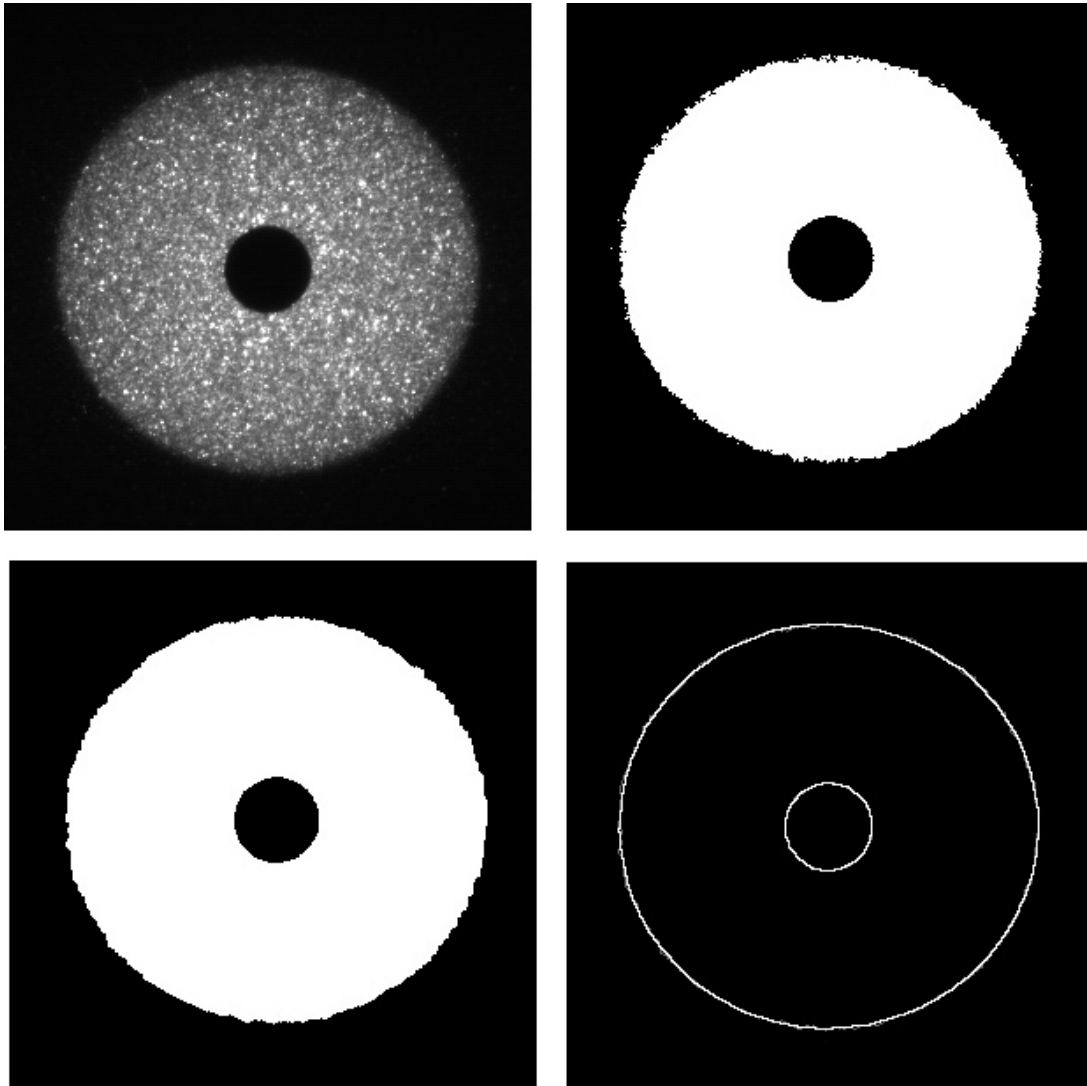


Figure 4.7: Original solar image as recorded by the camera in Karlsruhe (top left), after applying a threshold (top right), after applying morphological operations (bottom left). The bottom right image shows the retrieved contours (grey) and the fitted ellipse (white). The metal field stop disk is sandblasted, which causes the inhomogeneous illumination.

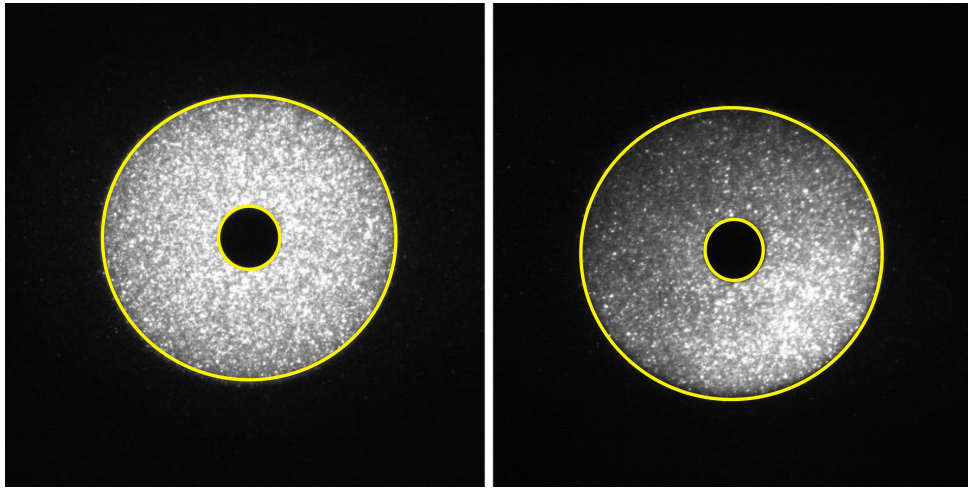


Figure 4.8: Two pictures of the camera recorded in Karlsruhe. The ellipses, which have been retrieved by the image processing algorithms are painted in yellow on top of the original image. The solar disk and the field stop opening have diameters of 244 and 52 pixels respectively. The field stop diameter used was 0.8 mm. The right picture shows a correct positioning of the solar disk relative to the field stop opening despite strong intensity variations resulting from clouds, which would be impossible using a quadrant diode.

4.3.2 Automatic calibration of the optical setup

In order to calculate the corrections to the tracker mirror angles, it has to be known how the tracker axes have to rotate, to realign the solar disk on the field stop. This relationship (which will be denoted as mirror-image-correlation (MIC) in the following) is not constant, but depends on the solar position in the sky and the orientation and geometric design of the tracker. One way to obtain the MIC is to model the whole mirror system including the camera and its focusing optics, which is a quite complex task (Huster (1998)). A simple experimental approach is to sequentially move the mirror angles a few small defined steps, and to register the resulting shift (direction and distance) of the solar disk in terms of camera pixels on the field stop. This procedure, however, can only be performed between FTIR measurements, which is not frequent enough in some cases. In addition it takes some time to be performed, which then is missing for the FTIR measurements. Therefore, a combination of the two procedures is used. This includes a simulation of the moving mirrors of the solar tracker only (which are either one or two as described in sections 5.1.1 and 5.1.2) which therefore is rather simple, and the experimentally determined MIC, which is performed only once after the first setup of the system and is repeated if something has changed in the optical or mechanical setup. Using this, the simulation is initialized, so that it can calculate the MIC for any desired solar position. This has the advantage that the solar position independent effects of all the optical elements after the first two tracking mirrors are determined experimentally. Therefore, the only thing to do after a change of the position or the orientation of the camera or a change in any mirrors is to reperform the initialization sequence to adapt the simulation.

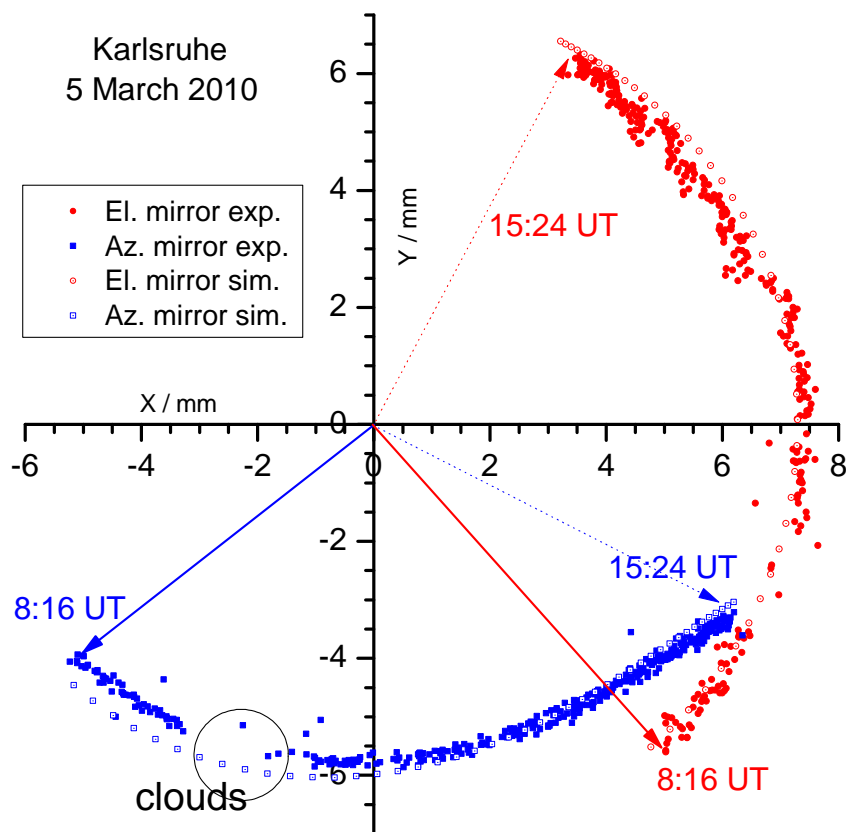


Figure 4.9: Experimental and simulated effects of rotating a single tracking axis by 1 degree in an Alt-Azimuthal setup onto the position of the solar image on the aperture (MIC). At the beginning of this day the simulation was initialized, allowing to calculate the MIC for the rest of the day within less than 2 degrees. The experimental MIC values (filled circles and squares) were obtained automatically every minute.

Examples for the effect of rotating a single axis of an alt-azimuthal tracker onto the solar image position on the entrance aperture are shown in figures 4.9 for Karlsruhe and 4.10 for Izaña. At low elevation angles, the daily course follows a simple circle-like path. At higher elevation angles, which can occur at low latitude sites, the pattern becomes quite complex. This is due to the fact, that for the direction into the zenith, the azimuthal-direction is undetermined. Nevertheless, except for the zenith, the directions in which the solar image moves for a rotation of the elevation- and the azimuth angle, always enclose an angle of 90 degrees.

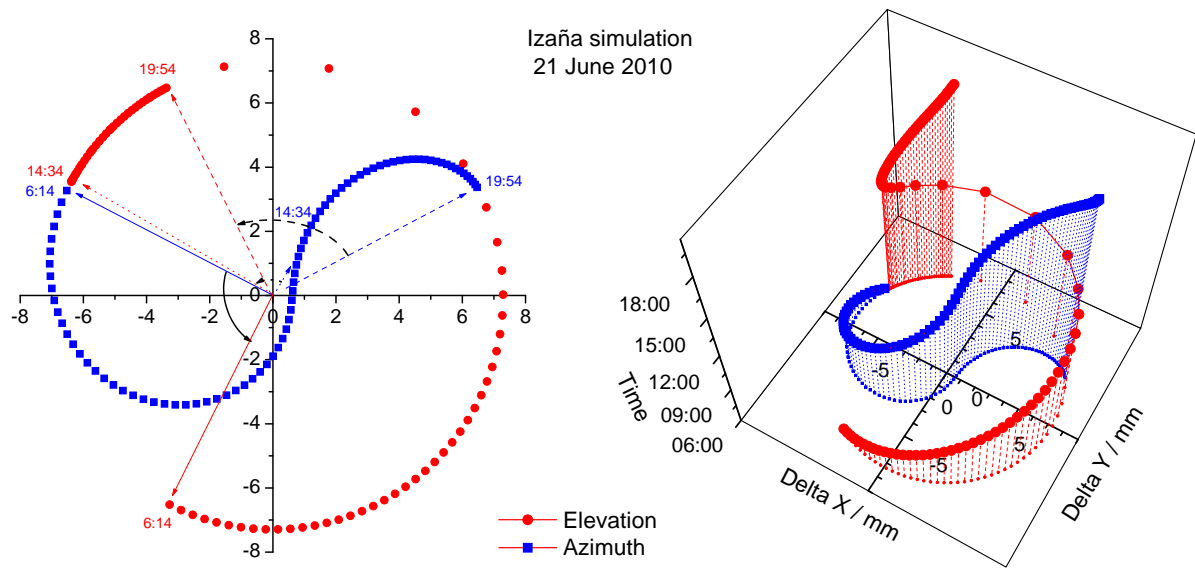


Figure 4.10: Simulation of the MIC for Izaña. As in figure 4.9 the mirrors are moved by 1 degree to cause the displayed shift of the solar image on the field stop.

4.4 Advantages of the camera setup

The main reasons to choose the camera set up instead of a quadrant diode, which is the current solution applied in the NDACC and the TCCON, is that it results in a very exact tracking (see sec. 4.5), it is easy to setup and very robust:

- Using the camera information, it is possible to determine both the position of the center of the solar disk on the field stop wheel and the opening of the stop at the same time. Since the input stop itself defines the measurement direction of the spectrometer, direct information about the pointing and its errors can be obtained. In other words, the camera-based optical feedback system is self-calibrating. Systematic shifts which can easily occur with a quadrant diode setup are avoided. Even deficits in the mechanical positioning of the field stop (see sec. 4.6.1) are canceled, as its position is determined continuously. Displacements of the camera into any direction do not matter as long as the camera records a sufficiently focused picture of the solar disk and the field stop opening. This, as the only prerequisite, makes the system very easy to set up and robust. Combined with an

excellent spatial resolution of current cameras, this leads to a very precise tracking of the Sun, as will be shown in section 4.5.

- A very important advantage over a quadrant diode setup is the ability of precisely tracking light sources which have a variable intensity over their surface. For the Sun, this can be caused by a rather thin cloud layer or mist which dims a part of the Sun, as it often happens at low solar angles. As long as a big part of the rim of the solar disk can be determined, it is possible to retrieve the center and to maintain the precise line-of-sight (LOS) steering. An example can be seen in figure 4.8. In contrast, a quadrant diode detects the center of intensity instead, which then is centered onto the input field stop.
- In case of an incorrect LOS, the necessary absolute tracker angle correction values can be calculated from a single image. A quadrant diode setup, however, only provides intensity differences between the quadrants, from which the necessary correction can't be calculated with the same precision. Therefore, the camera-based setup is capable of performing the corrections precisely and therefore very fast.
- Resulting from the fact that the rim of the light source can be used instead of the center of intensity, the system provides the ability to track non-spherical light sources, such as the partially illuminated Moon, as shown in the left part of Fig. 4.11.
- By storing the pictures, even in the occurrence of tracking problems, one can determine the actual pointing directions later on and use them when evaluating the FTIR spectra. The stored pictures also offer a way to reveal the causes of unexpected intensity variations during subsequent inspections of the interferograms (e.g. moving objects such as clouds and airplanes or transit of the Sun across fixed obstacles, e.g. contours of antennas, buildings and trees), as shown in the right part of Fig. 4.11.
- The camera based system is very easy to set up since no other optical elements except for the camera are needed. Its only prerequisite is the existence of a field stop which scatters some radiation back, so it is widely applicable.

4.5 Accuracies of tracking

The quantification of a tracking system's accuracy is a difficult task. One possibility could be to check the variation of the retrieved O_2 column. However, this requires the knowledge of the precise pressure- and temperature profile and a good knowledge of the spectroscopic data of O_2 and all interfering gases. In practice (especially at low SZAs), the available accuracy is too low for the detection of the errors induced from the very precise camera-controlled tracker. In addition, at pure NDACC stations such as Kiruna, the NIR spectral range is not recorded so that no O_2 column can be retrieved. Here, in principle, the N_2 column could be used. However, these lines are very weak. In addition, the precision of spectroscopic parameters is not sufficient, which prevents the application of this procedure until today.

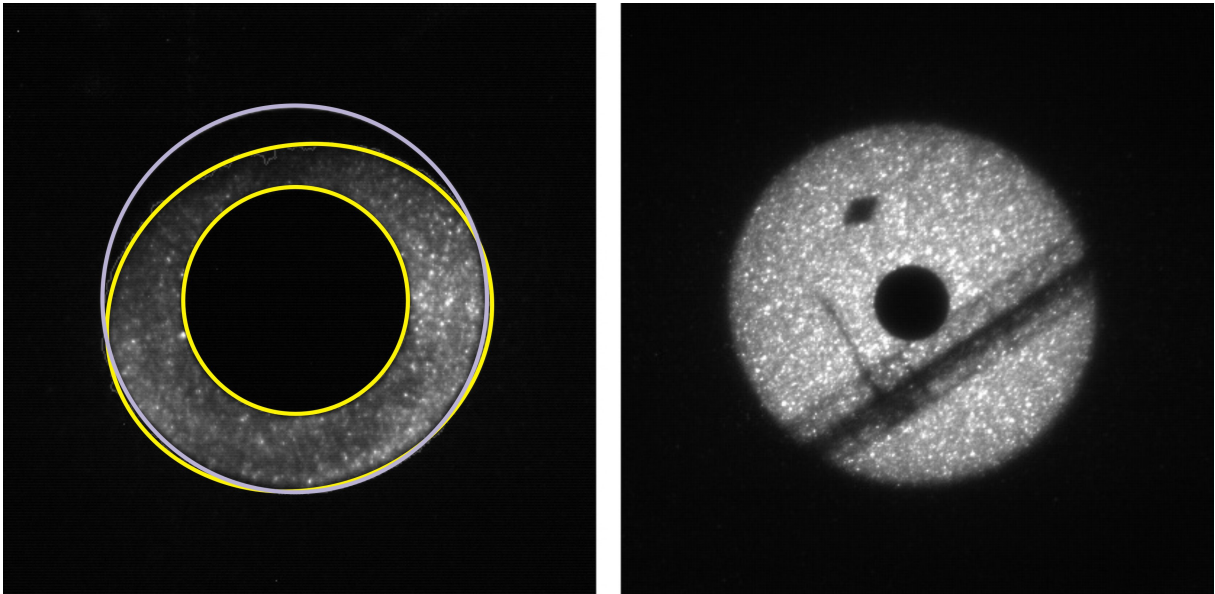


Figure 4.11: Left: Image of the non-fully illuminated Moon. Here the center of the fitted circle (blue) gives a better approximation for the center of the Moon than the ellipse (yellow). To observe and track the Moon, the optical band pass filter in front of the camera lens was removed. Right: Obstacles can be identified, such as the 200 m meteorological measurement tower which is located close to the TCCON spectrometer in Karlsruhe.

Two possible methods to determine the tracking accuracy are described in sections 4.5.1 and 4.5.2. Here, the ellipse data from the tracking, and a shift of the solar lines with respect to the terrestrial lines in the measured spectra are used.

4.5.1 Ellipse center positions

A first approach to determine the tracking accuracy of the “CamTracker” system is to look at the distance between the centers of the two ellipses, which correspond to the solar disk and the field stop opening. This may not exactly be the actual accuracy of the pointing, since there may be deviations between the ellipse and the actual rim of the solar disk and residual errors resulting from small perspective distortions. Still a useful quantification of the pointing error due to the motor resolution and mechanical backlash can be expected. As the recorded solar disk diameter in camera pixels and its angular size on the sky of about 32 arc minutes is known, one can transform the ellipse center distances in pixels to tracking angle deviations in degrees. Figure 4.12 shows a plot of these deviations over a time period of more than 8 h, from which a tracking precision of 3.7 arc sec and a very small systematic error of about 0.3 arc sec can be derived.

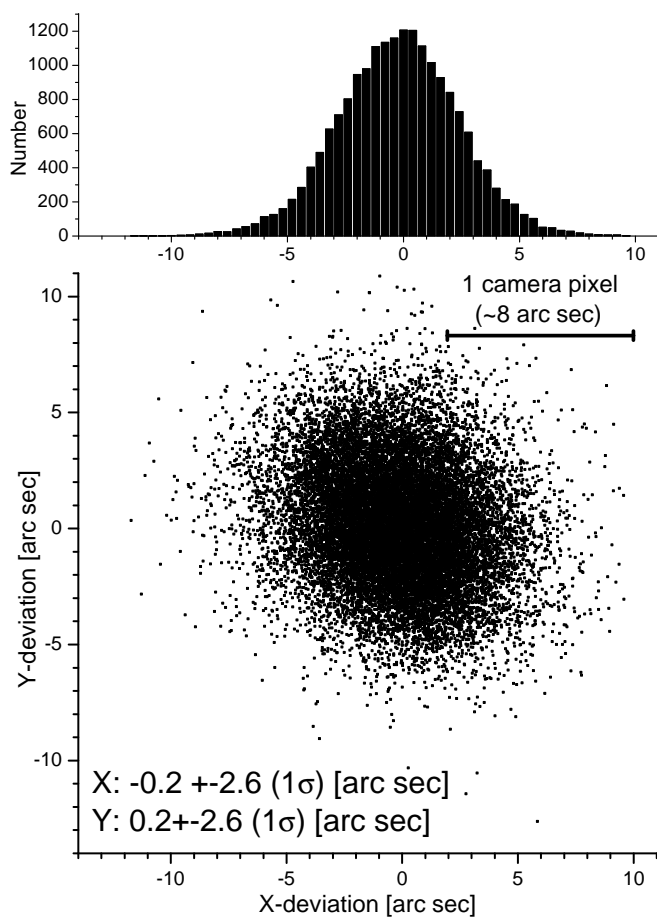


Figure 4.12: Distance between the centers of the 2 fitted ellipses corresponding to the solar disk and the field stop opening as a 2D plot (lower graph) and the associated histogram along the x-direction (upper graph). The units are given in tracking angle deviations. The data has a 2-D 1σ interval of less than 4 arc sec and was recorded on 22th of September 2010, 10:29–16:43 UTC and 23th of September 2010, 07:54–12:36 UTC, in two second intervals. (Image taken from Gisi et al. (2011))

4.5.2 Solar line shifts

A second possibility to determine the tracking accuracy is by investigating the solar lines in the spectrum. Mispointing of the solar tracker can generate a Doppler shift of the solar lines with respect to the telluric spectral features due to the solar rotation, which is shown schematically in Fig. 4.13. The synodic ro-

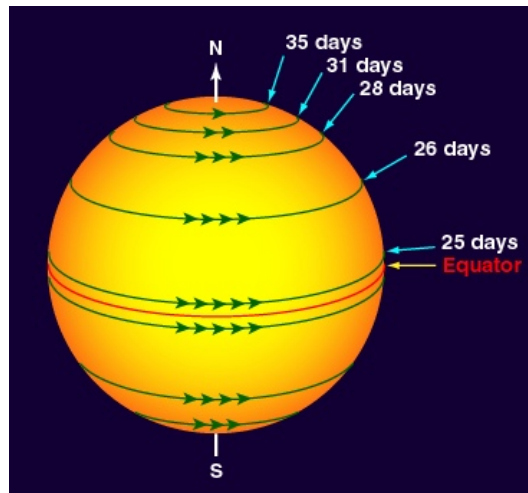


Figure 4.13: Latitude-dependent sidereal rotation period of the Sun (from: <http://scienceblogs.com/startswithabang/2010/10/07/counterclockwise-but-there-are/>)

tation period of the Sun at its equatorial region (which is the period as seen from the moving Earth) is about 26.75 days, which corresponds to an observed equatorial solar velocity of about 1890 m s^{-1} (Lang, 1991). A mispointing along the solar equator of 1 arc min translates into a Doppler scaling $\Delta v/v$ of 3.9×10^{-7} . If this effect is considered in the analysis by fitting a separate shift for the solar background lines, the effects on the trace gas analysis are minor, but it gives a useful method to estimate the pointing quality at hand. Note, however, that the mispointing cannot be retrieved unambiguously from the observed Doppler shifts, because there is no sensitivity along the direction parallel to the solar rotation axis. For this reason, in the following an additional factor of $\sqrt{2}$ is applied when estimating the total pointing error for two dimensions (2D), assuming that the pointing uncertainty is of the same size for any direction on the solar disk.

For the analysis the software PROFFIT Ver. 9.6 (see section 2.2.2) was used. A model of the solar absorption lines is included in this code (Hase et al., 2006) and (Hase et al., 2010). To calculate the shifts of the solar lines, the movement of the observer is included, where the location of the observer on the rotating Earth, the position of the Earth on its elliptic orbit and the influence of the Moon is accounted for. The precision of these calculations results in errors below ± 4 arc seconds for the retrieved pointing accuracies. To estimate tracking accuracies, the spectra measured at the FTIR sites in Kiruna, Izaña and Karlsruhe are evaluated.

The solar trackers in Kiruna and Izaña initially were controlled by a quadrant diode. However, the setups

differed as described in section 4.1. The camera based system replaced the quadrant diode in September 2010 in Kiruna and April 2012 in Izaña, respectively.

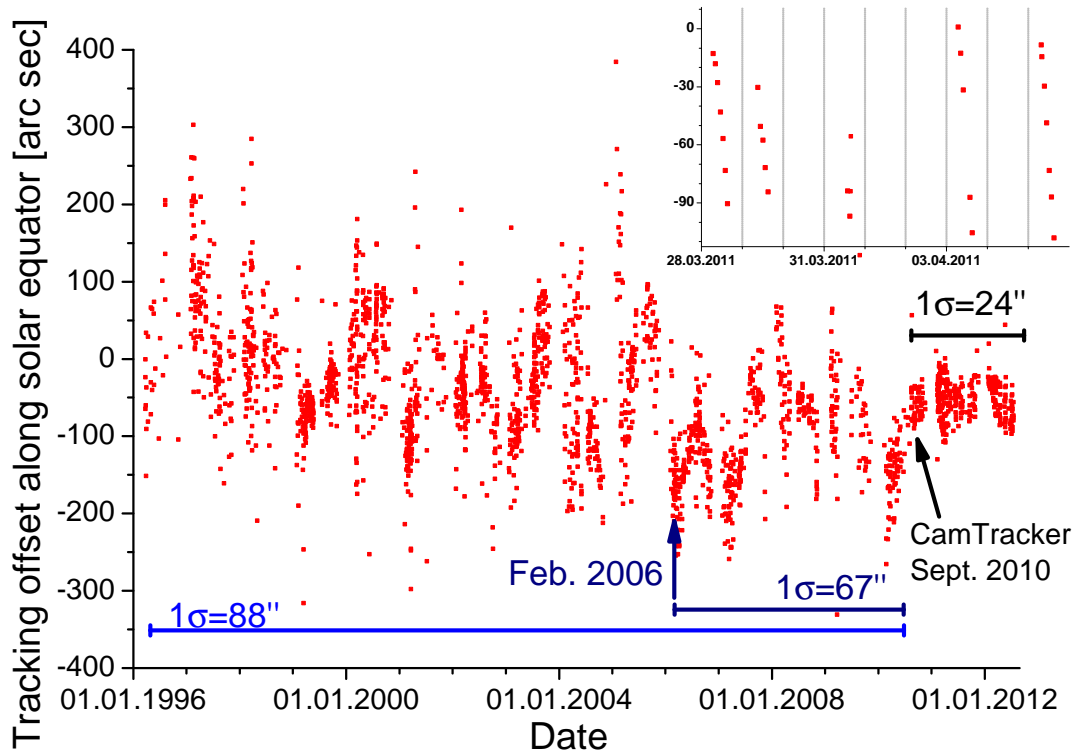


Figure 4.14: Tracking offsets in Kiruna retrieved by observing the solar line shifts in MIR spectra around 2704 cm^{-1} . The values are not centered around zero which could be due to incorrect values of the solar line positions. This however has no significance, which is why only the scattering around mean values are discussed in this chapter. The graph at the top right side is a zoom into the time series after installation of the tracker. The residual offsets follow a daily repetitive pattern. Apart from this, the scattering is very low.

The deduced pointing accuracy for Kiruna is shown in Fig. 4.14, indicating a tracking accuracy of ± 95 arc seconds ($\approx \sqrt{2} \cdot \pm 67$ arc seconds) in the three years before the CamTracker was installed. Note that any realignment of the quadrant sensor tends to affect the quality of the tracking, this is probably the reason for the reduced scatter since February 2006. After the installation of the CamTracker in September 2010, the precision improved to $\pm 34''$ ($\approx \sqrt{2} \cdot \pm 24''$). This value is a factor of about three lower, showing a significant improvement induced from the camera based system. Nevertheless it is not within the desired range of 20 arc sec. The variation in the remaining tracking offset shows a systematic pattern with continually decreasing values each day, as can be seen in the zoomed region in Fig. 4.14. The reasons for these are not clear yet, although several attempts were made to correct this behavior remotely. For example, the recorded solar image intensity varies gradually along the vertical direction, which might cause the observed systematic effects. However, a software-based correction of this intensity variation was not successful. A discussion about errors can be found in section 4.5.3. As a next step, an on

site inspection of the light path and the orientation of mirrors would be necessary, which however was not performed yet due to the remoteness of the site. The current accuracies in Kiruna correspond to an air mass uncertainty of about 0.09% at a solar zenith angle of 80° , which is about 2 times higher than desired. Nevertheless this is a very good value compared to other NDACC or TCCON stations, having a tracking accuracy of several arc minutes (Toon and Wunch (2010)).

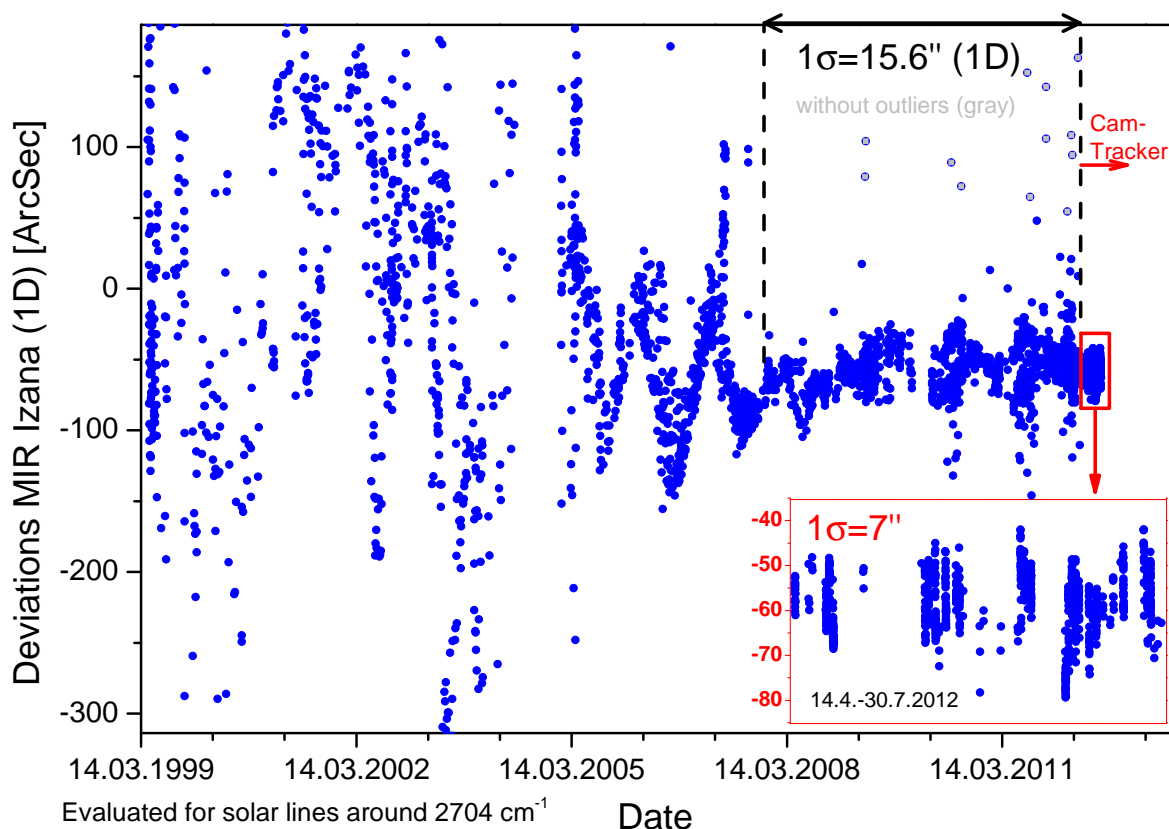


Figure 4.15: Tracking offset for Izaña in the MIR, showing a very good value of 22 arc seconds ($=\sqrt{2} \cdot 15.6''$) since 14th of November 2007. After 14th of April 2012 the CamTracker was used as the optical feedback.

For the FTIR site Izaña, the tracking offsets are shown in Fig. 4.15. After the setup with the semitransparent mirror was installed in February 2005 and further realignments of the quadrant diode were made in May 2007, an accuracy of $\pm 22''$ ($\approx \sqrt{2} \cdot \pm 15.5''$) was reached. The final accuracies in Izaña are nearly sufficient for the desired gas retrieval precision of 0.1% (see section 3.2), resulting from the advantageous setup of the quadrant diode behind a semi-transparent mirror. After the setup of the CamTracker system at 14th of April 2012, the available time series is too short to make a good quantitative evaluation. However, the available data indicate an excellent pointing precision of $10''$ ($\approx \sqrt{2} \cdot \pm 7''$).

At the Karlsruhe site, the CamTracker system was used since the FTIR became operational in April 2010. The tracking offsets deduced from the solar line shift are displayed in Fig. 4.16 for two spectral regions. In the NIR, a tracking accuracy of $\pm 17.4''$ ($\approx \sqrt{2} \cdot \pm 12.3''$) can be estimated, in the MIR the values are about 1.5 times higher. This discrepancy most probably results from disturbances of interfering gas

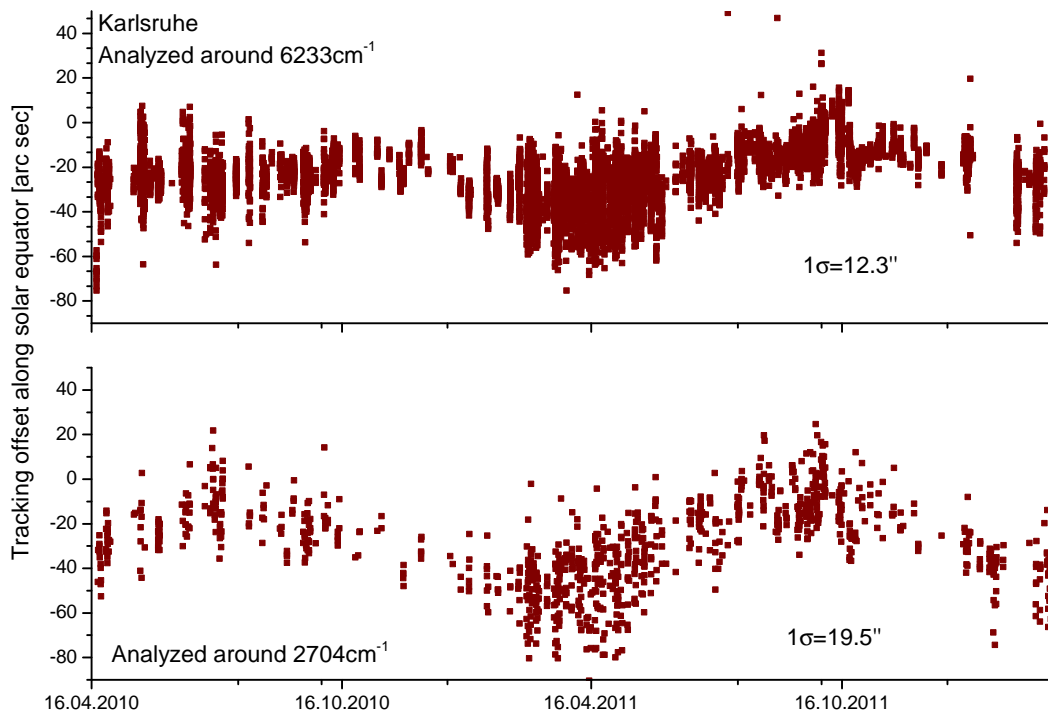


Figure 4.16: Tracking offset in Karlsruhe, where 2 spectral windows were evaluated, which were recorded with different detectors.

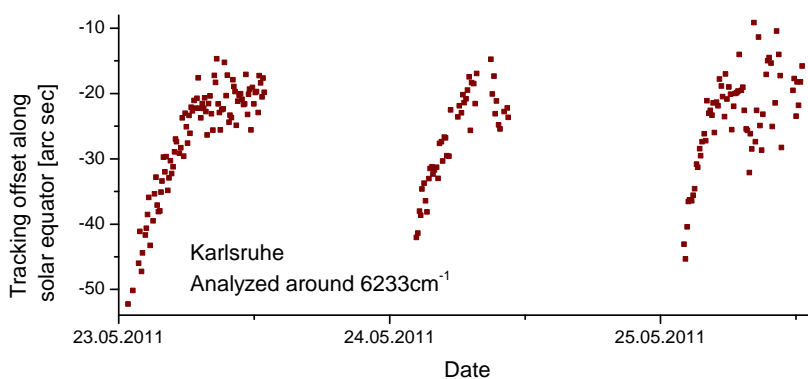


Figure 4.17: Zoom into Figure 4.16 to visualize the systematic intraday offsets. The accuracies deduced from the ellipse center positions for 23th of May 2011 were $-0.8'' \pm 2.3''$ and $-0.3'' \pm 2.6''$. Therefore, these offsets do not result from erroneous controlling of the mirrors.

species, such as H₂O in the MIR spectral window used and errors in the solar line list. Interfering water vapor spectral features might also be the reason for the observed annual cycle. This example shows the limits of the solar scaling approach.

As seen before for Kiruna, the main deviations result from systematic intraday offsets, which is shown in Fig. 4.17, consistent for both detectors. The size depends strongly on the length of the observation per day. In summer, with up to 13 hours of measurements, this structure extends further to negative offset values, but not towards positive values, which most probably results from the insensitivity for mispointings along the solar rotation axis. This effect causes the apparent annual structure in the upper panel of Fig. 4.16. The reasons for these offsets, being up to about ± 20 arc seconds, are not completely clear, as discussed in section 4.5.3.

To conclude, it is important to state that besides the systematic offsets, the statistical errors are very low in the order of less than 5 arc seconds. A further example of this high precision will be shown in sec. 4.6.

4.5.3 Error budget of the camera-based system

In this section contributions to the tracker pointing error budget are given. They are listed in a combined form in table 4.1, followed by a further discussion of selected items.

Image reconstruction*	2'' at good conditions, up to $\approx 20''$ in the presence of clouds
Tilt of field stop**	8.8''
Perspective distortion	<2''
Atmospheric dispersion***	up to 3.6'' at 80° SZA
Apparent solar flattening	<0.4'' at 80° SZA
Motor increment	3.6''
Finite control loop duration	< 2''
Positioning of detector in FTS	up to 10''

*Finite pixel size, sensor noise + image granularity

**will be further reduced in future software upgrade

***is removed by proper analysis procedure (see sec. 3.3.6)

Table 4.1: CamTracker pointing error contributions in arc seconds.

Accuracy of image processing:

The theoretical accuracy to determine the center of an ideal circle is $\sigma = \frac{0.42}{\sqrt{d}}$ (Haralick and Shapiro, 1993), where d is the diameter of an observed circular contour in units of pixels, assuming negligible obliquities of the ellipses. For Karlsruhe, $d=240$ pixels for the big, and 48 pixels for the small ellipse. Two other sources limiting the accuracy are the noise generated by the image sensor and the granularity of the solar image. This granularity is due to the scattering properties of the matt finished aperture wheel surface (see figure 4.8). For good measurement conditions, these effects sum up to an error of about 2 arc seconds. With thick cirrus clouds, it rises up to about 15-20 arc seconds.

Tilt of field stop:

The field stop is tilted by about 10 degrees relative to the optical axis, to prevent back-reflections from its rear side into the spectrometer (see Fig. 4.18).

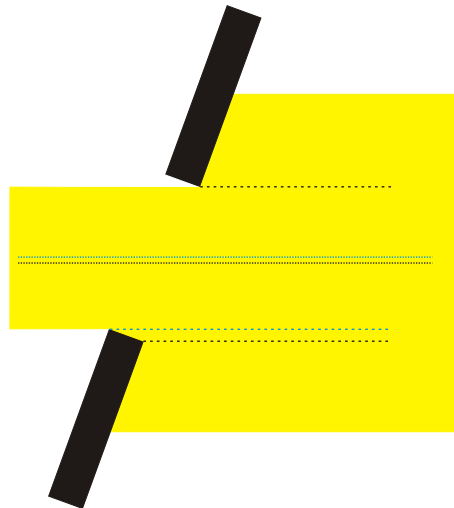


Figure 4.18: Schematic drawing of the light passing the tilted field stop. For this illustration, the field stop is tilted 20 degrees, and also the thickness is exaggerated. The black dashed lines are the borders of the field stop detected by the camera, resulting in a center as given by the black dotted line. The true center of the light passing the field stop is slightly higher as indicated by the blue dotted line.

However, due to the finite thickness of the field stop, this results in a deviation of the true and apparent center of the field stop. The currently used field stop has a thickness of about 0.2 mm for which an offset of 8.8 arc seconds can be calculated. In contrast to other errors such as the image reconstruction or the motor increment, this causes a daily repetitive, systematic effect. In future versions of CamTracker, this offset will be correctable by a separate input parameter, which, however, reduces the self-calibration capabilities of the system.

Perspective distortion:

Due to the aforementioned tilt of the field stop, the projected image of the Sun is not round. Instead, the width is slightly bigger than the height. In addition, the camera records this image, as well as the field stop, with a specific angle, which may induce an additional perspective distortion. The important question is whether these effects influence the determination of the true center of the solar image.

Pure geometric calculations give a shift of the solar disk center with respect to the center as defined from the rims of the solar image of 0.8 arc seconds. The subsequent recording of the camera from an angled view increases this difference to 1.8 arc seconds, which would still be negligible for our purposes. These calculations were made for the Karlsruhe camera setup (15 degrees viewing angle with respect to the optical axis in 24 cm distance from the field stop). These results agreed within the errors with an experimental evaluation of the image of a lamp on the field stop from various viewing angles.

The calculated effect onto the diameter in the horizontal direction is bigger. The vertical and horizontal diameters differ by 2.4%, which corresponds to about 6 pixels for Karlsruhe. However, the actual measured difference for the solar image is about 10 pixels (see Fig. 4.21), which is significantly larger than expected. The reason for this may be residual astigmatism induced by a non-ideally aligned off-axis mirror which forms the collimator of the FTIR spectrometer.

Atmospheric dispersion:

As described in section 3.3.5, the refraction of the radiation depends on its wavelength. As the camera records in the visible and the spectrometer records in the IR, the respective centers of the Sun are different. As given in table 3.1, at 80° this difference is up to 3.6 arc seconds. As this effect can be calculated later on when evaluating the spectra, it can be compensated, which is done in the current implementation of PROFFIT.

Refractive flattening of the Sun:

As the refraction varies with the elevation angle, the lower part of the Sun is affected stronger than the upper part. As a result, the Sun gets flattened at the lower side, so that the exact determination of the true solar center becomes more difficult. Fortunately this effect is rather small. At a SZA of 80 degrees, the influence by the refraction differs between the upper and lower rim by 0.4 arc seconds only, so that this effect can be neglected for our purposes.

Positioning of the detector:

Ideally, the detector inside the FTIR spectrometer should be aligned in a way, that it's center corresponds to the center of the entrance side of the field stop. In practice this may not be the case, as the detector is aligned towards a maximum signal. This misalignment results in a detector FOV different from the one defined by the field stop, and therefore can cause a daily repetitive systematic mispointing effect as observed in Kiruna and Karlsruhe. In Karlsruhe this was investigated for the InGaAs detector by

realigning the detector's position while observing it through the input field stop with a camera. However, these modifications did not show significant improvements.

Except for the last item, these listed errors can not explain the observed systematic daily shape of the pointing offsets of up to ± 20 arc seconds for Karlsruhe and ± 35 arc seconds for Kiruna (see figures 4.14 and 4.16). The reasons for these disagreements could not be determined within this work. One possible source could be an asymmetric projection effect of the solar image, resulting from a misaligned off-axis parabolic mirror. To check for this, sample measurements with reduced beam diameters will be made, as this should reduce effects from misalignments.

4.6 Further indications for the LOS sensitivity of the CamTracker

The current CamTracker software provides many available tracking parameters, which can be saved in regular intervals. Examples are the actual solar image on the field stop, the retrieved tracking offsets to the astronomical angles, which are necessary for a centered solar image or the central positions of the solar image and the field stop. By analyzing these large dataset, two effects were found which were not expected initially and are described in this section. They demonstrate the very high precision, both of the optical system itself and the successive image processing.

4.6.1 Aperture position

As described previously, the field stop of the IFS125 spectrometers is made of a metal disk with holes of different diameters. It can be rotated around its center, to move a desired field stop diameter into the optical path, which is done by a stepper motor. As the image processing also determines the center of the field stop, its actual position is determined continuously. In Fig. 4.19 these positions are shown for different field stop diameters. In the tangential direction (rotation direction of the field stop wheel) periodical deviations can be seen. These deviations therefore most probably originate from the discrete rotation angles of the stepper motor. The deviation in the radial direction probably results from an aperture wheel centering error.

As a consequence from these results, the most relevant field stop should be used when aligning the spectrometer. Measurements with other field stops will alter the ILS and also change the observed solar region. A smaller step size of the motor therefore would be beneficial for a further generation of spectrometers.

A shift of the field stop position of 0.08 mm, which is the maximum difference observed in Fig. 4.19, corresponds to a pointing offset of 40 arc seconds. In contrast to the camera-based system, the quadrant diode does not take into account the actual field stop position. It assumes fixed positions of the field stop, which therefore would lead unavoidably to pointing errors up to ± 40 arc seconds.

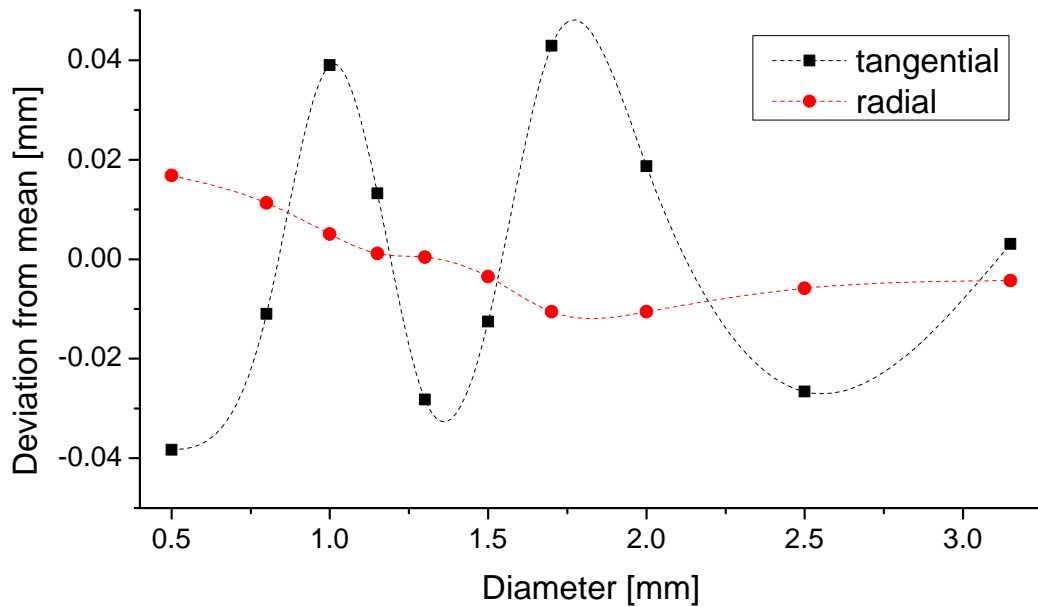


Figure 4.19: Variations in the central positions of the field stop in Karlsruhe, as determined by the image processing. The dashed lines are drawn for visualization reasons only.

4.6.2 Tilting of the spectrometer

The offsets derived from the camera optical feedback, as displayed in Fig. 4.6, are saved in a file periodically. A closer inspection (see Fig. 4.20) shows systematic triangle-shaped structures with different widths and amplitudes which coincide with the times when measurements were taken. In the time ranges denoted as A and B, 4 scans (2 forward and 2 backward) with a resolution of 0.0055 cm^{-1} (180 cm OPD), in C four scans with 0.014 cm^{-1} (64 cm OPD) were taken. The reason for this influence of the measurements onto the tracker position is the bearing of the whole instruments on springs, which reduces the influence from external vibrations. However, as the moving mirror changes its position, its weight of about 2 kg causes a slight tilting of the spectrometer, which has to be compensated by the tracker. At higher resolutions, the mirror moves further, which is the reason for the different amplitude between the ranges A/B and C. The necessary correction onto the elevation mirror was about 25 arc seconds for the high resolution scan, and about 7 arc seconds for the low resolution measurement. This shows the high precision of the image processing.

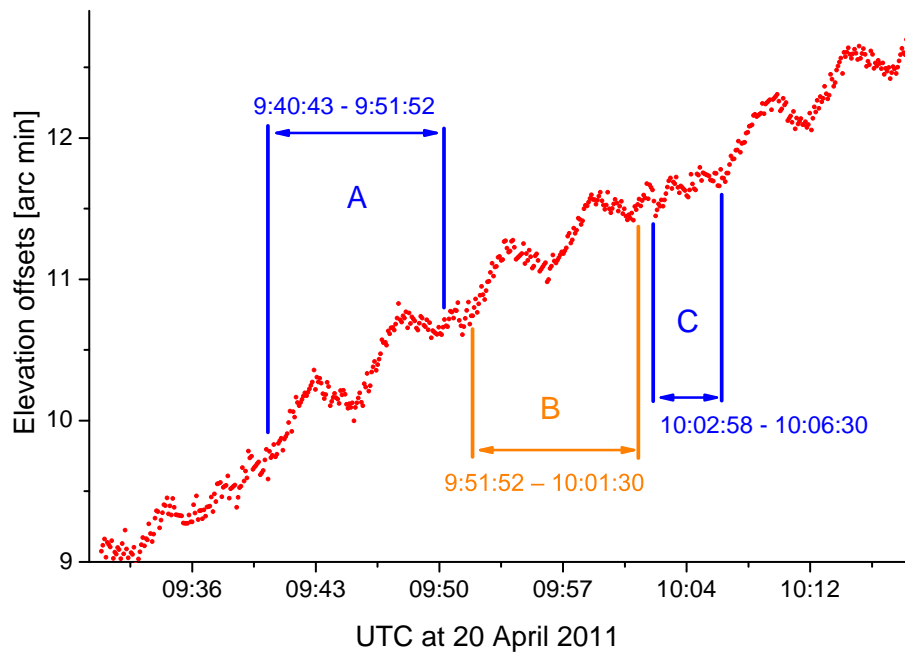


Figure 4.20: Repetitive structures on the elevation motor offsets in Karlsruhe derived from the optical feedback.

4.7 Tracking software

To operate the solar trackers, an easy-to-use program with a graphical user interface was created. It takes care about the recording of images with the camera, the image processing and the controlling of the tracker. It was programmed using several freely available open source C++ software libraries: QT³, a cross-platform development framework, OpenCV⁴, an image processing library and Eigen⁵, a matrix and vector calculation library. Using these has the benefit, that the program is not limited to the WindowsTM operating system; it was successfully tested under Linux (Ubuntu). The graphical user interface of the CamTracker program (see Fig. 4.21) provides an image of the camera, on choice combined with the retrieved ellipses, and its histogram. In addition, several settings are easily accessible by sliders and buttons, such as the exposure time (if not chosen automatically) or the option to use the results of the circle fit instead of the ellipse, which is useful when tracking the non fully illuminated Moon (see Fig. 4.8). In the standard operation, the program decides automatically whether to choose the circle or the ellipse for the rim of the Sun, depending on the quality of the fit. Next to the tracking offsets, the program can also save the retrieved image in user-specified intervals. With these, an inspection of the tracking accuracy, as well as an identification of unexplained intensity variations in the interferograms can be performed after the measurement.

The program takes care about varying illumination conditions by adjusting the exposure time of the

³<http://qt.nokia.com/products/>

⁴<http://opencv.willowgarage.com/wiki/>

⁵<http://eigen.tuxfamily.org>

camera. Changes of the field stop diameter are recognized as well, which is necessary for finding the correct threshold value in the brightness histogram.

All parameters are saved in a configuration file, which has to be set up prior to the first usage. As the tracker types which can be controlled vary both in their optical setup (alt-azimuthal, single-mirror) the motor controller types (NewportTM, SynScanTM⁶, NanotecTM) and the communication protocol (RS232, RS485, TCP/IP), the program was designed to handle all these types simply by choosing the correct option in the CamTracker configuration file. The trackers are described in chapter 5.

4.8 Conclusion of the camera-based tracker system

A novel optical feedback system for solar trackers (CamTracker) was developed, which records the solar image on the spectrometer's input field stop. It is easy to set-up, robust for distortions from thin clouds and showed significantly higher tracking accuracies compared to common quadrant-diode based systems. The CamTracker setup was installed at the FTIR measurement stations in Karlsruhe, Kiruna, Izaña and Alzomoni. In addition, it was integrated into the tracking system of a portable spectrometer (see sec. 6). The tracking accuracies in Karlsruhe, Kiruna and Izaña derived from actual measurements were 17, 34 and 10 arc seconds, respectively. Especially in Kiruna, the main part of these values presumably stem from misaligned optical components of the spectrometer, and not from the tracker itself. This can be seen from the fact, that positioning of the solar image on the field stop showed a precision of better than 5 arc seconds.

⁶http://www.skywatcher.com/swtinc/customer_support.php?class1=1

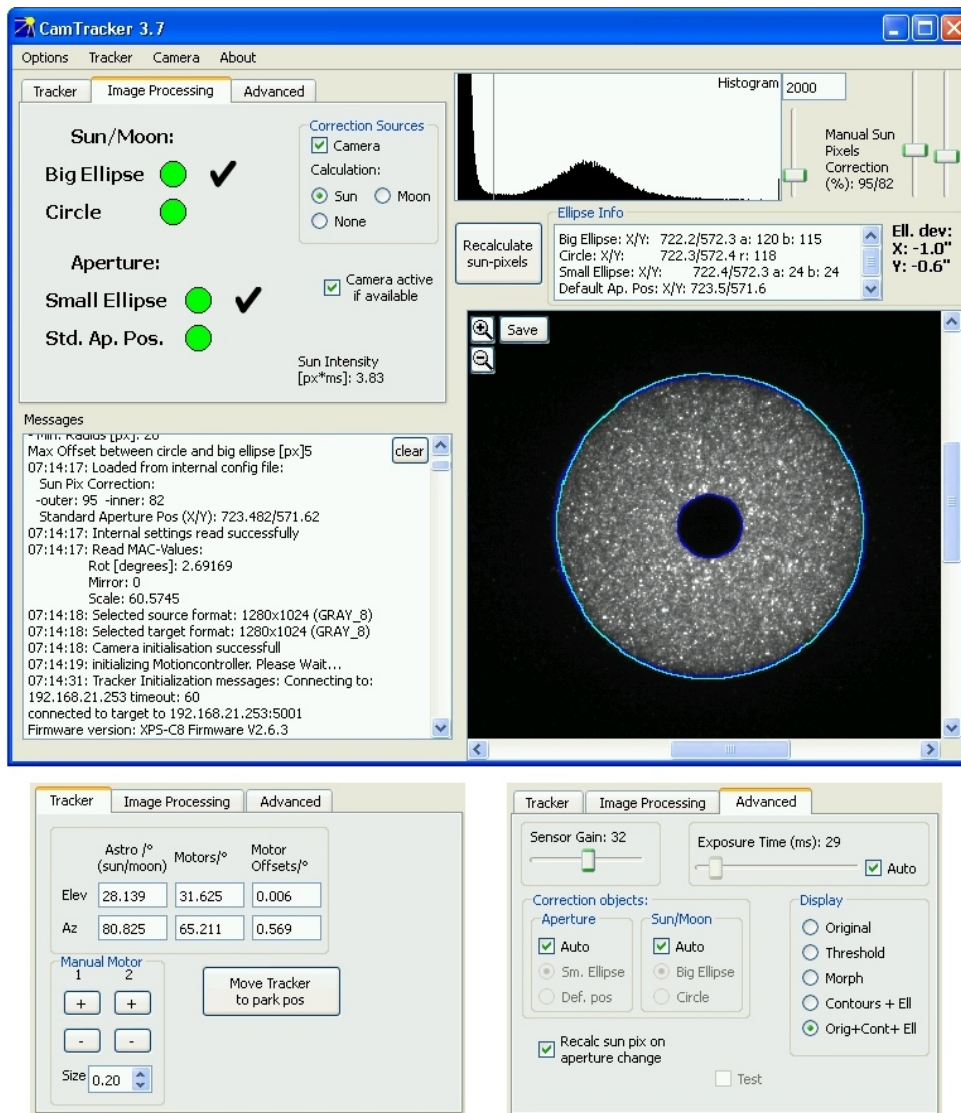


Figure 4.21: Screenshots of the CamTracker software while tracking the Sun. The upper image shows a live picture of the camera, optionally combined with the retrieved ellipses and circles. Above, the current histogram, together with the actual threshold is displayed. The text field in between shows the central position and radii of the retrieved ellipses and the circle. The default position is used, when no small ellipse can be found, e.g. when the field stop is outside the solar disk image. The actual tracking accuracy in arc seconds, as derived from the ellipse positions and diameters, is displayed as bold numbers right of the text field. On the left part of the top panel, the user can select, whether a astronomical calculation should be used as a base tracking information, and if the camera information shall be taken into account. To visualize the current tracking status at a quick glance, green circles and red hexagons (not shown) indicate the quality of the retrieved ellipses. The check marks show which information currently is used. The text field at the bottom left gives status information of the tracker. In the bottom left panel, the coordinates from the astronomical calculation, the current mirror angles and the offset retrieved from the optical feedback are displayed. In the bottom right panel the user may disable the automatic exposure time finding and the automatic determination, which element should be used for the Sun and the field stop.

5 Solar tracker systems

In the context of this work, the existing alt-azimuthal tracker systems in Kiruna, Izaña and Karlsruhe were upgraded to be controlled with the camera-based optical feedback system. These will be described in section 5.1.1. In addition, two new setups were built. One is a low-cost tracker, based on mechanical components normally used in astronomy for telescopes, and contains only one motorized mirror. More details are given in section 5.1.2. The second is a standard alt-azimuthal type tracker, the focus was put on a small size and low weight to make it transportable and versatile applicable (“mini-tracker”). The mechanical setup is shown in section 5.1.3, a first and very successful application with a small spectrometer is described in chapter 6.

Section 5.2 gives an overview about the calculations involved to determine the correct tracker angles for a given solar elevation and azimuth angle. In addition, the formulas to model the light path through the tracking setups is presented.

5.1 Tracker set ups

5.1.1 Alt-azimuthal “Newport”-setup

The “NewportTM” tracker was mechanically designed and built by S. Huster (see Huster (1998)) and the mechanical workshop of the IMK. It is in use at the FTIR sites in Kiruna, Izaña and Karlsruhe. The motors (RV80PP, RVS80PP, RV160PP, RTM80, RTM180) and the controllers (MM4006, XPS) were purchased from NewportTM. This has the advantage of getting a ready-to-work, highly sophisticated motor controller, which on the other hand, reflects in a rather high price. A letter-box shaped, automated cover was built in cooperation with the company Impres¹. It can be opened and closed with pressurized air. When closed, inflatable sealing tubes protect the tracker very efficiently from water and dust at the outside.

The tracker is an alt-azimuthal system (see Fig. 4.2 on page 63) with ellipse-shaped plane mirrors having 12 cm as the projected diameter and an uncoated aluminum layer. The lower motor is able to move a considerable weight and is also carrying the “letter-box” shaped cover of the tracker so that the opening is always orientated into the observing direction. This cover can be opened, closed and sealed with pressurized air. The lower motor offers a hollow axle diameter of 11 cm, through which the light falls downwards to the FTIR.

An image of the tracker in Kiruna is shown in figure 5.1.

¹<http://www.impres-gmbh.de/>



Figure 5.1: Tracker in Kiruna on the roof of the IRF building. The letter-box cover can be moved by pressurized air, which is also used to inflate the red sealing.

5.1.2 Astronomical mount

For the FTIR which was shipped to Altzomoni in Mexico, a new type of tracker was designed as the “Newport” trackers are rather expensive, the “letter-box” cover is complicated to produce and additional infrastructure such as a compressor and a controlling unit for opening and closing is necessary.

As astronomers also require a good tracking when observing the sky, in general done by moving the whole telescope, a Vixen GP2 telescope mount driven by stepper motors from the “Skywatcher SynScan GoTo Kit” was used as a basis. The declination axis was disassembled and attached to the right-ascension axis in a way, that a 12 cm diameter elliptic mirror can be rotated around 2 axes, where the central point of the mirror (in the following denoted as the optical center of the tracker) remains stationary. An image of the setup is shown in Fig. 5.2, already applied onto the container in Altzomoni. During tracking, this mirror has to be orientated in a way, that the solar radiation is reflected on a second elliptic mirror (target mirror), which reflects the radiation downwards into the FTIR measurement container. As Altzomoni is a low-latitude site, the Sun has high elevation angles except for early in the morning and late in the evening. Therefore, to keep the projected effective diameter of the moving mirror large, the angle between the incoming and reflected radiation has to be kept small by locating the target mirror above the moving one.

It is also possible to orient the tracker in an equatorial way, so that the rotation axis of the lower motor is parallel to the Earth’s rotation axis, and the target mirror is positioned on this axis. This setup has the

advantage to achieve a rather accurate tracking of the Sun by simply rotating around this single axis with a uniform speed.

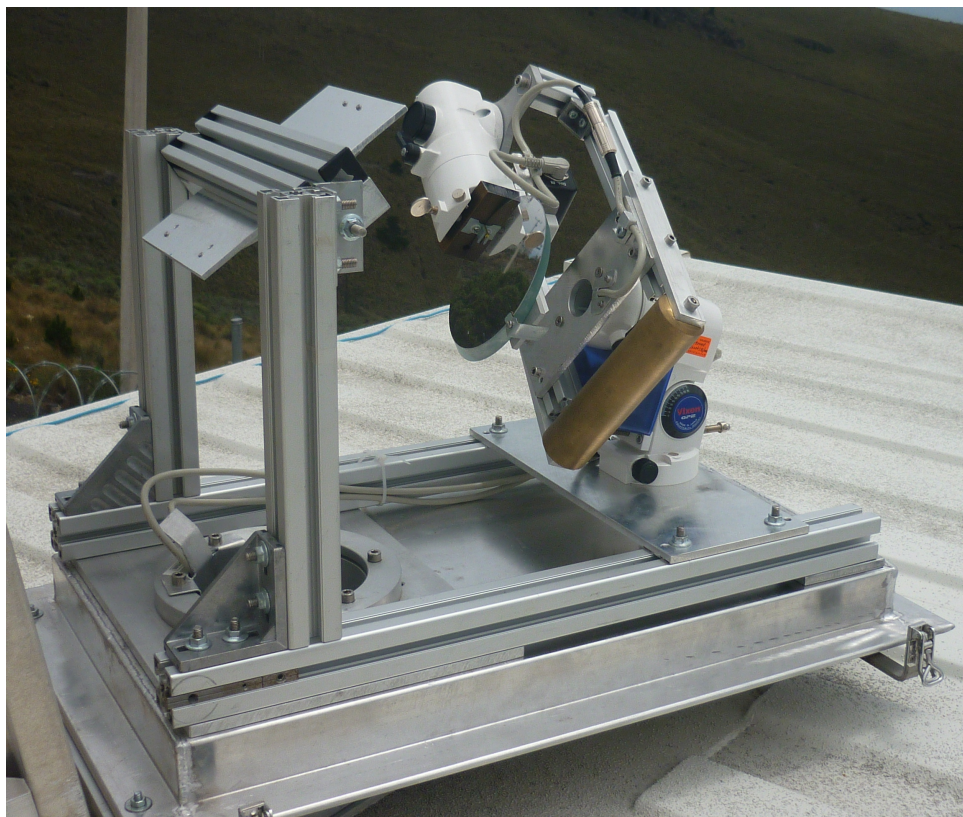


Figure 5.2: Setup of the “astronomical mount” tracker on top of the FTIR container in Altzomoni, Mexico. The fixed mirror which reflects the radiation into the container is located above the rotating mirror.

5.1.3 Miniaturized setup

Within the course of this work the possibilities to determine accurate XCO_2 values with a small and portable FTS were examined (see chapter 6 on page 97). The aim was to attach the tracker directly to the FTS, to get a self-standing measuring setup. As the size and the weight of the two other trackers would have compromised the portability of the setup, a small and lightweight tracker was required, which still offers a high tracking precision.

After investigations on motor types and possible setup configurations, it was decided to realize an alt-azimuthal tracker, with 2 stepper motor driven rotation stages. The complete tracker weights about 2 kg and has the dimensions 30 x 20 x 10 cm. It supports a beam diameter of 50 mm, which actually turned out to be much wider than required for the purpose of measuring XCO_2 as described in chapter 6. However, this allows to apply the tracker for other kinds of observations (e.g. lunar, open path, emission measurements).

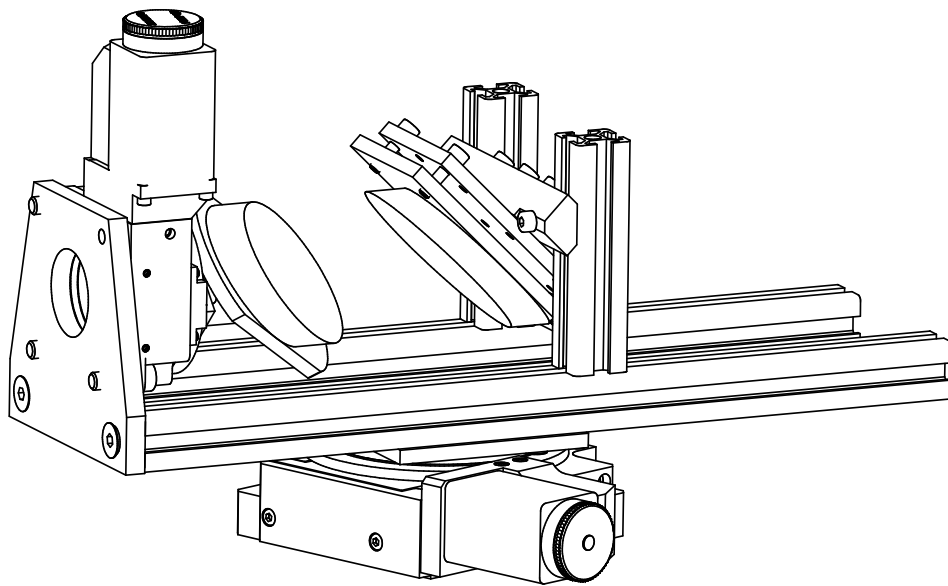


Figure 5.3: CAD drawing of the miniature tracker used for the low-resolution XCO_2 -measurements.

Two rotation stages with hollow axles from Standa², the 8MR151 and the 8MR190-2-28 were used, the latter rotation stage offers a 2 inch free aperture. They are driven by stepper motors controlled by a home-made motor controller unit using the “SMCI12” motor drivers from Nanotec³, allowing a microstep size of 1/64th of a full step, which results in a theoretical 0.56 arc seconds resolution along both axes.

The mirrors are elliptic glass plates with SiO_2 protected aluminum coating.

As the other trackers, it is controlled by the CamTracker software via a TCP/IP connection. A CAD drawing of the tracker is shown in Fig. 5.3, a photo is displayed in figure 5.4.

²<http://www.standa.lt>

³<http://www.nanotec.com>

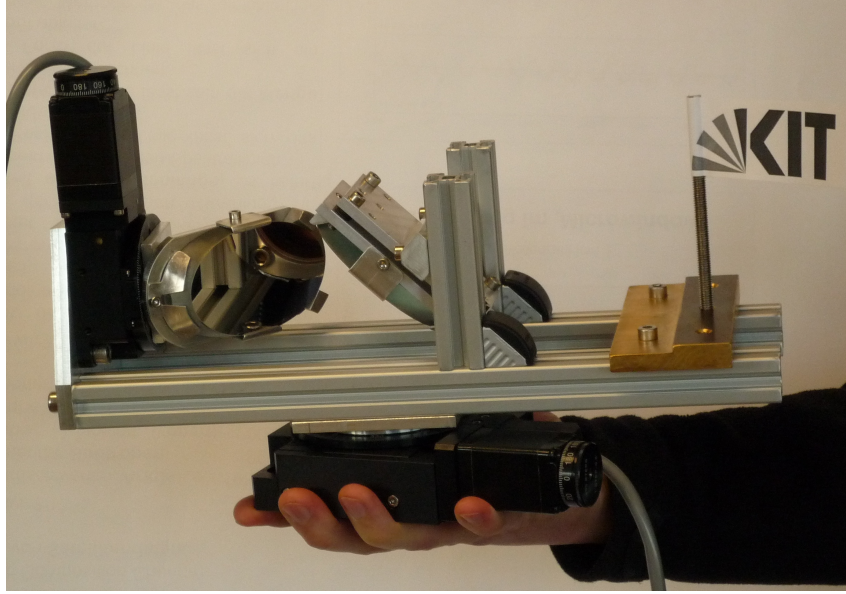


Figure 5.4: Image of the tracker as built by the mechanical workshop. The copper bar on the right serves as a counterweight to balance the weight distribution above the lower motor.

5.2 Calculation of mirror angles

To calculate the angles for the solar tracker, a transformation has to be performed from the local horizontal coordinate system, in which the solar position can be calculated (see section 3.3) to the coordinates of the tracker. This can be orientated arbitrarily and has to be known. The orientation can be described by 3 rotation angles around three orthogonal axes. The definitions of the angles for the current implementation are described in figure 5.5.

Mathematically, the transformation of any vector \vec{v} in the local coordinate system ($x \hat{=} \text{South}$, $y \hat{=} \text{East}$, $z \hat{=} \text{Zenith}$) into the system defined by the tracker's base-plane orientation can be described very easily by rotations around three axes with three angles (Euler angles) using rotation matrices:

$$\vec{v}_{tracker} = R_y(-\alpha) * R_x(-\beta) * R_z(\gamma) * \vec{v} \quad [5.1]$$

Where $R_{x,y,z}$ denote the standard rotation matrices around the 3 Cartesian axes:

$$R_x = \begin{pmatrix} 1 & 0 & 0 \\ 0 & \cos(\beta) & -\sin(\beta) \\ 0 & \sin(\beta) & \cos(\beta) \end{pmatrix}, \quad R_y = \begin{pmatrix} \cos(\alpha) & 0 & \sin(\alpha) \\ 0 & 1 & 0 \\ -\sin(\alpha) & 0 & \cos(\alpha) \end{pmatrix}, \quad R_z = \begin{pmatrix} \cos(\gamma) & -\sin(\gamma) & 0 \\ \sin(\gamma) & \cos(\gamma) & 0 \\ 0 & 0 & 1 \end{pmatrix}$$

To get the vector \vec{v} in the Cartesian coordinate system from a given elevation and azimuth angle, it has to be transformed as follows:

$$\vec{v}_x = \cos(az) \cdot \cos(elev), \quad \vec{v}_y = -\sin(az) \cdot \cos(elev), \quad \vec{v}_z = \sin(elev)$$

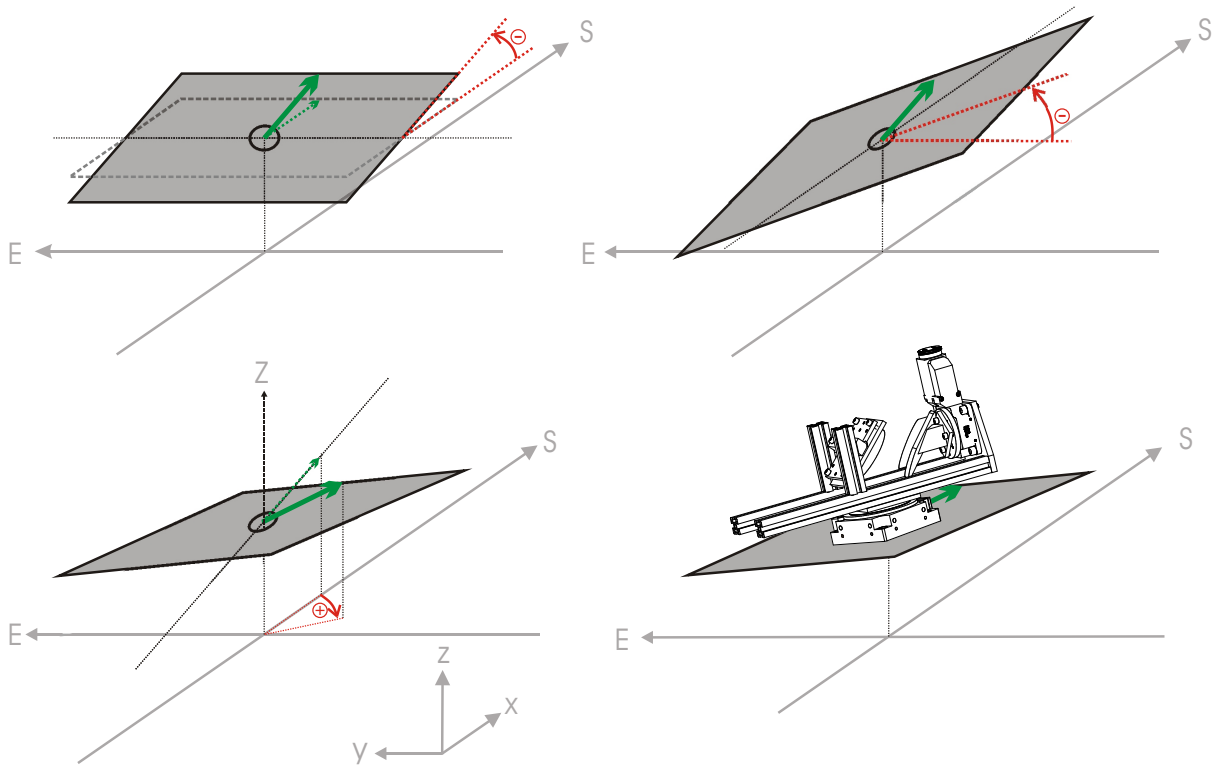


Figure 5.5: Transformation from the local horizontal coordinate system to the tracker system as implemented in the current Tracker Software. As the basis the plane around the lower rotation motor is taken, with a initial orientation facing directly southwards. The transformation order is the following: 1: Tilt North-South (α). 2: Tilt East-West (β). 3: Rotation around Zenith (γ). The + and - signs denote the sign which has to be taken for the displayed rotation direction.

The back-transformation is given by:

$$elev = \arcsin(\vec{v}_z/|\vec{v}|), \quad az = -atan2(\vec{v}_y/|\vec{v}|, \vec{v}_x/|\vec{v}|)^4$$

The calculation of the required tracking angles depends on the optical set up of the tracking system. The two types presented within this work are described in the following.

Alt-Azimuthal setup In an alt-azimuthal setup, the required motor angles for the lower and upper motor to point to a desired direction, are equal to the elevation and the azimuth of the desired direction (in the tracker's base plate coordinate system), which makes the system very simple to implement.

As one also has to simulate the effect of a mirror angle variation for the position of the solar image on the field stop (to calculate the MIC described in section 4.3.2), one has to calculate the light path through the tracker, depending on its orientation. In the tracker-based system this can be done using rotation matrices as well. When denoting the rotation of the lower and upper tracker motors as θ_{az} and θ_{elev} ⁵, the effect onto the incoming vector \vec{v}_{track} is:

$$\begin{aligned} \vec{v}'_{track} = & R_z(-\theta_{az}) \\ & * R_x(45^\circ) * M_{xz} * R_x(-45^\circ) \\ & * R_y(-\theta_{elev}) \\ & * R_z(45^\circ) * M_{yz} * R_z(-45^\circ) \\ & * R_y(\theta_{elev}) \\ & * R_z(\theta_{az}) * \vec{v}_{track} \end{aligned}$$

The matrices M_{xz} and M_{yz} describe a reflection with respect to the x-z and y-z-planes:

$$M_{xz} = \begin{pmatrix} 1 & 0 & 0 \\ 0 & -1 & 0 \\ 0 & 0 & 1 \end{pmatrix}, \quad M_{yz} = \begin{pmatrix} -1 & 0 & 0 \\ 0 & 1 & 0 \\ 0 & 0 & 1 \end{pmatrix}$$

Single mirror setup With only one mirror, which can rotate about 2 angles around its central point, the required calculations look different. The first step to transform vectors to the tracker's base-plane coordinates is the same than described above. In the initial orientation of the tracker ($\alpha = \beta = \gamma =$

⁴The function $atan2(x,y)$ calculates the angle (0° - 360°) between the positive x-axis and the point given by x and y. It is implemented in common programming languages such as Fortran, C++ and Java. The standard $arctan(x/y)$ would give values always between -90° and 90° only.

⁵The lower and upper motors are often denoted as azimuth- and elevation motors, respectively, as for an ideally orientated tracker ($\alpha = \beta = \gamma = 0$) they move the tracker's line-of-sight along the azimuth and elevation.

0) and motor angles of 0, the normal vector on the moving mirror is defined to point directly to the South. This vector is then moved along the azimuth and the elevation by the 2 motors, so that the motor axes, as before, are denoted as θ_{az} and θ_{elev} . The goal of the rotating mirror is to reflect the incoming radiation (with vector \vec{v} or \vec{v}_{track} in the local and the tracker's coordinate system, respectively) onto a fixed mirror, which then reflects the radiation into the measurement container. The position of this fixed mirror may be variable for different setups, so that it's direction has to be defined, e.g. by a azimuth and elevation angle relative from the moving mirrors central position. This direction will be denoted as the "target" vector \vec{v}_t .

When denoting the direction of the tracking object (Sun) as \vec{v} (always from the central point of the rotating mirror), then the normal vector \vec{v}_n of the rotating mirror has to point directly in between \vec{v} and \vec{v}_t , to reflect the radiation to the fixed mirror: $\vec{v}_n = \vec{v} + \vec{v}_t$. To get the actual mirror angles, this vector simply has to be transformed to the tracker's base plane coordinates using equation 5.1.

The calculation of the light path through the tracker is done by:

$$\begin{aligned} \vec{v}'_{tracker} = & R_z(-\theta_{az}) \\ & * R_y(-\theta_{elev}) \\ & * M_{yz} \\ & * R_y(\theta_{elev}) \\ & * R_z(\theta_{az}) * \vec{v}_{tracker} \end{aligned}$$

For both tracker setups, the modeling of the light path ends at the first fixed mirror. This is possible, as all the effects of the subsequent (and fixed) mirrors can be determined automatically with the CamTracker setup as described in section 4.3.2.

Of course, the three degrees of freedom for the tracker orientation (α, β, γ) and the nominal orientation of the tracking mirrors, can't represent the complete true setup. For this more orientation parameters would be needed as demonstrated in Huster (1998), where 10 parameters were determined by using stars at night-time. However these values are time-consuming to determine and showed to be dependent on the ambient temperature. From the experience gained within this work, the chosen simplification using only three orientation parameters is sufficient, as the optical feedback provided by the camera compensates all the misalignments of the tracker.

When recording the mirror offsets relative to the astronomically determined mirror angles for the course of a day, it is possible to retrieve better values for the initially chosen tracker orientation angles (see Huster (1998) and Merlaud et al. (2012)). However, for the setups used within this work, this was not necessary.

6 CO₂ measurements with a low-resolution spectrometer

In this chapter, the possibilities of retrieving atmospheric XCO₂ values with a portable, low-resolution spectrometer are investigated. The results of this were published in Gisi et al. (2012), from which parts were adopted for this chapter.

6.1 Motivation for portable spectrometers

Within the last several years, it has been recognized that a precise knowledge of the global abundances of greenhouse gases such as CO₂, N₂O and CH₄ is required for understanding the mechanisms of the global carbon cycle and to determine its sources and sinks (Olsen and Randerson, 2004). To measure column averaged mole fractions of these gases, several satellite-born instruments were developed such as SCIAMACHY¹, GOSAT² and OCO/OCO-2³. The latter two missions are exclusively dedicated on measuring greenhouse gases and OCO-2 is scheduled for launch in 2014. To support and validate these measurements great efforts have been undertaken to set up the TCCON (see section 2.2.3). The high-resolution TCCON spectrometers achieve an unprecedented accuracy of 0.25 % (≈ 1 ppm) for the atmospheric XCO₂ content (Wunch et al., 2011), which is the column-averaged dry air CO₂ mole fraction (see equation 3.3 on page 26).

To make the network results comparable to WMO (World Meteorological Organization) standards, the retrieved XCO₂ value is divided by a calibration factor of 0.989. This value was determined by comparisons with in situ profiles measured in the framework of aircraft campaigns (Wunch et al. (2010), Messerschmidt et al. (2011)).

Despite its outstanding capabilities such as the precision and stability during normal operations, the IFS125HR spectrometers from BrukerTM used by the TCCON also have their limitations. The IFS125HR is an expensive high-precision instrument, its large dimensions on the order of $1 \times 1 \times 3$ m and the mass well beyond 100 kg makes it difficult to transport, and its operation requires a significant amount of infrastructure, such as a stable support platform, air conditioning and sufficiently large lab space. For regular maintenance such as realignment and for repairs, an experienced person has to access the instrument, which can be difficult and time-consuming. The IFS125HR is not a portable spectrometer, moving it to a new site requires time-consuming start-up procedures. These obstacles impede the scientifically

¹<http://www.sciamachy.de/>

²http://www.gosat.nies.go.jp/index_e.html

³<http://oco.jpl.nasa.gov/news/>

important ground-based extension of atmospheric carbon column measurement on a global scale, e.g. in Africa, Asia and South America.

Some flexibility is gained by integrating the spectrometer into an overseas container including air conditioners and solar trackers (Notholt et al. (1995), Geibel et al. (2010)). But still, a truck and a forklift have to be available as the containers measure about 15ft (4.57 m) and weigh several tons. For field campaigns and for operation in remote areas with low infrastructure (the power consumption of such a container is on the order of 5 kW), this approach is hardly manageable.

To overcome these problems, the usage of smaller, cheaper and more easily transportable spectrometers was recently investigated to assess the ability to measure XCO₂. Besides the ability to be used easily in field campaigns, assuming a sufficient compactness and mechanical stability, the spectrometers could even be sent back and serviced by the manufacturer or the staff of the home institution for repairs or realignments, reducing the costs and effort significantly. A robust instrumentation which can be operated in a wide range of ambient temperatures would promote global deployment.

One alternative is the IFS125M instrument, which is smaller and less sturdy than the IFS125HR, while offering comparable resolution. Due to its lightweight design, the stability of the instrumental line shape (ILS) is not at the level of the IFS125HR spectrometer, so that it is difficult to achieve the long-term stability required by TCCON (priv. comm. V. Sherlock, NIWA, 2012). In addition, it still has a length of about 2 meters and requires on-site realignment by qualified personnel. The IFS125M spectrometer has been successfully operated on ships (Notholt et al., 2000).

In addition, several compact and medium to low-resolution instruments currently are under investigation, such as a grating spectrometer (about 0.16 cm⁻¹ resolution), a fiber Fabry-Perot interferometer (both setups presented in Kobayashi et al. (2010)), the IFS66TM from BrukerTM (0.11 cm⁻¹) (Petri et al., 2012), a Nicolet Spectrometer from Thermo-Scientific (0.125 cm⁻¹) (Chen et al. (2012)) and the IR-CubeTM from BrukerTM (0.5 cm⁻¹) (Jones et al. (2012)).

In this chapter, the suitability of a very compact setup, consisting of a modified commercial FTS with a resolution of 0.5 cm⁻¹ and a miniature solar tracker attached to it is demonstrated. The modifications applied to the commercial spectrometer are presented to achieve XCO₂ measurements with a precision 0.08 % over several months, validated with respect to a co-located TCCON spectrometer. This precision and long term stability was never achieved before by a similar compact spectrometer.

6.2 Instrumentation

The aim was to investigate the capabilities of a compact and robust spectrometer, which is sufficiently small and light to be carried by one person, without compromising the ability to align, modify and check internal optical components due to the compactness. In addition a small and transportable solar tracker was developed (see section 5.1.3 on page 91) which is directly attached to the spectrometer. This

merged setup is ready to use for various kinds of environmental research measurements. An image of the spectrometer is shown in figure 6.1.

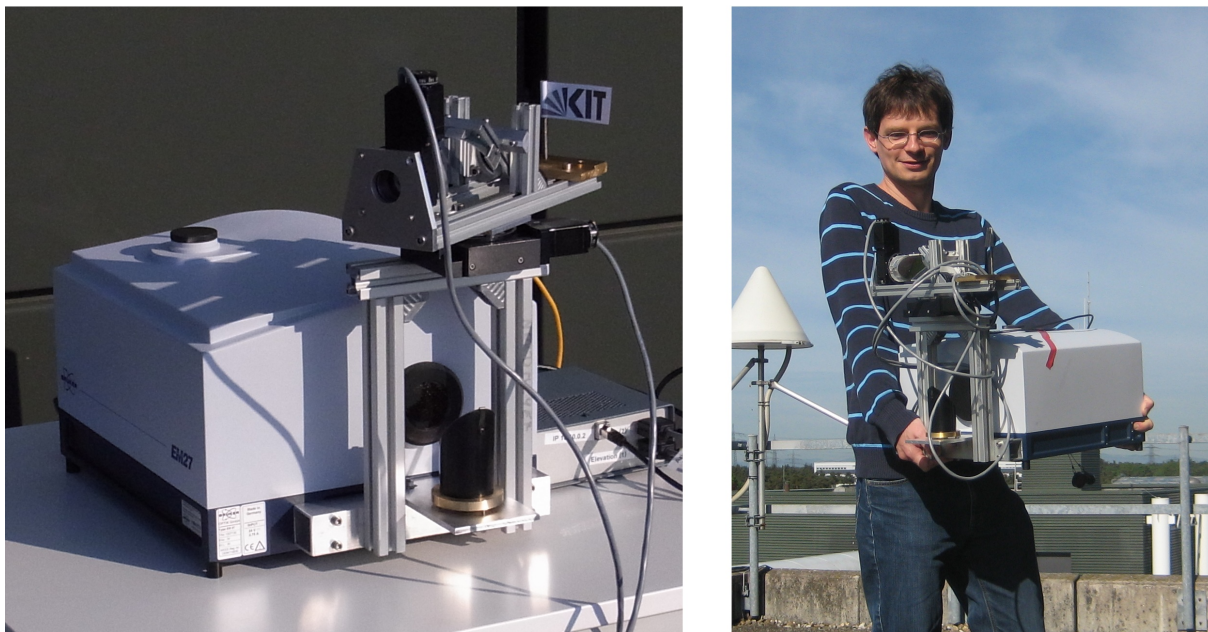


Figure 6.1: The EM27TM Spectrometer with the attached tracker. Right: transportation to the roof of the building where the measurements were made.

6.2.1 The NIR-modified EM27 spectrometer

For the investigations the EM27TM spectrometer from BrukerTM was used. This spectrometer uses the RockSolidTM pendulum interferometer with 2 cube corner mirrors and a CaF₂ beamsplitter, which offers very high stability with respect to thermal and mechanical disturbances. The interferometer supports a beam diameter of 40 mm. The pendulum is attached by springs, resulting in frictionless and wear-free movements. This principle results in even higher reliability of the interferometer in comparison to the 125HR setup. The latter suffers from wear due to use of friction bearings on the linearly moving retroreflector. This wear introduces a shear misalignment and requires regular realignment (Hase (2012)). The EM27 achieves 1.8 cm optical path difference equivalent to 0.5 cm⁻¹ resolution. To realize this, the retroreflectors of the pendulum structure move a geometric distance of 0.45 cm. The sampling of the interferogram is controlled by a standard, not frequency-stabilized HeNe laser. The sealed spectrometer compartment contains a desiccant cartridge; the radiation enters through a wedged fused silica window. So the spectrometer withstands and can be operated in adverse environmental conditions, e.g. high relative humidity. It measures approximately 35 × 40 × 27 cm and weighs 25 kg including the home-built miniature tracker, which was described in section 5.1.3. Due to the current electronics, with a resolution of 0.5 cm⁻¹, the spectrometer is capable of recording single-sided interferograms only, however, an electronics update will overcome this limitation in the future. It is compact enough to be carried by one

person, but still offers sufficient space inside for modifications and alignments of the light path, allowing us to test various setups.

A schematic drawing of the EM27 with modifications is presented in figure 6.2. The tracker, which was described in section 5.1.3, leads the solar radiation into the EM27 spectrometer. The beam is limited to 25 mm free diameter by using a 750 nm long-pass-filter a few centimeters behind the entrance window in order to block unwanted radiation which would disturb the laser detectors of the interferometer.

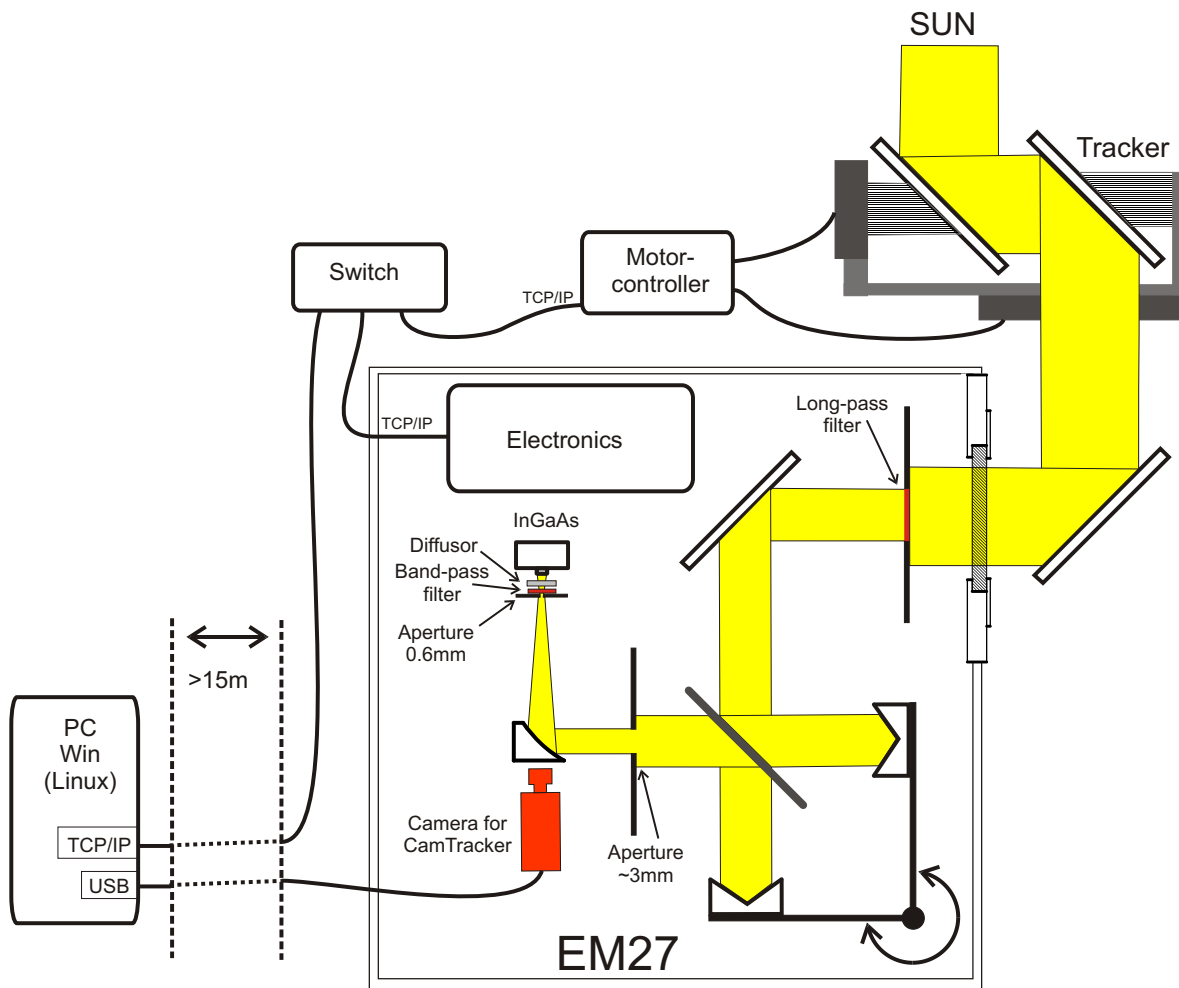


Figure 6.2: Schematic drawing of our measurement setup and the EM27 spectrometer. The camera is not in the same plane as the mirror, instead it observes the field stop by a small angle from above.

After the radiation has passed the interferometer, it is blocked by an aperture (which forms the aperture stop of the optical system) with a diameter of 3 mm. This aperture was inserted for controlling optical aberrations (to achieve a near-theoretical instrumental line shape, see section 6.3.1) and for avoiding nonlinear detector response. The remaining part of the radiation is appropriate for recording solar absorption spectra. Finally the beam is focused on a field stop with 0.6 mm diameter by a 90 degrees off-axis paraboloid with an effective focal length of 101.6 mm. In combination, this results in a semi

Field-of-View (FOV) of 2.96 mrad. This is half of the angle subtended by the FOV. The field stop is inclined versus the optical axis by a few degree to avoid channeling. As partially illuminated detectors show unwanted non-linear and ILS effects, a diffuser was placed between the field stop and the InGaAs detector (size $1 \times 1 \text{ mm}^2$, spectral sensitivity $6000\text{--}9000 \text{ cm}^{-1}$). The detector signal is DC coupled, allowing corrections for solar intensity variations due to thin clouds (Keppel-Aleks et al., 2007).

The image of the Sun on the field stop is recorded by the camera which then is used as the optical feedback for the tracker (CamTracker), as described in chapter 4. This is a very precise method for controlling the actual line of sight of the spectrometer. Changes of the alignment of any mirror, e.g. during transportation, have no effect on the accuracy of the tracking and the resulting line of sight. An image of the Sun on the aperture as it is recorded by the camera is shown in Fig. 6.3.

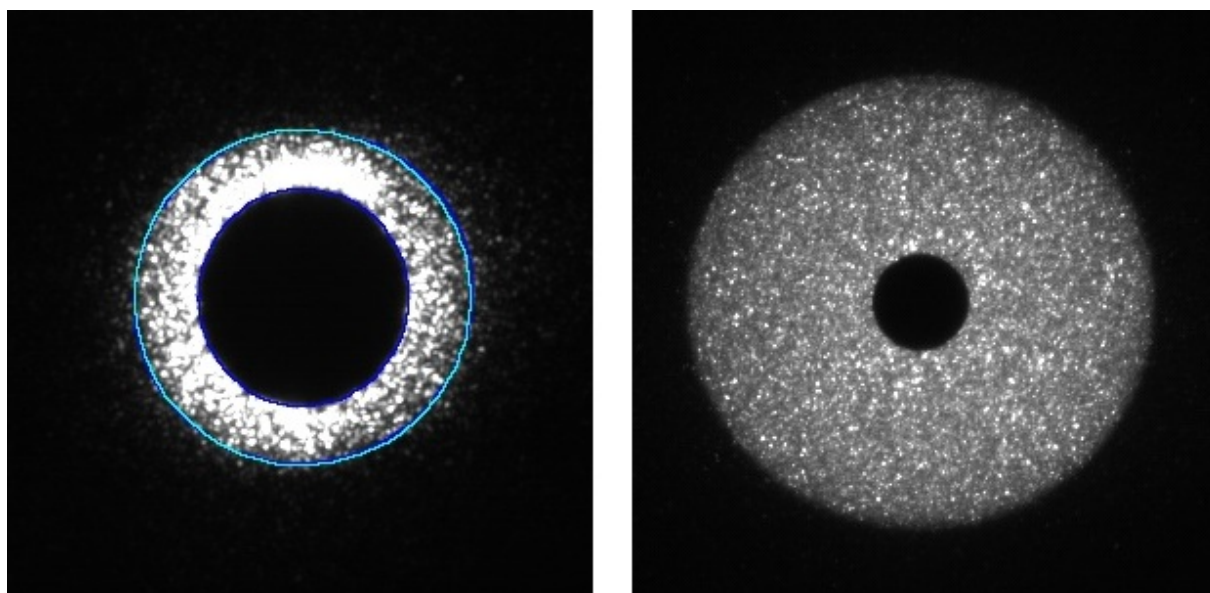


Figure 6.3: Images of the solar disk on the field stop of the EM27 spectrometer (left panel) and the IFS125HR in Karlsruhe (right panel) as recorded by CamTracker. The blue circles in the left image are the outlines, as they are detected and used by the CamTracker program for maintaining and correcting the precision of the tracking. The field-of-view differs between the EM27 and the IFS125HR.

The tracker and the EM27 interferometer are connected to a controlling computer via a standard network cable. The USB cable of the camera uses a separate outlet of the housing of the spectrometer and is connected with a 15 m active USB extension cable to the computer.

The controlling computer is equipped with an Intel 3.2 Ghz processor, runs Windows 7, the operating software for the spectrometer (Opus 7) and the CamTracker program. It was located one floor below the terrace on which the EM27 spectrometer was placed.

6.3 Characteristics

6.3.1 Instrumental line shape

Any quantitative trace gas retrieval depends on a proper knowledge of the spectral degradation characteristics. For FTIR spectrometers this instrumental line shape (ILS) is advantageously separated into one part which refers to the inherent self-apodization of an FTS with circular field stop, and therefore also exists for an ideally aligned spectrometer. This contribution can be calculated easily using the spectrometer's field-of-view and the optical path difference of the interferometer. The second component of the ILS can be described by a complex modulation efficiency (represented by a modulation amplitude and a phase error, both functions of optical path difference) which result from misalignments and optical aberrations. These parameters have to be derived by experiment, e.g. by evaluating gas cell measurements (Hase et al., 1999).

A standard approach for the high-resolution FTIR instruments is to use low-pressure gas cells. The ILS of the EM27 was checked by measuring the water vapor lines of about 2 meters in ambient air using a collimated standard halogen bulb as light source. This minimalistic approach makes a gas cell obsolete and can easily be performed, e.g. during measurement campaigns. To analyze these results and to obtain the modulation efficiency and the phase error, version 12 of the LINEFIT program (Hase et al., 1999) was used. The required parameters for the correct interpretation of the spectrum are the ambient temperature, the total pressure and the partial water pressure (the latter is a by-product of the LINEFIT analysis).

These measurements were performed 2 times within the time series presented in this chapter. On 8th of February 2012 and 22th of May 2012 the derived modulation efficiencies at maximum optical path difference were 0.9954 and 0.9910 respectively. However, as the used water vapor lines in HITRAN contain inaccuracies, the absolute value for the derived modulation efficiency and the phase error depend on the selected spectral range. Therefore it can only be concluded that the ILS of the EM27 is impressively stable, but the absolute calibration of the modulation efficiency requires further study of the H₂O line parameters in the 7000 cm⁻¹ spectral region.

For the tested system, with a spectral resolution of 0.5 cm⁻¹ an increase of 1 % of the modulation efficiency results in an XCO₂ increase of 0.15 %. As in the time series the assumed modulation efficiency changed by less than 0.5 %, a constant ideal ILS was used in the retrievals. Note that no realignment of the spectrometer was performed over the whole period, although the spectrometer was transported frequently and was exposed to temperatures between -10 and 40 °C. The knowledge of the absolute modulation efficiency was estimated to be within 2 %, which implies that the systematic offset between the EM27 and 125HR XCO₂ timeseries should be below 0.3 %.

6.3.2 Ghost to parent ratio

For the recording of NIR spectra in the 6000 to 9000 cm^{-1} range, the IFG sampling has to be performed at each rising and falling zero crossing of the laser AC signal. This makes the IFG recording prone to alternating sampling errors, which generates artifacts (ghosts) in spectral domain, as described in section 3.6 and by (Messerschmidt et al., 2010). As this problem affected several TCCON measurement sites in the past, the GPR (ghost-to-parent ratio) for the setup was checked.

In contrast to the IFS125HR spectrometers, it is not possible to readjust the GPR with the currently available EM27 electronics. The laser-detecting photo diodes, however, are the same as used in the latest 125HR version.

With the used EM27 spectrometer a GPR of $2 \cdot 10^{-4}$ was measured, which is of the order of the current TCCON recommendations ($1 \cdot 10^{-4}$). F. Hase recently suggested an IFG resampling scheme which has been successfully applied for correcting interferograms collected by different TCCON spectrometers (see sec. 3.6). For the EM27, we refrained from performing any correction because the GPR is rather small.

6.4 Measurements and analysis

6.4.1 Setup and operation of the spectrometers: EM27 and reference TCCON spectrometer

The EM27 spectrometer was operated on the roof terrace of the IMK office building at 133 meters above sea level with the coordinates 49.094° North and 8.4336° East. The testing period covered 26 measurement days from 3th of February 2012 to 22th of June 2012. For each day of operation, the spectrometer was moved from its storage place in the fourth floor to the terrace on floor 7, see Fig. 6.1. As a simple unsprung trolley was used for transportation, the spectrometer was subject to significant mechanical vibrations. When placing the spectrometer outside, not much effort was put into a precise leveling or orientation. A coarse orientation relative to the wall of the building was sufficient to enable the CamTracker program to detect the Sun on the field plane and to center it to the field stop (see Fig. 6.3). During operation, the spectrometer experienced outside ambient conditions. Temperatures in February were as low as -10°C , in May the spectrometer was heated to temperatures above 40°C due to exposure to direct sunlight. The standard measurement procedure was to alternately recorded single-sided interferograms with 0.5 cm^{-1} and double-sided interferograms with 1 cm^{-1} resolution, with 10 averages each. The recording time for each of these measurements (being an average of 10 IFGs) was about 34 seconds. The applied scanner speed was 10 kHz. For the further analysis in this work, only the 0.5 cm^{-1} resolution measurements were evaluated, because a significant loss in contrast between the CO_2 lines and the adjacent continuum is observed when the resolution is reduced to 1.0 cm^{-1} , as can be seen in Fig. 6.4. We chose the alternately 0.5 cm^{-1} and 1 cm^{-1} recording scheme, to maintain the option for evaluating

the spectrometer's capabilities with 1 cm^{-1} resolution, and to check for differences in the single-sided and double-sided recording scheme. However, as we only evaluated the 0.5 cm^{-1} resolution spectra, the effective duty-cycle of the EM27 is only 50%.

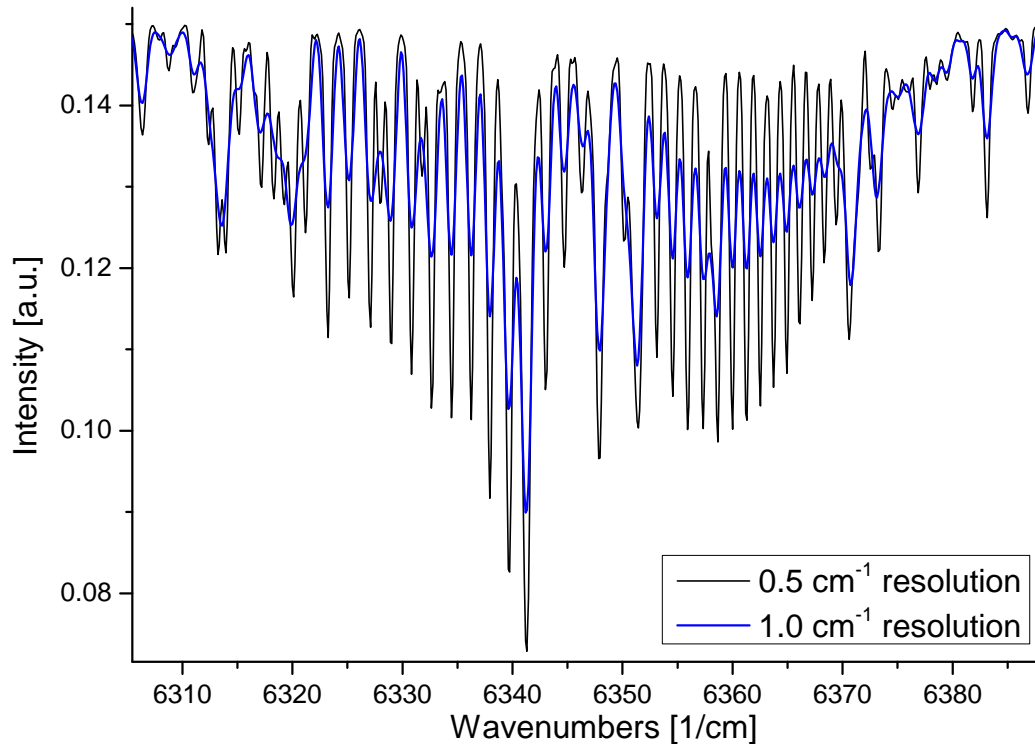


Figure 6.4: A section of the CO₂ retrieval window with 0.5 and 1 cm^{-1} resolution. A Norton-Beer apodization function was applied to the interferogram to suppress sidelobes next to each spectral line, which is an artifact in low-resolution FTIR spectra.

The TCCON instrument in Karlsruhe located about 700 meters north of the IMK office building provided the reference XCO₂ dataset. During each of the 26 EM27 measurement days, 125HR spectra were recorded in parallel.

In addition, various meteorological observations are available at the site. the records of ground pressure and tall tower temperatures at 100 and 200 meter altitude are of relevance. These auxiliary data have been used for the analysis of the spectra (see section 6.4.2). The ground pressure sensor is a BM35–barometer from meteolaborTM with a stated accuracy of $\pm 0.05\text{ hPa}$. The temperature is acquired from a PT100 sensor (Type 2015) from the company “Theodor Friedrichs & Co”. It’s accuracy is stated as $0.1^\circ\text{C} + 0.005 \cdot T$, with T in degrees Celsius.

6.4.2 Data processing and evaluation

The official analysis code for the TCCON network is GFIT, as described in section 2.2.2 (see also Wunch et al. (2011)). However, the calibration procedures and the retrieval codes (PROFFIT Version 9.6) developed at the ground-based FTIR group at the IMK was used in this study. This setup is well established for work within the NDACC FTIR network and has been validated in various studies (Schneider et al. (2008), Schneider et al. (2010) and Sepúlveda et al. (2012)). Therefore, first it will be shown that the setup well reproduces the official TCCON 125HR XCO₂ results for the high-resolution 125HR spectra, where the 2012 software release including the April update was used. Next the EM27 spectra and resolution-reduced 125HR spectra are analyzed with the IMK-internal retrieval setup. The resolution-reduced 125HR spectra have been included to discern instrumental effects from apparent XCO₂ changes when analyzing low-resolution spectra.

The same O₂ line list and the same CO₂ and H₂O a-priori mixing-ratio profiles were used, as applied in the “official” TCCON analysis. For CO₂ the HITRAN08 lines were used with line-mixing parameters derived from F. Hase, from a code provided by J.-M. Hartmann (Lamouroux et al., 2010).

The pressure and temperature profiles for all PROFFIT evaluations were taken from local meteorological measurements (ground pressure and tall-tower temperatures at 100 and 200 m altitudes) and from the Merra⁴ model (see Sec. 3.7). For each of these times, the solar position is calculated and the pressure and temperature values along the unrefracted path of the solar radiation are retrieved from the model data. These profiles are then used as an input for the PROFFIT retrieval. The profile which is used for the evaluation of a spectrum recorded at a specific time is calculated by PROFFIT by applying a linear interpolation between two temporally adjacent profiles. Further details are described in section 3.7.

No post-processing of the XCO₂ results has been performed within the analysis sequence apart from applying the TCCON calibration factor of 0.989 (Wunch et al., 2010) to all XCO₂ results. In accordance with previous studies (Petri et al., 2012) it was found, that reducing the spectral resolution significantly below the resolution applied by the TCCON network leads to a systematic increase of the retrieved O₂ and CO₂ columns. The study by Petri et al. was performed using GFIT. Similar - but not identical - changes can be observed with the independent analysis setup using PROFFIT. Therefore it can be assumed, that this effect is partly introduced by deficiencies of the far-wing line shape model and partly stems from approximations of the line-by-line calculation of absorption cross-sections. As long as the reasons are unclear, this systematic offset can be removed by adjusting the XCO₂ calibration factor for a hypothetical EM27 network.

The data was processed and evaluated in 4 different ways which will later be denoted as “EM27”, “HR_High”, “HR_Reduced” and “GFIT”:

EM27: PROFFIT-evaluated averages 10 IFG of EM27 with 0.5 wavenumber resolution. The IFGs were apodized by a Norton-Beer-Medium function.

⁴<http://disc.sci.gsfc.nasa.gov/daac-bin/DataHoldings.pl>

HR_High: PROFFIT-evaluated averages of 4 IFGs (2 forward, 2 backward) from TCCON-instrument with 0.014 wavenumber resolution.

HR_Reduced: The initial measurements are the same as in “HR_High”, but the interferograms were truncated to 0.5 cm⁻¹ resolution and apodized by a Norton-Beer-Medium function. The retrieval scheme then was the same as described in “EM27”.

GFIT: GFIT-evaluated averages of 2 forward or 2 backward interferograms of the TCCON instrument with 0.014 cm⁻¹ resolution (forward and backward interferograms are analyzed separately). For the time series intercomparison in Sect. 6.5.3, these separate forward- and backward results are averaged, in contrast to the figures containing the gas columns and the XCO₂ values in the course of measurement days. In any presented data, the IFG preprocessing routines from GGG were applied (correction of solar intensity variations and determination of the phase spectrum used for the FFT), as described in Wunch et al. (2011). For the calculation of XCO₂ values the standard GFIT postprocessing routines were applied. These include an averaging of the 2 CO₂ column values as two separate spectral windows are evaluated (see Sec. 6.4.3). In this averaging, a multiplicative bias between the 2 spectral windows is corrected for, which is determined from the whole available dataset. In the next step, the XCO₂ values are calculated according to eqn. 3.3 and an empirical airmass-dependent correction factor is applied. Further details can be found in (Wunch et al., 2011) and on the TCCON wiki webpage <https://tcccon-wiki.caltech.edu>.

The “EM27” and “HR_Reduced” low resolution spectra were generated from the interferograms after applying the Norton-Beer-Medium function. In low-resolution spectra, omitting the numerical apodization would introduce significant sidelobes around all spectral lines. As these fade away slowly, modeling of these artifacts would complicate the calculation of the model spectra considerably. The Norton-Beer-Medium apodization is a good compromise between sufficiently effective suppression of sidelobes and degradation of spectral resolution.

6.4.3 Spectral windows

In the “official” TCCON analysis, the CO₂ column is evaluated in the spectral ranges 6180-6260 and 6297-6382 cm⁻¹, for the O₂ analysis the range 7765-8005 cm⁻¹ is applied. For the PROFFIT analysis of the 125HR and EM27 spectra, the same O₂ window was adopted, however the CO₂ windows were merged into one broader region extending from 6173 to 6390 cm⁻¹.

An example of the spectral windows including the measurement, the fit and the residual is presented in Fig. 6.5. For both windows the quality is very good and the standard deviation of the residual is $1\sigma = 0.2\%$ for CO₂ and 0.17% for O₂. However, several peaks appear in the EM27 residuals (in the graph of the O₂ marked with arrows) which do not appear in the resolution-reduced 125HR spectra.

These residuals originate from the fact that the intensity and shape of the solar lines vary as function of the projected solar disc radius (Hase et al., 2006). Because the FOV of the EM27 instrument of 2.95 mrad

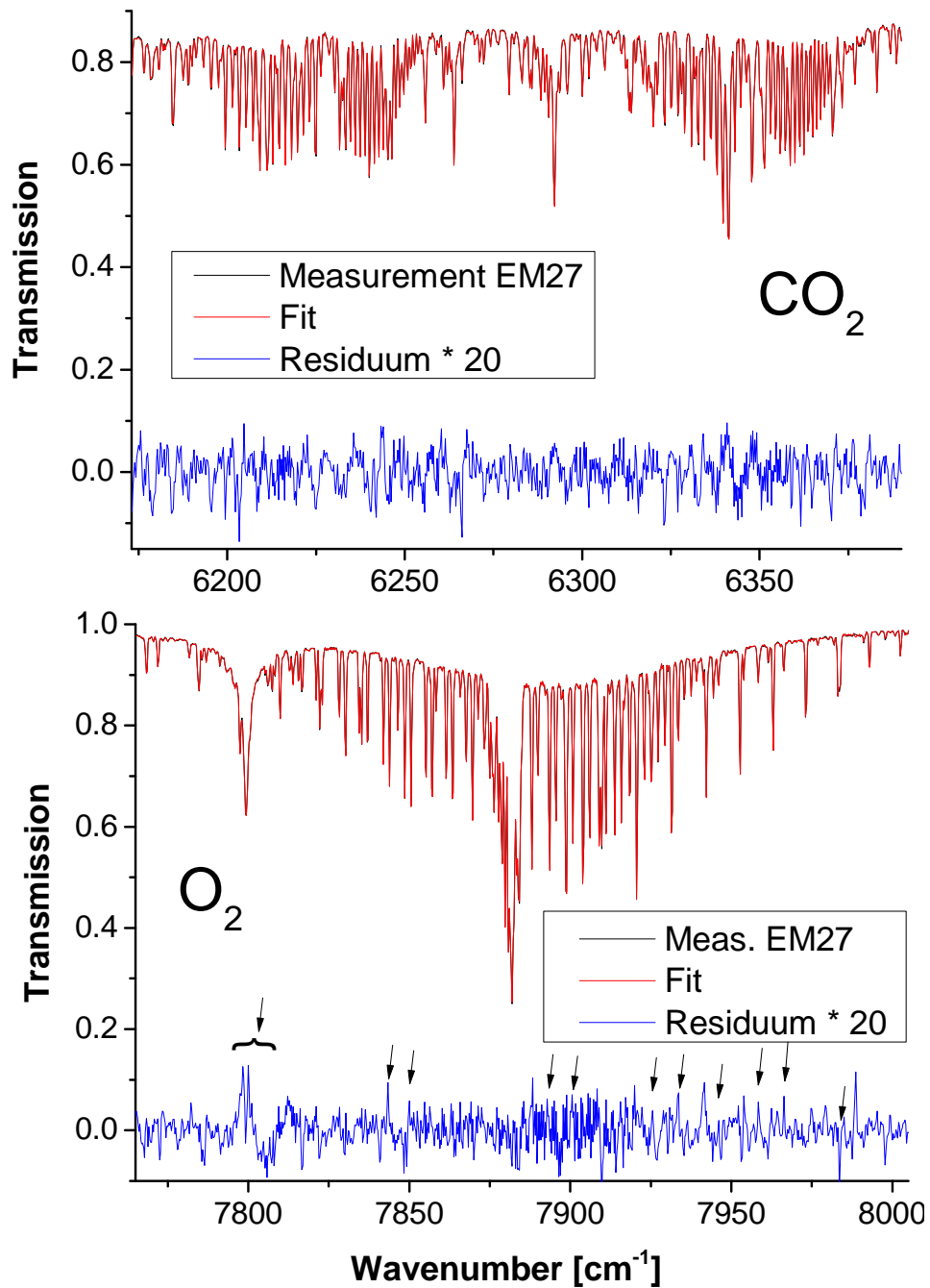


Figure 6.5: Spectral windows used by PROFFIT to derive the CO₂ and O₂ columns. In the lower figure the systematically occurring residuals due to deficiencies of the solar line modeling are marked in the residual.

(semi-FOV) is a factor of about 3 greater compared to the one of the IFS125HR, which has a semi-FOV of 0.957 mrad, the EM27 observes a significantly larger fraction of the solar disc. An image of the solar disc superimposed on the field stop as recorded by the CamTracker is displayed in Fig. 6.3. The current NIR line list used by PROFFIT does not include parameters to describe the center-to-limb variability of the solar lines.

6.5 Results

In this section, the results for the EM27 are evaluated, in comparison to the 125HR reference. In sections 6.5.1 and 6.5.2 an overview of the CO₂ and O₂ columns and the resulting intraday variability of XCO₂ during several sample days are provided. In section 6.5.3, a statistical analysis for the whole set of measurements is presented.

6.5.1 CO₂ and O₂-columns

Figures 6.6 and 6.7 show the CO₂ and O₂ columns for the measurement days 21th of February 2012 and 28th of March 2012. In each graph, the ambient air temperature on the terrace is given for the beginning and the end of the EM27 measurements. In addition, the starting, the minimal and the last value for the solar zenith angle (SZA) of the measurements are displayed. The values in the areas with a gray background are not taken into account in the statistical analysis of section 6.5.3. The shaded areas filter out SZAs beyond 70 degrees and measurements taken within the first 30 minutes after the start of measurements. The latter restriction was added as the EM27 requires some startup time before operating in a stable manner. After moving it from the 20 °C lab environment to the outside temperature on the terrace, which was sometimes as low as -12 °C, the HeNe reference laser tube temporarily undergoes fast temperature changes, thereby shifting the reference wavelength during a few scans.

Columns for O₂ recorded on 2 days are presented in Fig. 6.6. The data processing procedure for the 4 types of datapoints were described in section 6.4. One observes a difference between the “HR_High” and the “HR_Reduced” columns, resulting from the reduction of the resolution. The “HR_Reduced” columns of O₂ are 0.4 % higher than the reference values. This systematic resolution-depending difference was also observed before by Petri et al. (2012). A closer inspection reveals that this is not a constant correction factor in case of the CO₂ column, but also a weaker airmass-dependent contribution can be observed. The “HR_Reduced” CO₂ columns are 0.4 to 0.6 % higher than the reference values. This finding is not surprising for an effect probably induced by line shape issues. Nevertheless, this is not an obstacle for a hypothetical EM27 network, but a matter of adjusting the analysis procedures, as the TCCON network also performs some air mass dependent tuning in the course of the analysis of the 125HR spectra.

One would expect the EM27 O₂ and CO₂ columns to reproduce the “HR_Reduced” values. However, despite using the same retrieval parameters, values approximately 0.6 % lower were observed. The origin of this offset is not clear yet, as the retrieval scheme (a-prioris, pressure and temperature profiles, used

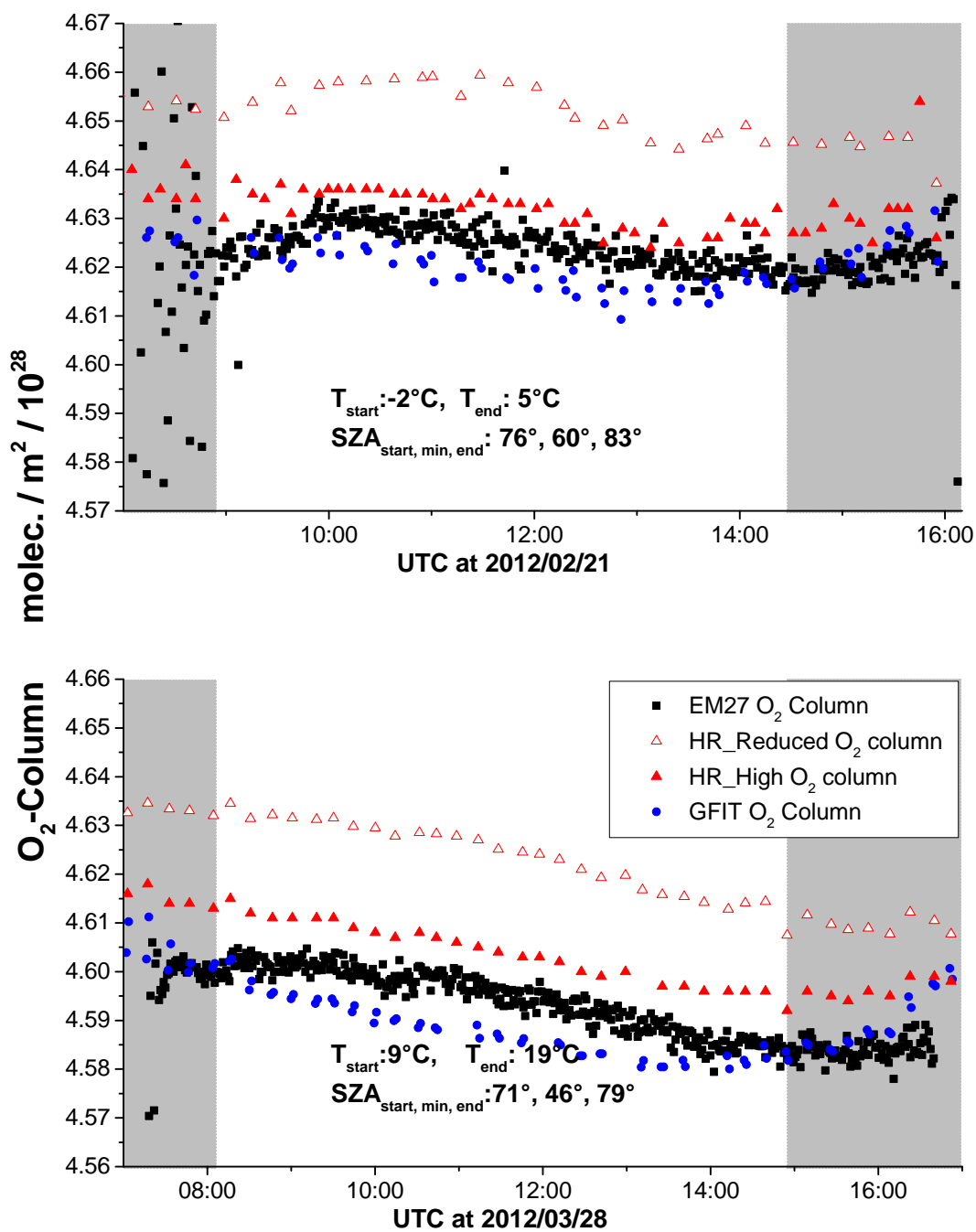


Figure 6.6: O₂ columns for the four datasets for two sample days. The observed intraday variability is very low. The number of interferograms and respective recording interval contained in a single datapoint of each type are the following: EM27: 10 IFGs, 34 s; HR_Reduced: 4 IFGs, 34 s; HR_High: 4 IFGs, 212 s; GFIT: 2 IFGs, 106 s.

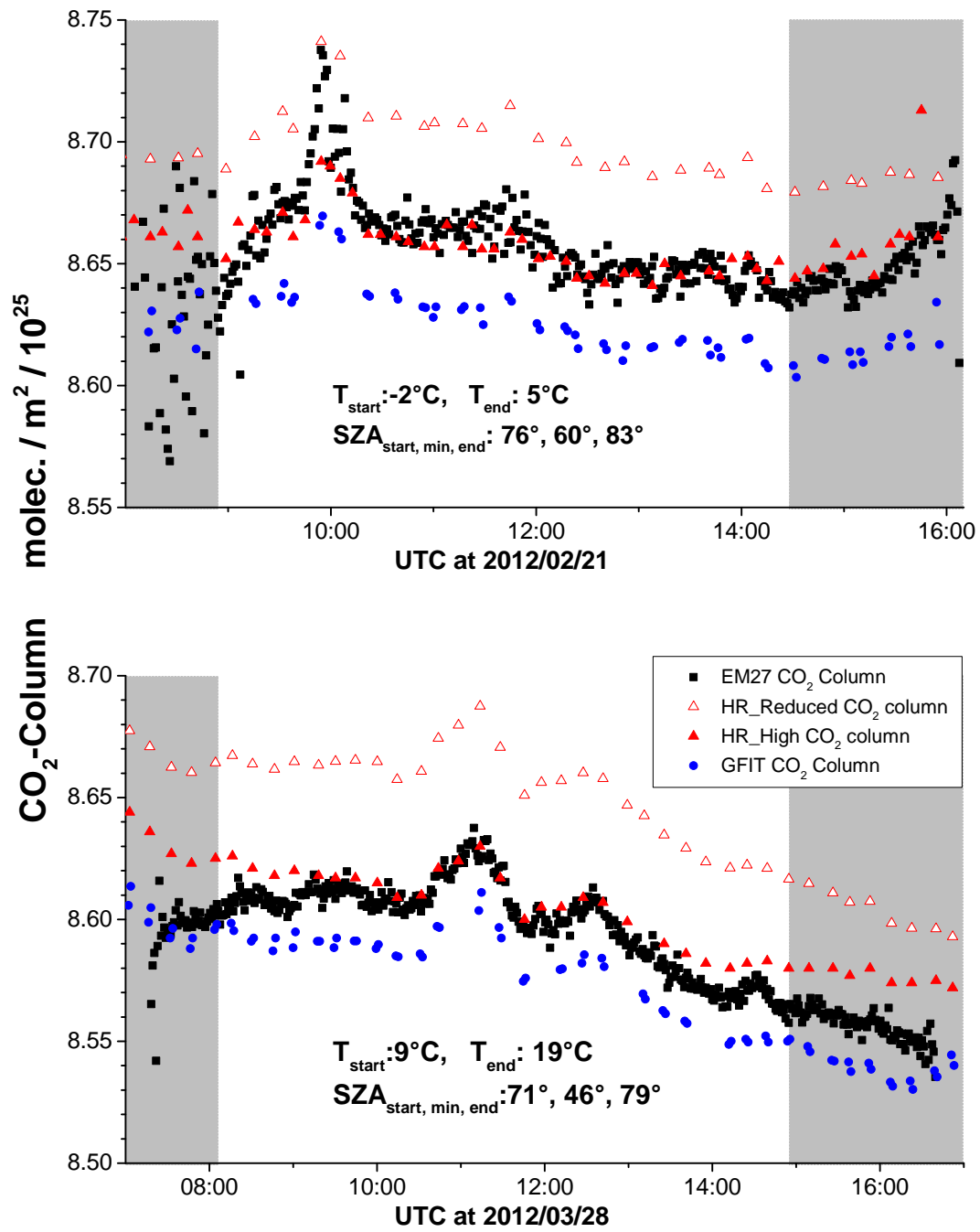


Figure 6.7: CO₂ columns for 2 days. The systematic offsets of the 4 datasets is very similar to those in the O₂ columns. The number of interferograms and respective recording interval contained in a single data-point of each type are the same than in Fig. 6.6

resolution,...) is exactly the same. As outlined in section 6.3.1 the absolute ILS calibration of the EM27 might be slightly off, and the observed discrepancies are within the resulting error bar (moreover, the offset is nearly the same for CO₂ and O₂ columns as one would expect in this scenario). Therefore, it can be assumed, that the uncertainty of the ILS calibration is the leading effect. In addition, the deficiencies of the solar line model could trigger parts of the systematic offsets. A third possible reason for this discrepancy could be an inhomogeneously illuminated field stop. As the solar intensity decreases towards to the rim and the FOV of the current EM27 setup includes a large section of the sun (see. Fig. 6.3), impacts on the trace gas retrieval are possible.

The variation in the EM27 O₂ columns during the evaluated days is very low which proves the high stability of the EM27 spectrometer as well as the high performance of the CamTracker system. When comparing the “GFIT” and “HR_High” results generated with PROFFIT, one observes an air mass dependent increase of the GFIT values. For this reason the TCCON applies an a posteriori airmass correction to the XCO₂ values. For the PROFFIT evaluated O₂ columns this effect is not evident, although the same line lists are used.

When compared to the intraday variability of the O₂ columns, the higher variability of the CO₂ columns is obvious. These enhancements are indicated by both the EM27 and the 125HR and are discussed in section 6.5.3.

6.5.2 XCO₂

The XCO₂ values for 5 sample days are presented in Fig. 6.8. As described in section 6.4.2, all datasets are calculated by equation 3.3 and include the WMO calibration factor of 0.989. In addition, the GFIT(TCCON) dataset contains a GFIT-specific post-correction, especially an air mass dependent correction.

Obviously the systematic differences between the 4 datasets cancel out very well so that they agree within about 1ppm. The intra day variability differs strongly between the measurement days. During some days the values vary very smoothly (e.g. 22th of March 2012), others, such as the 28th of March 2012, show several short-term increases. As these are observed both by the EM27 and the 125HR and the simultaneously recorded CamTracker images look unsuspectingly, these enhancements reflect real increases in the atmospheric XCO₂. The measurement site is located in an urban area; it is surrounded by several coal- and gas power plants. The closest ones are in the town Karlsruhe (13 km to the southwest with 915 MW), in Mannheim (39 km to the North with 1675MW) and in Heilbronn (57 km to the East with 950 WM). On 28th of March the wind came from the North, so the CO₂ increases can be suggested to originate from the power plant in the city of Mannheim.

A slight air mass dependent difference is visible between the 4 datasets. It is nearly negligible between the 2 low-resolution datasets and biggest between the “EM27” and the “HR_High”. However, it is worth

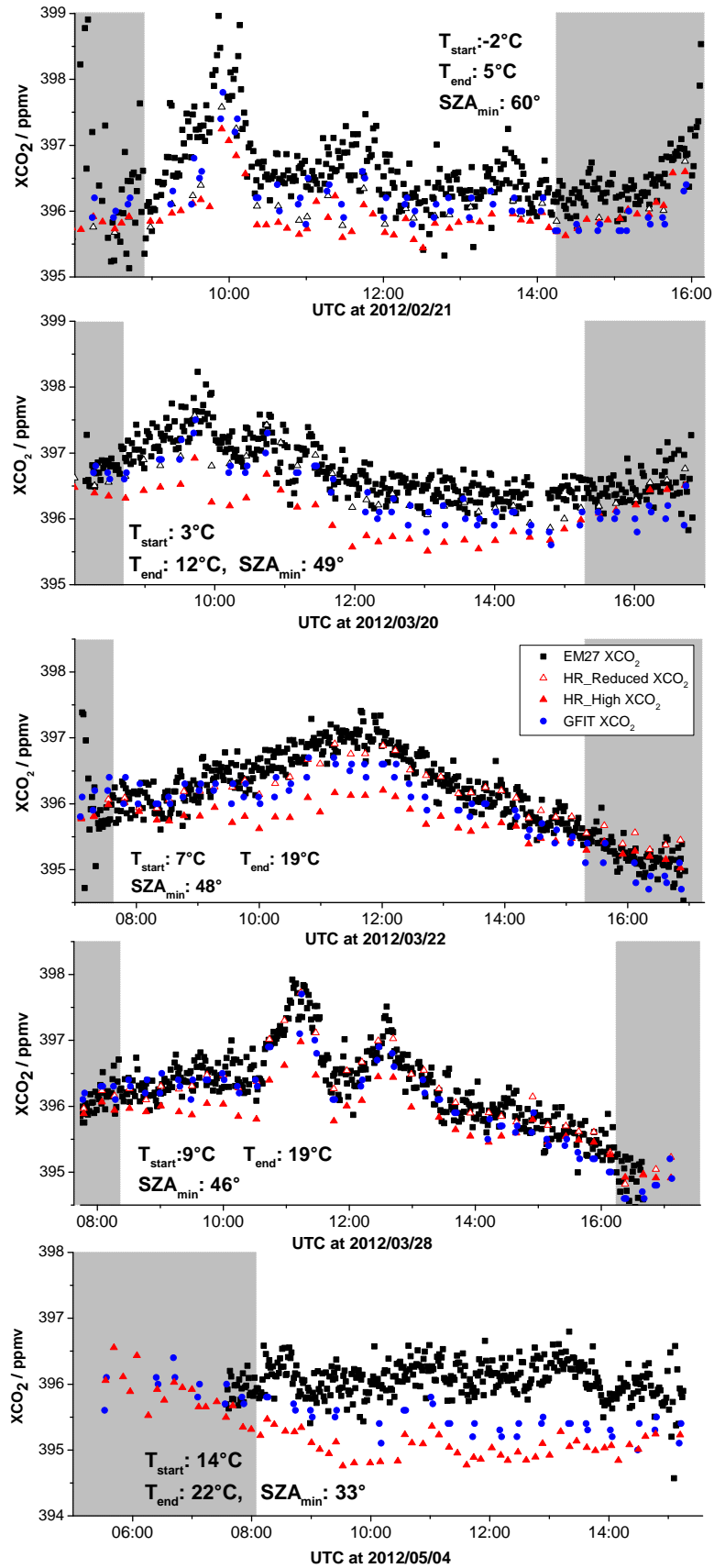


Figure 6.8: Measurements of retrieved XCO₂ at 5 sample days.

to mention that these effects are below 0.25 % and could essentially be shifted by an airmass-dependent post-correction as long as the reasons are not fully understood,.

6.5.3 Comparisons

To compare the XCO_2 -results over the whole time series of 26 measurement days between February and May 2012, the daily means were calculated, which is shown in Fig. 6.9.

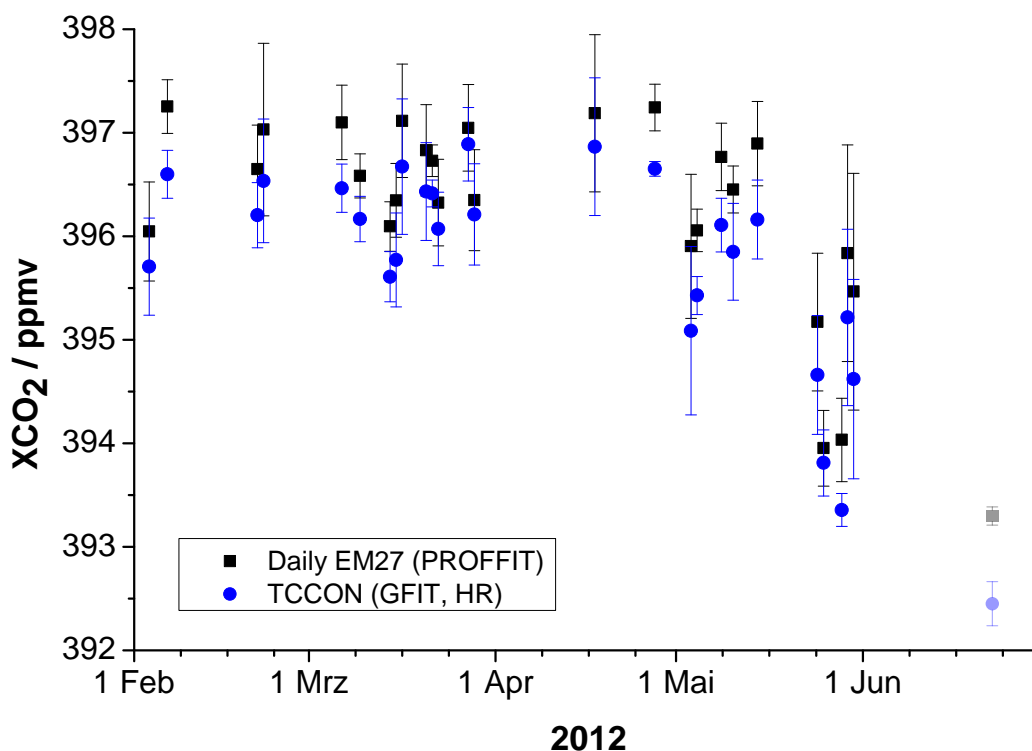


Figure 6.9: Daily means of XCO_2 values of the EM27 and the TCCON instrument. The last day is preliminary only, as the Merra meteorological model data were not yet available at the time this analysis was performed.

As the $1-\sigma$ error bars for the daily mean values mainly result from the intra day variabilities, a more significant comparison can be done by calculating the differences between the “EM27” values and the three other data types “GFIT”, “HR_High” and “HR_Reduced” (see 6.4.2). To reduce temporal variabilities, only data were taken into account, which were recorded at nearly the same time. In addition, as described above, only measurements were taken into account which had a corresponding SZA lower than 70° and were taken at least 30 minutes after the set up of the instrument on the terrace. For one datapoint taken with the HR instrument (duration 212 s, containing 2 forward and 2 backward IFGs), the data of 3 EM27 spectra (total duration 102 s; each spectrum containing 10 IFGs) were averaged and used.

Following this procedure, the XCO_2 and the total O_2 column values are investigated in the following. The O_2 column values offer the advantage that there is no significant variability on short time scales which could superimpose the instrumental effects under investigation.

As we alternately recorded 0.5 cm⁻¹ and 1 cm⁻¹ spectra as described in Sec. 6.4.1, these 3 EM27 0.5 cm⁻¹ measurements span about the same time period as the measurement time of an HR datapoint (average of 2 forward and 2 backward IFGs).

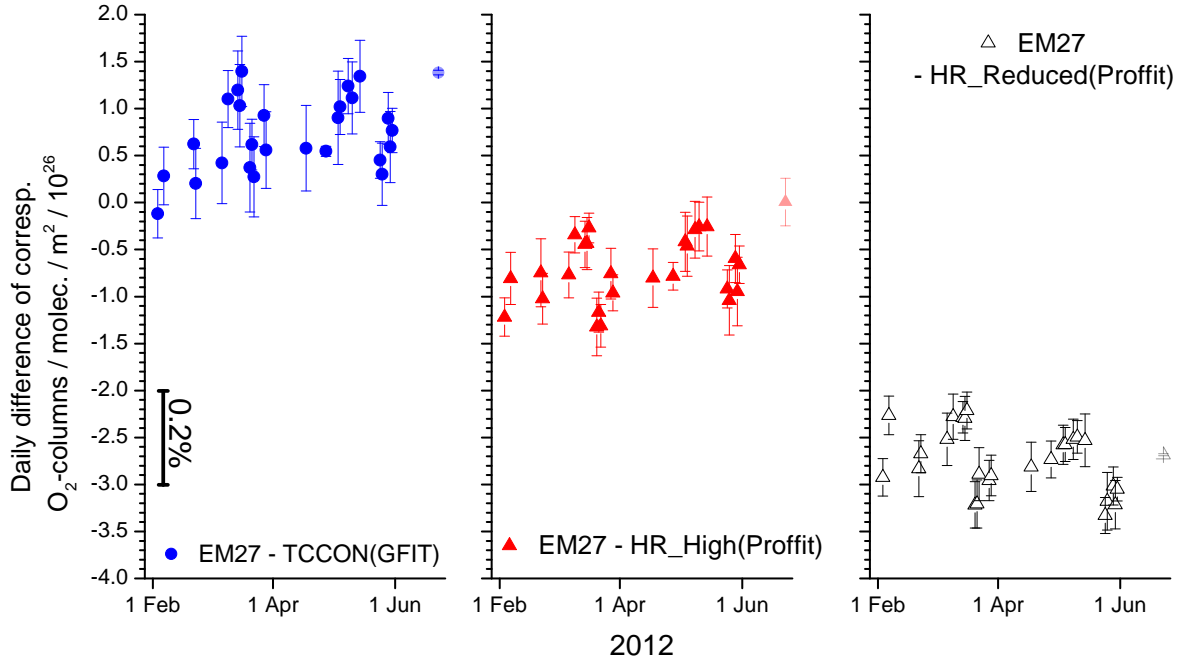


Figure 6.10: Differences between the EM27 O₂ total columns and the 3 other datasets, where the daily means of the differences with the according 1- σ error bars are shown. To obtain the differences, only IFGs were taken into account, which were recorded at the same time. The last day is preliminary only and not taken into account in the statistical evaluation.

In Fig. 6.10 the statistical behavior of the O₂ column differences for each measurement day are collected. The mean difference, and the 1- σ error bar according to the intraday scatter is shown. These daily means are made only for graphical reasons and not for the following statistical values. For all simultaneously measured results in the whole time series, the differences in the O₂ columns have the following values:

$$\begin{aligned} \text{EM27-GFIT:} & \quad (7 \pm 5) \cdot 10^{25} \text{ molec/m}^2 \\ & \quad \hat{=} (0.15 \pm 0.11)\% \end{aligned}$$

$$\begin{aligned} \text{EM27-HR_High:} & \quad (-7 \pm 4) \cdot 10^{25} \text{ molec/m}^2 \\ & \quad \hat{=} (-0.15 \pm 0.09)\% \end{aligned}$$

$$\begin{aligned} \text{EM27-HR_Reduced:} & \quad (-27 \pm 4) \cdot 10^{25} \text{ molec/m}^2 \\ & \quad \hat{=} (-0.59 \pm 0.09)\% \end{aligned}$$

The mean differences show significant offsets, as already discussed in section 6.5.1. However, they compensate for the largest part when calculating the XCO₂. The scatter around the mean systematic

offset, the precision, is impressively good with values around 0.1%, proving the high stability of the EM27 instrument.

When moving on to the XCO_2 , one obtains results as shown in Fig. 6.11 and the following statistical values:

$$\begin{aligned} \text{EM27-GFIT:} & \quad (0.46 \pm 0.32) \text{ ppm} \\ & \quad \hat{=} (0.12 \pm 0.08) \% \end{aligned}$$

$$\begin{aligned} \text{EM27-HR_High:} & \quad (0.81 \pm 0.36) \text{ ppm} \\ & \quad \hat{=} (0.20 \pm 0.09) \% \end{aligned}$$

$$\begin{aligned} \text{EM27-HR_Reduced:} & \quad (0.26 \pm 0.29) \text{ ppm} \\ & \quad \hat{=} (0.07 \pm 0.07) \% \end{aligned}$$

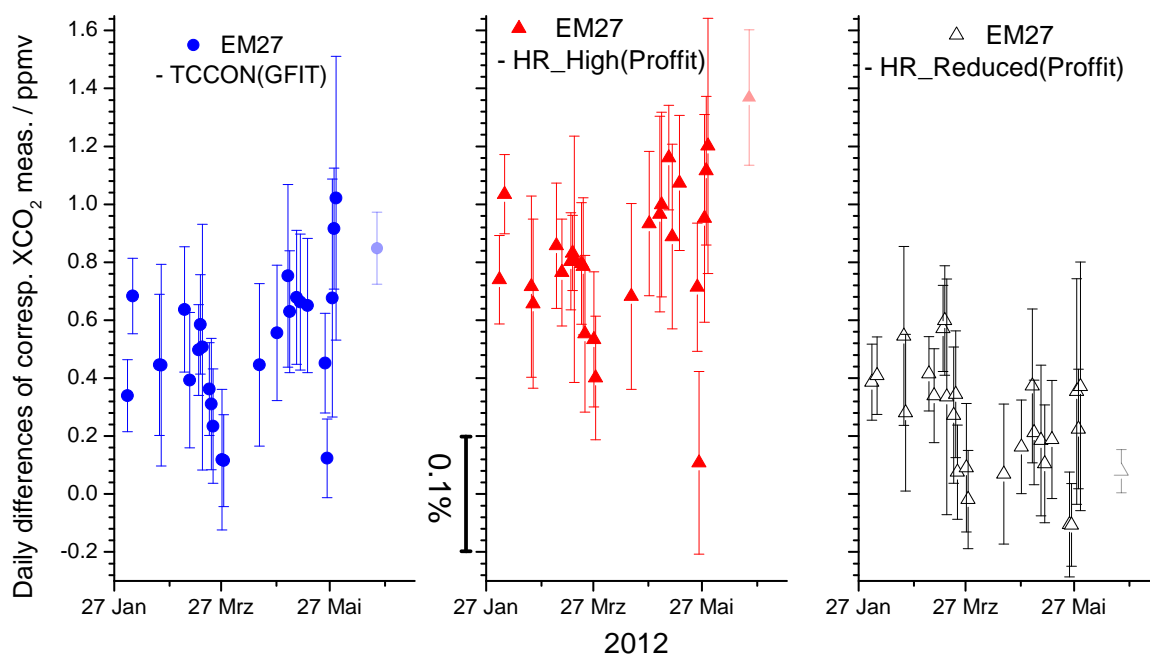


Figure 6.11: XCO_2 values with the same data processing as for the O_2 columns in Fig. 6.10 for the 26 measurement days.

These values show a very good accuracy of better than 0.2% relative to a high-resolution instrument. As long as the underlying causes are unknown, this offset most probably can be absorbed by a global scaling factor for a hypothetical EM27 network (and an air-mass-dependent correction term for reaching even higher accuracies), similar to the WMO factor which is applied to the TCCON XCO_2 values, presuming the low resolution instruments are all identical in construction. The scattering between the EM27 and the high-resolution data is lower than 0.09%, well inside the range of the stated precision of the TCCON network which is 0.25% (Wunch et al., 2011).

6.5.4 XCO₂-Signal to noise

To approximately compare the Signal-to-Noise of the XCO₂-values, a running average was applied to the EM27 and GFIT(TCCON) values of a few days (see Fig. 6.12 for 22th of March 2012) and the scatter of the data was calculated. The GFIT values show a standard deviation of 0.085 ppm for a recording time of 212 seconds (average of 2 forward and 2 backward scans). The EM27 values which had a recording time of 34 seconds per datapoint (which includes 10 scans) have 1 σ standard deviation of 0.17 ppm. For a TCCON-equivalent acquisition time of 212 seconds this value lies at approximately $0.17 \text{ ppm} \cdot \sqrt{34s/212s} = 0.07 \text{ ppm}$, which is comparable to the GFIT(TCCON) value.

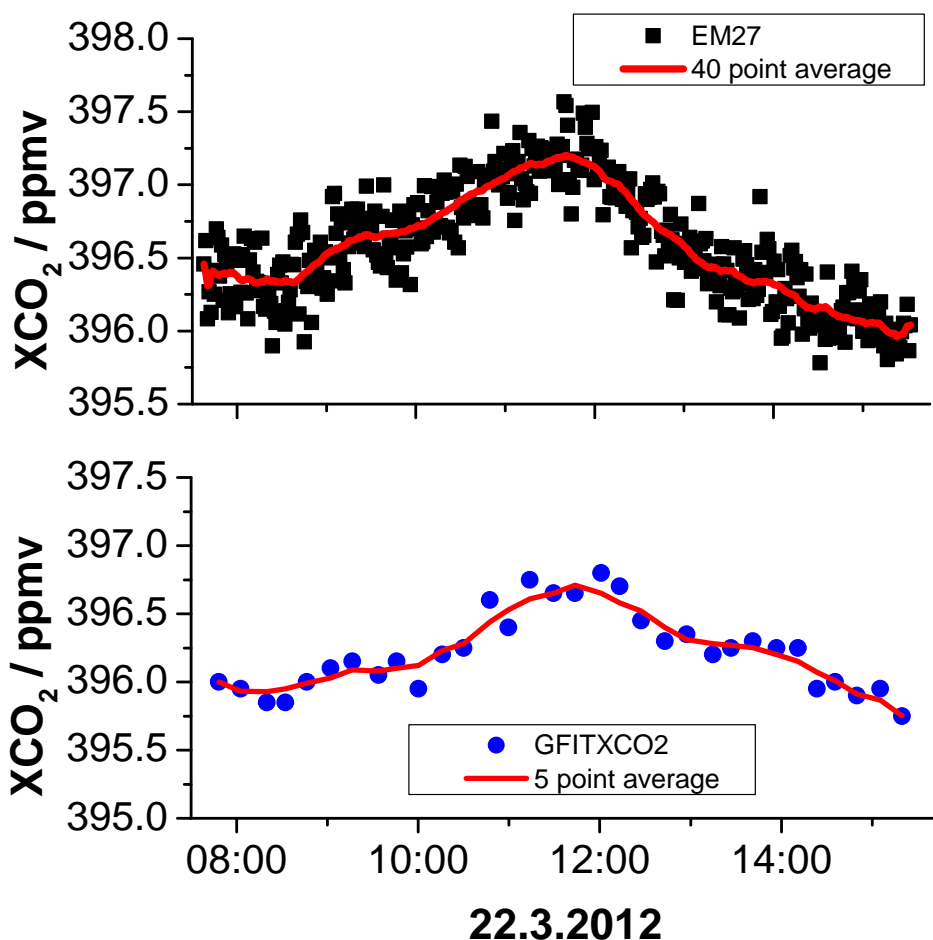


Figure 6.12: Sample day to derive the XCO₂ noise of the EM27 and GFIT(TCCON) values. When taking into account the different recording durations, the noise level is comparable. The number of interferograms and respective recording time contained in a single EM27 datapoint are 10 IFGs and 34 s, for a single GFIT datapoint 4 IFGs and 212 s.

On first sight this is surprising when having in mind the very small parallel beam diameter of 3 mm of the EM27. In total the intensity on the EM27 detector is a factor of about 150 smaller than on the HR detector. However, the photon noise part of the Signal-to-Noise Ratio (SNR) of a FTIR spectrum also

is dependent on the resolution, or more precisely the number N of datapoints in the interferogram. This factor of $\sqrt{2/N}$ leads to a comparable SNR of the low-resolution measurements.

6.6 Conclusions of the low-resolution XCO₂ measurements

The presented intercomparison demonstrates the applicability of a well-characterized low-resolution FTS spectrometer for XCO₂ measurements. The precision of the EM27 values found in this investigation is well inside the current network-wide TCCON accuracy of 0.25 %. The differences of temporally coinciding measurements for the retrieved XCO₂ were $(0.12 \pm 0.08)\%$ and $(0.20 \pm 0.09)\%$ when compared to high-resolution TCCON spectra, analyzed with the official GFIT and PROFFIT algorithms, respectively. The optical stability and the low influence of varying outside temperatures ($-10\text{ }^{\circ}\text{C}$ to more than $40\text{ }^{\circ}\text{C}$) are promising features of the EM27 spectrometer, so this study proves its high applicability especially for operation at remote sites and measurement campaigns.

Therefore, the EM27, with the modifications presented in this paper, seems a very promising candidate for an instrument supporting the core TCCON stations for increasing the global representativeness of greenhouse gas measurements by the operation of EM27 spectrometers at places inaccessible with a TCCON spectrometer. Moreover, for the study of local emission sources as megacities, large power plants, etc., several mobile EM27 units could be distributed.

Due to these promising results, and the great interest in the NDACC/TCCON community, the company Bruker OptikTM, will offer the EM27TM with the presented modifications within its normal range of products in 2013. This is an important step, as it assures the homogeneity of the instruments, which is a key point for intercomparing the results and for a hypothetical low-resolution network.

7 Summary

Several important error sources for measuring atmospheric gases with FTIR spectroscopy using solar radiation were investigated. Depending on their influence on the retrieval accuracy, measures for their reduction were presented.

An exact solar tracking in the order of 20 arc seconds is desired when recording the spectra. As this was not achieved with previous setups using a quadrant diode as optical feedback, a high precision camera based system was developed. It consists of the novel principle of recording the solar image on the input field stop of the spectrometer. Using real time image processing algorithms, this setup simplifies the optical feedback of the tracker and forms a self calibrating setup. This principle was published in Gisi et al. (2011) and registered at the German Patent and Trade Mark Office (Gisi et al., 2010). The new system was applied to 5 FTIR spectrometers worldwide. For two of these sites new variants of the tracker designs were developed: a low-cost tracker with a large beam diameter, and a low-weight miniature tracker for portable applications with a small diameter. An easy-to-use software with graphical user interface was created which performs the image processing, the astronomical calculations and controls the motors. It is capable of controlling several motor types and tracker designs.

For three sites at which sufficiently long time series exist, unprecedented accuracies of 17, 34 and 10 arc seconds could be determined, which is significantly better than the accuracies with previous tracker systems in the order of 90 arc seconds.

A special focus was put on the calculation of the solar position from a given time and location. The astronomical calculations for the elevation angle have an accuracy of 0.25 arc seconds. In addition, the influences of the atmosphere to the apparent position, depending on wavelength, pressure and temperature were investigated and incorporated in the current atmospheric retrieval procedures. Furthermore, the effects of the solar movement while recording a single spectrum were investigated.

Errors induced by source intensity fluctuations, e.g. from clouds passing in front of the sun were investigated. A correction scheme is presented and applied to interferograms, leading to a reduction of the retrieval errors by several orders of magnitude.

A novel correction scheme interferograms containing sampling errors was presented and applied to a time series of data. This correction was important, as the sampling errors lead to systematic errors in the retrieved CO₂ values.

The importance of taking into account intraday variability of atmospheric pressure and temperature profiles was shown. A program was created which extracts the required information from meteorological

model data. Using this, reductions of errors in the O₂ and CO₂ retrievals by more than 1% could be achieved.

As the global coverage of total column greenhouse gas measurement stations is poor, the capabilities of a portable FTIR instrument were investigated. Despite the low spectral resolution, an accuracy of less than 0.1 % has been achieved in comparison with a high-resolution reference spectrometer, which was published in Gisi et al. (2012). This unprecedented value makes the system capable of supporting existing measuring networks. This is the case, as it can be used in regions with little infrastructure, due to features such as robustness of the optical alignment for mechanical vibrations, immunity towards variable ambient temperatures, small dimensions, low weight and an easy set up. In addition, these characteristics promote the application in measurement campaigns. As the company BrukerTM will offer the demonstrated spectrometer within its standard product range in 2013, the homogeneity of the instruments will be ensured, which is a key point for an instrument used within a network.

8 Publications and Patents

Publications by M. Gisi, sorted by publication date:

- Gisi, M., Hase, F., Dohe, S., Blumenstock, T., Simon, A., Keens, A.: XCO₂-measurements with a tabletop FTS using solar absorption spectroscopy, *Atmos. Meas. Tech.*, 5, 2969-2980, (2012), doi:10.5194/amt-5-2969-2012.
- Schneider, M., Barthlott, S., Hase, F., González, Y., Yoshimura, K., García, O. E., Sepúlveda, E., Gomez-Pelaez, A., Gisi, M., Kohlhepp, R., Dohe, S., Blumenstock, T., Strong, K., Weaver, D., Palm, M., Deutscher, N. M., Warneke, T., Notholt, J., Lejeune, B., Demoulin, P., Jones, N., Griffith, D. W. T., Smale, D. and Robinson, J.: Ground-based remote sensing of tropospheric water vapour isotopologues within the project MUSICA, *Atmos. Meas. Tech. Discuss.*, 5, 5357-5418, doi:10.5194/amtd-5-5357-2012
- Gisi, M., Hase, F., Dohe, S., and Blumenstock, T.: Camtracker: a new camera controlled high precision solar tracker system for FTIR-spectrometers, *Atmos. Meas. Tech.*, 4, 47-54, (2011), doi:10.5194/amt-4-47-2011
- Hoeffler, H., Fechner, P. C., Gisi, M., Baumgartner, F., Galster, U., and Helm, H.: Momentum vector correlations in three-particle fragmentation of triatomic hydrogen, *Physical Review A*, 83(4), 042519 (2011)
- Messerschmidt, J., Geibel, M. C., Blumenstock, T., Chen, H., Deutscher, N. M., Engel, A., Feist, D. G., Gerbig, C., Gisi, M., Hase, F., Katrynski, K., Kolle, O., Lavric, J. V., Notholt, J., Palm, M., Ramonet, M., Rettinger, M., Schmidt, M., Sussmann, R., Toon, G. C., Truong, F., Warneke, T., Wennberg, P. O., Wunch, D., and Xueref-Remy, I.: Calibration of TCCON column-averaged CO₂: the first aircraft campaign, *Atmospheric Chemistry and Physics*, 11(21), 10765-10777, (2011), doi: 10.5194/acp-11-10765-2011
- Ortwein, P., Woiwode, W., Fleck, S., Eberhard, M., Kolb, T., Wagner, S., Gisi, M., and Ebert, V.: Absolute diode laser-based in situ detection of HCl in gasification processes, *Experiments in Fluids*, 49(4), 961-968, (2010), doi: 10.1007/s00348-010-0904-2
- Ortwein, P., Woiwode, W., Wagner, S., Gisi, M. and Ebert, V.: Laser-based measurements of line strength, self- and pressure-broadening coefficients of the H(35)Cl R(3) absorption line in the first overtone region for pressures up to 1 MPa, *Applied Physics B-Lasers and Optics*, 100(2), (2010), doi: 10.1007/s00340-009-3862-8

Patent:

- Gisi, M., Hase, F., and Blumenstock, T: Verfahren zur Ausrichtung des Messstrahles eines FTIR-Spektrometers auf einen ausgewählten Bereich einer relativ zum Spektrometer beweglichen ausgedehnten Strahlungsquelle. (Method for aligning the measuring beams of solar Fourier transform infrared spectrometers onto a selected area of a spatially expanded radiation source, which moves relatively to the spectrometer.), Applied as patent at the German Patent and Trade Mark Office, 2010.

Acknowledgments

The presented thesis was created in my employment as scientific assistant at the Institute for Meteorology and Climate Research (IMK) at the Karlsruhe Institute for Technology (KIT). I thank Prof. Dr. Johannes Orphal for enabling me to do this work and for advising the PhD thesis. Priv.-Doz. Dr. Michael Höpfner I want to thank as well for co-advising this PhD thesis.

Especially I want to thank Dr. Frank Hase for his excellent support and supervision during the complete process of my work, and the advice and corrections for finishing this document. His outstanding willingness for answering questions and having interesting discussions was crucial for the success. I also want to thank Dr. Thomas Blumenstock for his support and readiness to discussions, and for his recommendations for corrections of this document.

I am very grateful to all colleagues in the IMK, which assisted both in professional subjects but also in the necessary balance with non-work related things such as self-cooked lunches and barbecue and board game evenings.

For manufacturing the components for the solar trackers I want to thank Alex Streili and Benjamin Riexinger from the mechanical workshop in the IMK.

I also want to thank Jochen Groß for the support in all electronic questions and for assisting with tools and spare parts.

I thank Martin Kohler from the IMK-TRO for providing tall-tower meteorological data.

Also I acknowledge the Global Modeling and Assimilation Office (GMAO) and the GES DISC for the dissemination of MERRA meteorological datasets, and the NASA Goddard Automailer system for providing temperature and pressure profiles.

This work has been partially funded through grant BU2599/1-1 (RemoteC¹) within the Emmy-Noether programme of Deutsche Forschungsgemeinschaft (DFG).

Special thanks to the 2 kobolds in the spectrometers for their untiringly commitment for moving the scanner mirror ;-)

Especially I want to thank my wife and my parents for the great support they gave me during my studies and in the progress of writing this thesis.

Karlsruhe, November 2012

Michael Gisi

¹<http://www.imk-asf.kit.edu/english/RemoteC.php>

Bibliography

- Abrams, M. C., Toon, G. C., and Schindler, R. A.: Practical example of the correction of Fourier-transform spectra for detector nonlinearity, *Applied Optics*, 33, 6307–6314, 1994.
- Adrian, G. P., Baumann, M., Blumenstock, T., Fischer, H., Friedle, A., Gerhardt, L., Maucher, G., Oelhaf, H., Scheuerpflug, W., Thomas, P., Trieschmann, O., and Wegner, A.: First results of ground-based FTIR measurements of atmospheric trace gases in North Sweden and Greenland during EASOE, *Geophys. Res. Lett.*, 21, 1343–1346, doi:{10.1029/93GL01304}, URL <http://www.agu.org/pubs/crossref/1994/93GL01304.shtml>, 1994.
- Atkins, P. W., ed.: *Physikalische Chemie*, vol. [Hauptbd.]:, Wiley-VCH, Weinheim, 4., vollst. überarb. Aufl. edn., 2006.
- Birch, K. P. and Downs, M. J.: An Updated Edlén Equation for the Refractive Index of Air, *Metrologia*, 30, 155, URL <http://stacks.iop.org/0026-1394/30/i=3/a=004>, 1993.
- Birch, K. P. and Downs, M. J.: Correction to the Updated Edlén Equation for the Refractive Index of Air, *Metrologia*, 31, 315, URL <http://stacks.iop.org/0026-1394/31/i=4/a=006>, 1994.
- Bowring, B. R.: Transformation from Spatial to Geographical Coordinates, *Survey Review*, 23, 323–327, 1976.
- Bretagnon, P. and Francou, G.: Planetary theories in rectangular and spherical variables. VSOP87 solutions, *Astronomy & Astrophysics* 202, 202, 309–315, 1988.
- Chen, J., Gottlieb, E., and Wofsy, S.: Compact FTIR Spectrometer for total column measurement in urban environments, in: IRWG/TCCON Meeting, Wengen (Switzerland), pp. 1–32, 11-15 June 2012, 2012.
- Ciddor, P. E.: Refractive index of air: new equations for the visible and near infrared, *Appl. Opt.*, 35, 1566–1573, doi:10.1364/AO.35.001566, URL <http://ao.osa.org/abstract.cfm?URI=ao-35-9-1566>, 1996.
- Davis, S. D., Abrams, M. C., and Brault, J. W.: *Fourier Transform Spectrometry*, Academic Press, 2010.
- Demtröder, W.: *Experimentalphysik*, vol. 2: Elektrizität und Optik, Springer, Berlin, 5th edn., 2009.

- Demtröder, W.: Experimentalphysik, vol. 3: Atome, Moleküle und Festkörper of *Springer-Lehrbuch*, Springer, Berlin, 4th edn., 2010.
- Dohe, S., Sherlock, V., Hase, F., and Gisi, M.: Correction of sampling ghosts for historic near-infrared Fourier Transform Spectrometer (FTS) measurements, publication in preparation, 2012/2013.
- Edlén, B.: The Refractive Index of Air, *Metrologia*, 2, 71, URL <http://stacks.iop.org/0026-1394/2/i=2/a=002>, 1966.
- Geibel, M. C., Messerschmidt, J., Gerbig, C., Blumenstock, T., Chen, H., Hase, F., Kolle, O., Lavrič, J. V., Notholt, J., Palm, M., Rettinger, M., Schmidt, M., Sussmann, R., Warneke, T., and Feist, D. G.: Calibration of column-averaged CH₄ over European TCCON FTS sites with airborne in-situ measurements, *Atmospheric Chemistry and Physics*, 12, 8763–8775, doi:10.5194/acp-12-8763-2012, URL <http://www.atmos-chem-phys.net/12/8763/2012/>, 2012.
- Geibel, M. C., Gerbig, C., and Feist, D. G.: A new fully automated FTIR system for total column measurements of greenhouse gases, *Atmospheric Measurement Techniques*, 3, 1363–1375, doi:{10.5194/amt-3-1363-2010}, 2010.
- Gerdan, G. P. and Deakin, R. E.: Transforming Cartesian Coordinates X,Y,Z to Geographic Coordinates ϕ , λ , h., *The Australian Surveyor*, 44, 55–63, URL <http://user.gs.rmit.edu.au/rod/files/publications/Transforming%20Cartesian%20Coordinates.pdf>, 1999.
- Gisi, M., Blumenstock, T., and Hase, F.: Verfahren zur Ausrichtung des Messstrahles eines FTIR-Spektrometers auf einen ausgewählten Bereich einer relativ zum Spektrometer beweglichen ausgedehnten Strahlungsquelle. (Method for aligning the measuring beams of solar Fourier transform infrared spectrometers onto a selected area of a spatially expanded radiation source, which moves relatively to the spectrometer.), URL <http://depatisnet.dpma.de/DepatisNet/depatisnet?action=bibdat&docid=DE102010048140A1>, 2010.
- Gisi, M., Hase, F., Dohe, S., and Blumenstock, T.: Camtracker: a new camera controlled high precision solar tracker system for FTIR-spectrometers, *Atmospheric Measurement Techniques*, 4, 47–54, doi: 10.5194/amt-4-47-2011, URL <http://www.atmos-meas-tech.net/4/47/2011/>, 2011.
- Gisi, M., Hase, F., Dohe, S., Blumenstock, T., Simon, A., and Keens, A.: XCO₂-measurements with a tabletop FTS using solar absorption spectroscopy, *Atmospheric Measurement Techniques*, 5, 2969–2980, doi:10.5194/amt-5-2969-2012, URL <http://www.atmos-meas-tech.net/5/2969/2012/>, 2012.
- Günzler, H. and Heise, H. M.: IR-Spektroskopie : eine Einführung, VCH, Weinheim [u.a.], 3., neubearb. Aufl. edn., 1996.

- Griffiths, P. R., Haseth, J. A. D., and Winefordner, J. D.: *Fourier Transform Infrared Spectrometry*, Wiley John + Sons, 2007.
- Guelachvili, G.: *Spectrometric techniques*, vol. 2, chap. Distortions in Fourier spectra and diagnosis, pp. 1–61, Academic Pr., New York, 1981.
- Haralick, R. and Shapiro, L.: *Computer and robot vision*, vol. Edition 1 Volume 2, Addison-Wesley publishing company, 1993.
- Hase, F.: *Messung des Apparateprofils eines hochauflösenden FTIR-Spektrometers*, Master's thesis, Universität Karlsruhe (TH), diplomarbeit im Fach Physik, 1995.
- Hase, F.: *Inversion von Spurengasprofilen aus hochaufgelösten bodengebundenen FTIR-Messungen in Absorption*, Ph.D. thesis, Universität Karlsruhe (TH), URL <http://www-imk.fzk.de/asf/ftir/disshase.pdf>, dissertation FZK Report No. 6512, 2000.
- Hase, F.: Improved instrumental line shape monitoring for the ground-based, high-resolution FTIR spectrometers of the Network for the Detection of Atmospheric Composition Change, *Atmospheric Measurement Techniques*, 5, 603–610, doi:10.5194/amt-5-603-2012, URL <http://www.atmos-meas-tech.net/5/603/2012/>, 2012.
- Hase, F. and Höpfner, M.: Atmospheric Ray Path Modeling for Radiative Transfer Algorithms, *Appl. Opt.*, 38, 3129–3133, doi:10.1364/AO.38.003129, URL <http://ao.osa.org/abstract.cfm?URI=ao-38-15-3129>, 1999.
- Hase, F., Blumenstock, T., and Paton-Walsh, C.: Analysis of the Instrumental Line Shape of High-Resolution Fourier Transform IR Spectrometers with Gas Cell Measurements and New Retrieval Software, *Appl. Opt.*, 38, 3417–3422, doi:10.1364/AO.38.003417, URL <http://ao.osa.org/abstract.cfm?URI=ao-38-15-3417>, 1999.
- Hase, F., Demoulin, P., Sauval, A., Toon, G., Bernath, P., Goldman, A., Hannigan, J., and Rinsland, C.: An empirical line-by-line model for the infrared solar transmittance spectrum from 700 to 5000 cm^{-1} , *Journal of Quantitative Spectroscopy and Radiative Transfer*, 102, 450 – 463, doi:10.1016/j.jqsrt.2006.02.026, URL <http://www.sciencedirect.com/science/article/pii/S0022407306000343>, 2006.
- Hase, F., Hannigan, J., Coffey, M., Goldman, A., Höpfner, M., Jones, N., Rinsland, C., and Wood, S.: Intercomparison of retrieval codes used for the analysis of high-resolution, ground-based FTIR measurements, *Journal of Quantitative Spectroscopy & Radiative Transfer*, 87, 25–52, doi:{10.1016/j.jqsrt.2003.12.008}, 2004.
- Hase, F., Demoulin, P., Sauval, A. J., Toon, G. C., Bernath, P. F., Goldman, A., Hannigan, J. W., and Rinsland, C. P.: An empirical line-by-line model for the infrared solar transmittance spectrum from

- 700 to 5000 cm^{-1}), *Journal of Quantitative Spectroscopy & Radiative Transfer*, 102, 450–463, doi: {10.1016/j.jqsrt.2006.02.026}, 2006.
- Hase, F., Wallace, L., McLeod, S. D., Harrison, J. J., and Bernath, P. F.: The ACE-FTS atlas of the infrared solar spectrum, *Journal of Quantitative Spectroscopy & Radiative Transfer*, 111, 521–528, doi:{10.1016/j.jqsrt.2009.10.020}, 2010.
- Humlíček, J.: An efficient method for evaluation of the complex probability function: The Voigt function and its derivatives, *Journal of Quantitative Spectroscopy and Radiative Transfer*, 21, 309 – 313, doi:10.1016/0022-4073(79)90062-1, URL <http://www.sciencedirect.com/science/article/pii/0022407379900621>, 1979.
- Huster, S.: Bau eines automatischen Sonnenverfolgers für bodengebundene IR-Absorptionsmessungen, Master's thesis, Forschungszentrum Karlsruhe, diploma Thesis Forschungszentrum Karlsruhe, 1998.
- IPCC: Fourth Assessment Report: Climate Change 2007: The AR4 Synthesis Report, Geneva: IPCC, URL http://www.ipcc.ch/pdf/assessment-report/ar4/syr/ar4_syr.pdf, 2007.
- Jones, N., Griffith, D., Velasco, V., Macatangay, R., O'Brien, D., Clark, A., and Rayner, P.: Solar FTS-lite down under, in: IRWG/TCCON Meeting, Wengen (Switzerland), pp. 1–17, 11-15 June 2012, 2012.
- Keppel-Aleks, G., Toon, G. C., Wennberg, P. O., and Deutscher, N. M.: Reducing the impact of source brightness fluctuations on spectra obtained by Fourier-transform spectrometry, *Appl. Opt.*, 46, 4774–4779, doi:10.1364/AO.46.004774, URL <http://ao.osa.org/abstract.cfm?URI=ao-46-21-4774>, 2007.
- Kobayashi, N., Inoue, G., Kawasaki, M., Yoshioka, H., Minomura, M., Murata, I., Nagahama, T., Matsumi, Y., Tanaka, T., Morino, I., and Ibuki, T.: Remotely operable compact instruments for measuring atmospheric CO_2 and CH_4 column densities at surface monitoring sites, *Atmospheric Measurement Techniques*, 3, 1103–1112, doi:10.5194/amt-3-1103-2010, URL <http://www.atmos-meas-tech.net/3/1103/2010/>, 2010.
- Kohlhepp, R., Ruhnke, R., Chipperfield, M. P., De Mazière, M., Notholt, J., Barthlott, S., Batchelor, R. L., Blatherwick, R. D., Blumenstock, T., Coffey, M. T., Demoulin, P., Fast, H., Feng, W., Goldman, A., Griffith, D. W. T., Hamann, K., Hannigan, J. W., Hase, F., Jones, N. B., Kagawa, A., Kaiser, I., Kasai, Y., Kirner, O., Kouker, W., Lindenmaier, R., Mahieu, E., Mittermeier, R. L., Monge-Sanz, B., Morino, I., Murata, I., Nakajima, H., Palm, M., Paton-Walsh, C., Raffalski, U., Reddmann, T., Rettinger, M., Rinsland, C. P., Rozanov, E., Schneider, M., Senten, C., Servais, C., Sinnhuber, B.-M., Smale, D., Strong, K., Sussmann, R., Taylor, J. R., Vanhaelewyn, G., Warneke, T., Whaley, C., Wiehle, M., and Wood, S. W.: Observed and simulated time evolution of HCl, ClONO₂, and HF total column

- abundances, *Atmospheric Chemistry and Physics*, 12, 3527–3556, doi:10.5194/acp-12-3527-2012, URL <http://www.atmos-chem-phys.net/12/3527/2012/>, 2012.
- Lamouroux, J., Tran, H., Laraia, A. L., Gamache, R. R., Rothman, L. S., Gordon, I. E., and Hartmann, J. M.: Updated database plus software for line-mixing in CO₂ infrared spectra and their test using laboratory spectra in the 1.5-2.3 μm region, *Journal of Quantitative Spectroscopy & Radiative Transfer*, 111, 2321–2331, doi:{10.1016/j.jqsrt.2010.03.006}, 2010.
- Lang, K. R.: *Astrophysical Data: Planets and Stars*, Springer Verlag, 1991.
- Learner, R. C. M., Thorne, A. P., and Brault, J. W.: Ghosts and artifacts in Fourier-transform spectrometry, *Appl. Opt.*, 35, 2947–2954, doi:10.1364/AO.35.002947, URL <http://ao.osa.org/abstract.cfm?URI=ao-35-16-2947>, 1996.
- Liu, Y., Lin, J., Huang, G., Guo, Y., and Duan, C.: Simple empirical analytical approximation to the Voigt profile, *J. Opt. Soc. Am. B*, 18, 666–672, doi:10.1364/JOSAB.18.000666, URL <http://josab.osa.org/abstract.cfm?URI=josab-18-5-666>, 2001.
- Marchetti, S. and Simili, R.: Accurate measurement of the refractive index of CO₂, N₂, He, O₂, and air at 10.57 μm and T = 23°C, *Infrared Physics & Technology*, 47, 263 – 266, doi:10.1016/j.infrared.2004.12.005, URL <http://www.sciencedirect.com/science/article/pii/S1350449504001537>, 2006.
- Mathar, R. J.: Calculated Refractivity of Water Vapor and Moist Air in the Atmospheric Window at 10 μm , *Appl. Opt.*, 43, 928–932, doi:10.1364/AO.43.000928, URL <http://ao.osa.org/abstract.cfm?URI=ao-43-4-928>, 2004.
- Mathar, R. J.: Refractive index of humid air in the infrared: model fits, *Journal of Optics A: Pure and Applied Optics*, 9, 470, URL <http://stacks.iop.org/1464-4258/9/i=5/a=008>, 2007.
- Matsumoto, H.: The Refractive Index of Moist Air in the 3- μm Region, *Metrologia*, 18, 49–52, doi: {10.1088/0026-1394/18/2/001}, 1982.
- Meeus, J.: *Astronomical Algorithms*, Willmann-Bell, Inc., Richmond, Virginia, 1991.
- Merlaud, A., De Mazière, M., Hermans, C., and Cornet, A.: Equations for Solar Tracking, *Sensors*, 12, 4074–4090, doi:10.3390/s120404074, URL <http://www.mdpi.com/1424-8220/12/4/4074>, 2012.
- Messerschmidt, J., Geibel, M. C., Blumenstock, T., Chen, H., Deutscher, N. M., Engel, A., Feist, D. G., Gerbig, C., Gisi, M., Hase, F., Katrynski, K., Kolle, O., Lavrič, J. V., Notholt, J., Palm, M., Ramonet, M., Rettinger, M., Schmidt, M., Sussmann, R., Toon, G. C., Truong, F., Warneke, T., Wennberg, P. O., Wunch, D., and Xueref-Remy, I.: Calibration of TCCON column-averaged CO₂: the first aircraft campaign over European TCCON sites, *Atmospheric Chemistry and Physics*, 11, 10765–10777, doi: 10.5194/acp-11-10765-2011, URL <http://www.atmos-chem-phys.net/11/10765/2011/>, 2011.

- Messerschmidt, J., Macatangay, R., Notholt, J., Petri, C., Warneke, T., and Weinzierl, C.: Side by side measurements of CO₂ by ground-based Fourier transform spectrometry (FTS), *Tellus series B - chemical and physical meteorology*, 62, 749–758, doi:{10.1111/j.1600-0889.2010.00491.x}, 2010.
- Notholt, J., Beninga, I., and Schrems, O.: Shipborne FT-IR Measurements of Atmospheric Trace Gases on a South (33°S) to North (53°N) Atlantic Traverse, *Appl. Spectrosc.*, 49, 1525–1527, URL <http://as.osa.org/abstract.cfm?URI=as-49-10-1525>, 1995.
- Notholt, J., Toon, G., Rinsland, C., Pougatchev, N., Jones, N., Connor, B., Weller, R., Gautrois, M., and Schrems, O.: Latitudinal variations of trace gas concentrations in the free troposphere measured by solar absorption spectroscopy during a ship cruise, *J. Geophys. Res. - Atmospheres*, 105, 1337–1349, doi:{10.1029/1999JD900940}, 2000.
- Olivero, J. and Longbothum, R.: Empirical fits to the Voigt line width: A brief review, *Journal of Quantitative Spectroscopy and Radiative Transfer*, 17, 233 – 236, doi:10.1016/0022-4073(77)90161-3, URL <http://www.sciencedirect.com/science/article/pii/0022407377901613>, 1977.
- Olsen, S. C. and Randerson, J. T.: Differences between surface and column atmospheric CO₂ and implications for carbon cycle research, *J. Geophys. Res.*, 109, doi:10.1029/2003JD003968, 2004.
- Þorsteinn Sæmundsson: *Atmospheric Refraction*, *Sky & Telescope* (72), 1986.
- Ouyang, X. and Varghese, P. L.: Reliable and efficient program for fitting Galatry and Voigt profiles to spectral data on multiple lines, *Appl. Opt.*, 28, 1538–1545, doi:10.1364/AO.28.001538, URL <http://ao.osa.org/abstract.cfm?URI=ao-28-8-1538>, 1989.
- Petri, C., Warneke, T., Jones, N., Ridder, T., Messerschmidt, J., Weinzierl, T., Geibel, M., and Notholt, J.: Remote sensing of CO₂ and CH₄ using solar absorption spectrometry with a low resolution spectrometer, *Atmospheric Measurement Techniques*, 5, 1627–1635, doi:10.5194/amt-5-1627-2012, URL <http://www.atmos-meas-tech.net/5/1627/2012/>, 2012.
- Petty, G. W.: *A first course in atmospheric radiation*, Sundog Publ., Madison, 2nd edn., 2006.
- Puerta, J. and Martin, P.: Three and four generalized Lorentzian approximations for the Voigt line shape, *Appl. Opt.*, 20, 3923–3928, doi:10.1364/AO.20.003923, URL <http://ao.osa.org/abstract.cfm?URI=ao-20-22-3923>, 1981.
- Schneider, M., Hase, F., Blumenstock, T., Redondas, A., and Cuevas, E.: Quality assessment of O₃ profiles measured by a state-of-the-art ground-based FTIR observing system, *Atmospheric Chemistry and Physics*, 8, 5579–5588, doi:10.5194/acp-8-5579-2008, URL <http://www.atmos-chem-phys.net/8/5579/2008/>, 2008.

- Schneider, M., Romero, P. M., Hase, F., Blumenstock, T., Cuevas, E., and Ramos, R.: Continuous quality assessment of atmospheric water vapour measurement techniques: FTIR, Cimel, MFRSR, GPS, and Vaisala RS92, *Atmospheric Measurement Techniques*, 3, 323–338, doi:10.5194/amt-3-323-2010, URL <http://www.atmos-meas-tech.net/3/323/2010/>, 2010.
- Sepúlveda, E., Schneider, M., Hase, F., García, O. E., Gomez-Pelaez, A., Dohe, S., Blumenstock, T., and Guerra, J. C.: Long-term validation of tropospheric column-averaged CH₄ mole fractions obtained by mid-infrared ground-based FTIR spectrometry, *Atmospheric Measurement Techniques*, 5, 1425–1441, doi:10.5194/amt-5-1425-2012, URL <http://www.atmos-meas-tech.net/5/1425/2012/>, 2012.
- Toon, G. and Wunch, D.: Diurnal asymmetry in O₂/Air, in: IRWG/TCCON Meeting, Wollongong (Australia), pp. 1–14, 2-7 June 2010, 2010.
- Toon, G., Blavier, J.-F., Washenfelder, R., Wunch, D., Keppel-Aleks, G., Wennberg, P., Connor, B., Sherlock, V., Griffith, D., Deutscher, N., and Notholt, J.: Total Column Carbon Observing Network (TCCON), URL http://www.tcccon.caltech.edu/publications/OSA_FTS_Meeting_20090323.pdf, 2009.
- Washenfelder, R. A., Toon, G. C., Blavier, J.-F., Yang, Z., Allen, N. T., Wennberg, P. O., Vay, S. A., Matross, D. M., and Daube, B. C.: Carbon dioxide column abundances at the Wisconsin Tall Tower site, *J. Geophys. Res.*, 111, URL <http://www.agu.org/pubs/crossref/2006/2006JD007154.shtml>, 2006.
- Wunch, D., Toon, G. C., Wennberg, P. O., Wofsy, S. C., Stephens, B. B., Fischer, M. L., Uchino, O., Abshire, J. B., Bernath, P., Biraud, S. C., Blavier, J.-F. L., Boone, C., Bowman, K. P., Browell, E. V., Campos, T., Connor, B. J., Daube, B. C., Deutscher, N. M., Diao, M., Elkins, J. W., Gerbig, C., Gottlieb, E., Griffith, D. W. T., Hurst, D. F., Jiménez, R., Keppel-Aleks, G., Kort, E. A., Macatangay, R., Machida, T., Matsueda, H., Moore, F., Morino, I., Park, S., Robinson, J., Roehl, C. M., Sawa, Y., Sherlock, V., Sweeney, C., Tanaka, T., and Zondlo, M. A.: Calibration of the Total Carbon Column Observing Network using aircraft profile data, *Atmospheric Measurement Techniques*, 3, 1351–1362, doi:10.5194/amt-3-1351-2010, URL <http://www.atmos-meas-tech.net/3/1351/2010/>, 2010.
- Wunch, D., Toon, G. C., Blavier, J.-F. L., Washenfelder, R. A., Notholt, J., Connor, B. J., Griffith, D. W. T., Sherlock, V., and Wennberg, P. O.: The Total Carbon Column Observing Network, *Philosophical Transactions of the Royal Society A: Mathematical, Physical and Engineering Sciences*, 369, 2087–2112, doi:10.1098/rsta.2010.0240, URL <http://rsta.royalsocietypublishing.org/content/369/1943/2087.abstract>, 2011.

Acronyms

ADC Analog to Digital Converter

a.s.l Above Sea Level

CFCs Chlorofluorocarbon

DMF Dry air Mole Fractions

CMOS Complementary Metal Oxide Semiconductor

ECMWF European Centre for Medium-Range Weather Forecasts

FOV Field Of View

FT Fourier Transformation

FTS Fourier Transform Spectrometry

FTIR Fourier Transform Infrared

FWHM Full Width at Half Maximum

GAW Global Atmospheric Watch

GFIT Software for determination of trace gases out of solar absorption spectra

GLORIA GLOBal Limb Radiance Imager of the Atmosphere

GMAO Global Modeling and Assimilation Office

GMT Greenwich Mean Sidereal Time

GOSAT Greenhouse gases Observing SATellite

GPR Ghost-To-Parent Ratio

GSFC Goddard Space Flight Center

HITRAN High Resolution Transmission Molecular Absorption Database

IASI Infrared Atmospheric Sounding Interferometer

IERS International Earth Rotation and Reference System Service

IFG Interferogram

ILS Instrumental Lineshape

IMK Institut für Meteorologie und Klimaforschung

InGaAs Indium Gallium Arsenide

InSb Indium Antimonid

IPCC Intergovernmental Panel on Climate Change

JD Julian Day

JPL Jet Propulsion Laboratory

KIT Institute for Meteorology and Climat Research

LINEFIT Software for determination of ILS out of gas cell measurements

LAST Local Apparent Sidereal Time

LOS Line Of Sight

LST Local Sidereal Time

LTE Local Thermodynamic Equilibrium

MCT Mercury Cadmium Telluride

MERRA Modern-Era Retrospective analysis for Research and Applications

MIC Mirror-Image-Correlation

MIPAS Michelson Interferometer for Passive Atmospheric Sounding

MIR Mid-InfRared

NASA National Aeronautics and Space Administration

NCAR National Center for Atmospheric Research

NCEP National Centers for Environmental Prediction

NDACC Network for the Detection of Atmospheric Climate Change

NIR Near-InfraRed

NOAA National Oceanic and Atmospheric Administration

OCO Orbiting Carbon Observatory

OPD Optical Path Difference

PROFFIT Software for determination of trace gases out of solar absorption spectra

PSC Polar Stratospheric Cloud

SBF Source Brightness Fluctuation

SFIT2 Software for determination of trace gases out of solar absorption spectra

SNR Signal-to-Noise ratio

SZA Solar Zenith Angle

TCCON Total Carbon Column Observing Network

UNAM Universidad Nacional Autónoma de México

UT Universal Time

UTC Coordinated Universal Time

VIS Visible

VMR Volume Mixing Ratio

WMO World Meteorological Organization